

Stellar populations of galaxies in the ALHAMBRA survey up to $z \sim 1$

II. Stellar populations of quiescent galaxies within the stellar mass- and the UVJ colour-colour diagrams

L. A. Díaz-García¹ ^{*}, A. J. Cenarro¹, C. López-Sanjuan¹, I. Ferreras², M. Cerviño^{3,4}, A. Fernández-Soto^{5,6},
I. Márquez³, M. Pović³, I. San Roman¹, K. Viironen¹, M. Moles^{1,3}, D. Cristóbal-Hornillos¹, E. Alfaro³,
T. Aparicio-Villegas⁷, N. Benítez³, T. Broadhurst^{8,9}, J. Cabrera-Caño¹⁰, F. J. Castander¹¹, J. Cepa^{4,12},
R. M. González Delgado³, C. Husillos³, L. Infante^{13,14}, J. A. L. Aguerri^{4,12}, J. Masegosa³, A. Molino¹⁵, A. del Olmo³,
J. Perea³, F. Prada³, J. M. Quintana³, and V. J. Martínez^{16,17,6}

(Affiliations can be found after the references)

Received ? / Accepted ?

ABSTRACT

Aims. We aim at discerning the distribution of stellar population parameters (extinction, age, metallicity, and sSFR) of quiescent galaxies within the rest-frame stellar mass- and UVJ colour-colour diagrams up to $z \sim 1$ and down to $m_{F814} = 23$ AB, as well as the development of new diagrams to reduce the contamination from dust-reddened galaxies in samples of quiescent galaxies.

Methods. By use of the photometric data from ALHAMBRA, we determine the stellar population parameters of quiescent galaxies using the SED-fitting code MUFFIT and different SSP models. Through the extinctions retrieved by MUFFIT, we remove dusty star forming galaxies from the sample of quiescent galaxies. The distribution of all the stellar populations parameters is also fitted by a bidimensional and locally weighted regression method (LOESS) across the rest-frame diagrams to mitigate the impact of uncertainties and provide the likely distribution of stellar population parameters in these diagrams.

Results. Quiescent galaxies selected via classical UVJ diagrams are typically contaminated by a ~ 20 % fraction of dusty star forming galaxies. A significant part of the galaxies that reside in the green valley are actually obscured star-forming galaxies (~ 65 %). Therefore, the transition of galaxies from the blue cloud to the red sequence, and hence the related mechanisms for quenching, seems to be much more efficient and faster than previously considered. There are well defined correlations in both the rest-frame stellar mass- and UVJ colour-colour diagrams that allow to constrain the ages, metallicities, extinctions, and sSFR of quiescent galaxies with only their rest-frame colours, redshifts and stellar masses. Dust corrections play an important role in understanding how quiescent galaxies are distributed in these diagrams. To perform a pure non-biased selection of quiescent galaxies from these diagrams is key to include dust corrections of the involved colours and also the galaxy stellar mass.

Key words. galaxies: stellar content – galaxies: photometry – galaxies: evolution – galaxies: formation – galaxies: high-redshift

1. Introduction

Galaxies exhibit a well known bimodal distribution with respect to colour (e. g. Bell et al. 2004; Baldry et al. 2004; Williams et al. 2009; Ilbert et al. 2010; Peng et al. 2010; Arnouts et al. 2013; Moresco et al. 2013; Fritz et al. 2014). Red galaxies present more evolved stellar populations with lower star formation levels, for which they are usually referred as passive or quiescent. In contrast, the blue ones exhibit younger stellar populations with signatures of strong star formation processes typically. The formation and evolution of the so-called quiescent/passive galaxies is still today a challenge, as these galaxies started to form stars at very early epochs, to later shut down their star formation by a mechanism that is still today matter of debate (see references in Peng et al. 2015).

One of the most extended diagrams for disentangling different types of galaxies involves rest-frame colours and absolute magnitudes (e. g. Bell et al. 2004; Baldry et al. 2004; Brown et al. 2007). These diagrams, usually referred as colour-magnitude diagrams (CMD), clearly show the well known bi-

modal distribution of galaxies. There is a numerous population of galaxies with $U - V$ blue colours lying on the CMD lower parts (the so-called blue cloud) with typical young stellar populations. Whereas in the red part of the CMD, there is a dominant population of massive galaxies, called red-sequence galaxies, with predominant older and more evolved stellar populations. In between, some authors define an additional, third sub-population of galaxies, the green valley, with a significant overdensity of active galactic nuclei (AGN, Nandra et al. 2007; Bundy et al. 2008; Georgakakis et al. 2008; Silverman et al. 2008; Hickox et al. 2009; Schawinski et al. 2009), that some authors interpret as a mechanism to produce a transition of galaxies from the blue-cloud to the red-sequence (e. g. Faber et al. 2007; Schawinski et al. 2007). Although, there are evidences to support that galaxies belonging to the green valley are mainly dust-reddened star-forming galaxies (Bell et al. 2005; Cowie & Barger 2008; Brammer et al. 2009; Cardamone et al. 2010). During the last decade, the rest-frame colour-colour diagrams, specially the UVJ diagram, has become one of the most extended methods for separating these two kinds of galaxies (e. g. Daddi et al. 2004; Williams et al. 2009; Arnouts et al.

^{*} e-mail: diaz@cefca.es

2013). The advantage of these diagrams is that they use two colours (one in the blue part of the SED, e. g. $U - V$ or $NUV - r$; the other one in the red part, e. g. $V - J$ or $r - K$), that reduce the contamination of dusty star-forming galaxies in the passive or quiescent sample with predominant red colours and low star formation (e. g. Williams et al. 2009; Arnouts et al. 2013; Ilbert et al. 2013; Moresco et al. 2013). The efficiency of these colour-colour diagrams resides in that galaxies empirically present a more separated loci between red and blue populations than typical colour-magnitude diagrams, in which both populations appear overlapped partially (Wyder et al. 2007; Cowie & Barger 2008; Brammer et al. 2009). Despite the UVJ diagrams demonstrated to be a reliable method to split quiescent from star-forming galaxies, these diagrams present a level of contamination in the selection of quiescent galaxies that depends on redshift and stellar mass (Williams et al. 2009; Moresco et al. 2013). In some cases, the number of star-forming outliers may reach 30 % at certain redshift and mass regime, or at least a 15 % after imposing a more restrictive $U - V$ colour limit than the one defined originally (Moresco et al. 2013).

Alternative methods for splitting galaxies comprise colours and stellar masses (Peng et al. 2010), but these are quasi-equivalent to the colour magnitude diagrams, as absolute magnitudes or luminosities are tightly linked to stellar mass. Therefore, colour-stellar mass diagrams present similar non-negligible contaminations of dusty star-forming galaxies in the red part, as they are not able to distinguish the influence of dust. Other works (e. g. Noeske et al. 2007; Whitaker et al. 2012; Moustakas et al. 2013; Fumagalli et al. 2014) suggest introducing star formation rates (SFR), along with stellar masses, as a criterion for separating both quiescent and star-forming galaxies. This diagram has the disadvantage that a previous estimation of the mentioned stellar population parameters is necessary, which in many cases are not available or they could be calculated with great difficulty. In some cases, SFR and specific star formation rates (sSFR, defined as the star formation rate per unit of stellar mass, i. e. SFR/M_*) can be also used as an additional (or the unique criterion) for selecting passive or quiescent galaxies below a threshold (e. g. Ilbert et al. 2010; Pozzetti et al. 2010; Domínguez Sánchez et al. 2011, 2016).

Recent work shows that some stellar population parameters are related to the range of colours that galaxies occupy in UVJ colour-colour diagrams (Belli et al. 2015; Domínguez Sánchez et al. 2016; Martis et al. 2016; Pacifici et al. 2016; Yano et al. 2016; Fang et al. 2017). There is a general agreement amongst results pointing out that certain ranges of SFR and sSFR values are well constrained in precise colour ranges in UVJ diagrams. Thereby, galaxies in the typical colour ranges enclosing quiescent galaxies exhibit low sSFR, whereas the largest sSFR values lie on the lower parts of these kind of diagrams. In fact, there is evidence to support a continuous sSFR gradient perpendicular to the empirical colour limit separating quiescent from star-forming galaxies in UVJ diagrams (see e. g. Belli et al. 2015; Fang et al. 2017). In addition, and as expected from extinction laws, the most dust-reddened galaxies would populate the reddest parts of these diagrams (see e. g. Martis et al. 2016; Fang et al. 2017). This suggests that rest-frame UVJ diagrams may be used as stellar population estimators to predict, or at least constrain, the stellar population properties of galaxies. However, this potential idea has not been extensively exploited in detail yet (specially for quiescent galaxies), and usually stellar populations are only plotted on these diagrams with the unique purpose of a sanity check. Large scale multifilter surveys can provide a large number of galaxies to

largely populate the full range of colours for any kind of rest-frame colour-colour diagrams at wide redshift ranges and stellar masses.

This paper is the second in a series in which we aim at improving our knowledge of the evolution of quiescent galaxies since $z \sim 1$ through the use of spectrophotometric data from the ALHAMBRA survey (Moles et al. 2008). In this work, we focus on the distribution of the stellar population parameters of quiescent galaxies within the UVJ diagram, dissecting for the first time the loci of ages, metallicities, extinctions, and sSFR simultaneously for a complete and numerous sample of quiescent galaxies from the large scale multi-filter photometric ALHAMBRA survey (Moles et al. 2008). In addition, we extend this study to the stellar mass-colour diagram, which also illustrates the influence of the stellar mass more easily and complements the reliability in the selection of quiescent galaxies.

This paper is organized as follows. In Sect. 2, we present the main features of the ALHAMBRA survey, the SED-fitting methodology carried out by MUFFIT, as well as the set of SSP models taken to constrain the stellar populations of quiescent galaxies from ALHAMBRA. Section 3 details the careful process to build a sample of quiescent galaxies complete in stellar mass from the ALHAMBRA photometric catalogues. The techniques to retrieve SFR, and therefore sSFR, from the SED-fitting results provided by MUFFIT and values for dusty star-forming galaxies are shown in Sect. 4. The main result of this work, that is, the distribution of the stellar population parameters of quiescent galaxies within stellar mass- and colour-colour rest-frame diagrams, is given in Sect. 5. Implications from our results are discussed in Sect. 6. The summary and conclusions of this work are provided in Sect. 7.

Throughout this paper we assume a Λ CDM cosmology with $H_0 = 71 \text{ km s}^{-1}$, $\Omega_M = 0.27$, and $\Omega_\Lambda = 0.73$. All magnitudes are in the AB-system (Oke & Gunn 1983). The stellar masses are given in solar mass units [M_\odot].

2. The ALHAMBRA data

The ALHAMBRA survey¹ (Moles et al. 2008) provides a total of 23 photometric bands² in AB-magnitudes (Coe et al. 2006, PSF corrected), 20 in the optical range $\lambda\lambda$ 3500–9700 Å and 3 at the NIR regime $\lambda\lambda$ 1.0–2.3 μm , for each source in 8 non-contiguous fields along the northern hemisphere, the current effective area is $\sim 2.8 \text{ deg}^2$ and the total on-target exposure time $\sim 700 \text{ h}$ ($\sim 608 \text{ h}$ were dedicated for the optical bands, and $\sim 92 \text{ h}$ for the NIR ones). The optical photometric system of ALHAMBRA (Aparicio Villegas et al. 2010) is composed of 20 medium band filters, $FWHM \sim 300 \text{ Å}$, with a flat top transmission and overlapping close to zero between contiguous bands. The magnitude limits in the optical bands, 5σ level and $3''$ aperture, range from $m_{AB} \sim 24$ for the 14 bluer filters, decreasing towards the red, reaching $m_{AB} \sim 22$ in the reddest one (Molino et al. 2014). The ALHAMBRA NIR range was imaged using the standard J , H , and K_s bands for the same fields than in the optical one, with a 50% of recovery efficiency depth (point-like sources) equal to $J \sim 22.4$, $H \sim 21.3$ and $K_s \sim 20.0$ (Cristóbal-Hornillos et al. 2009). The observations were performed with two different cameras depending of the spectral range or set of filters used. In the optical range were made using the wide-field camera LAICA³ (4 CCDs of 4096×4096 pixels and pixel scale $0.225'' \text{ pixel}^{-1}$) and

¹ <http://www.alhambrasurvey.com>

² <http://svo2.cab.inta-csic.es/theory/fps3/>

³ <http://www.caha.es/CAHA/Instruments/LAICA>

with Omega-2000⁴ in the NIR regime (ICCD with 2048×2048 pixels and plate scale $0.45'' \text{ pixel}^{-1}$), both in the 3.5 m telescope in the Calar Alto Observatory⁵ (CAHA).

Our reference catalogue is the ALHAMBRA Gold catalogue⁶ (Molino et al. 2014) that contains $\sim 95\,000$ galaxies imaged in 20 + 3 optical and NIR bands respectively. This catalogue provides an accurate enough photometry (non-fixed aperture) as for developing stellar population studies of galaxies (Díaz-García et al. 2015), complemented with precise photo- z predictions ($\sigma_z \sim 0.012$). In order to build the galaxy set from the Gold catalogue, we took all the sources classified as galaxies (STAR/GALAXY discriminator parameter `Stellar_flag` ≤ 0.5); and also imaged with 70% photometric weight on the detection image (`PercW` ≥ 0.7), the latter to avoid photometric errors in the galaxies close to the image edges. This catalogue also provides the synthetic AB-magnitude m_{F814W} , which is mainly employed for detection purposes and that sets the Gold catalogue selection as $m_{F814W} \leq 23$. This synthetic band is not used during the SED-fitting process anytime.

2.1. Stellar-population parameters in ALHAMBRA

Along this chapter, we focus on the evolution and assembly of the so-called quiescent galaxy population (galaxies without dominant star formation processes, which predominantly present red colours), as well as on the role of the stellar mass, studying how their stellar populations evolved along cosmic time. To explore this topic, we only employed the photometric data of each galaxy in ALHAMBRA and a set of the SED-fitting techniques that were specifically and carefully developed for setting constraints on their stellar population parameters. These techniques are powerful and present high capabilities for this kind of surveys (see e. g. Díaz-García et al. 2015).

In order to retrieve the stellar population parameters of our galaxies, we ran the generic code MUFFIT⁷ (largely detailed by Díaz-García et al. 2015), since this code demonstrated to be a reliable tool for exploring the stellar content of galaxies from multi-filter photometric data and it is specifically optimised to deal with multi-photometric data. We include in our analysis the iterative process for removing those bands that may be affected by strong emission lines, to carry out a detailed analysis of the galaxy SED even when strong nebular or AGN emission lines are present. The results are complemented by the Monte Carlo simulations available in MUFFIT, in order to explore the kind of errors and uncertainties that affect the retrieved stellar population parameters. From MUFFIT analysis, we retrieved ages and metallicities (both luminosity- and mass-weighted), photo z (treated as another free parameter in the 1σ confidence level provided by the Gold catalogue), stellar masses, rest-frame luminosities or k -corrections, and extinctions.

For the analysis, we use different sets of SSP models to assess potential systematics from the use of a given population synthesis model. Firstly, we selected the Bruzual & Charlot (2003) SSP models (hereafter BC03; Padova 1994 tracks, ages from 0.06 to 14 Gyr, and metallicities $[M/H] = -1.65, -0.64, -0.33, 0.09, 0.55$) with a Chabrier (2003) initial mass function (IMF). The BC03 spectral coverage, $\lambda\lambda\, 91\, \text{\AA} - 160\, \mu\text{m}$, allows us to perform our analysis in an extensive redshift range, as in the ALHAMBRA case where the population of galaxies easily

extends up to redshift $z \sim 1.5$. On the other hand, we make use of the set of MIUSCAT SSP models, which are an extension of the Vazdekis et al. (2003, 2010) models and are built from empirical stellar spectra. Owing to the variety of spectral wavelength-ranges and stellar population parameters handled for this family of models (see e. g. <http://miles.iac.es>), we select various sets to cover our needs during the analysis and interpretation of stellar population results. More precisely, we chose the UV and NIR extension of MIUSCAT models (EMILES, $\lambda\lambda\, 1\,680\, \text{\AA} - 5\, \mu\text{m}$; Vazdekis et al. 2016) taking the two sets of theoretical isochrones: the scaled-solar isochrones of Girardi et al. (2000, hereafter Padova00) and Pietrinferni et al. (2004, BaSTI in the following). It is noteworthy that this set includes the optical MIUSCAT SSP predictions (Vazdekis et al. 2012; Ricciardelli et al. 2012), the NIR ones of MIUSCATIR (Röck et al. 2015), and the UV extension from the NGSL stellar library (Koleva & Vazdekis 2012). For EMILES, we took 22 ages in the range 0.05–14 Gyr and metallicities $[M/H] = -1.31, -0.71, -0.40, 0.00, 0.22$ for Padova00 and $[M/H] = -1.26, -0.96, -0.66, -0.35, 0.06, 0.26, 0.40$ for BaSTI, with Kroupa Universal IMF.

For the whole set of SSP models, we added extinctions to the SSPs with values in the range $A_V = 0.0 - 3.1$ (assuming a constant value $R_V = 3.1$), following the extinction law of Fitzpatrick (1999). This extinction law covers a wider spectral range than the observed in ALHAMBRA since $z \sim 2$, and it is suitable for dereddening any photospectroscopic data and accounting for uncertainties robustly (further details in Fitzpatrick 1999). Previously to the SED-fitting analysis, the photometry of the galaxies was also corrected of the Milky Way dust using MUFFIT. Although the discrepancies among the 4 CCDs of the LAICA camera are mild, each galaxy was analysed with the SSP model set after convolving it with the precise photometric system/CCD in which was imaged. For the Omega-2000 camera, this process is not necessary as it only contains a unique CCD.

Throughout this work, the mass-weighted ages and metallicities are preferred to the luminosity ones, because of the mass-weighted parameters are more representative of the total stellar content of the galaxy and they are not linked to a definition luminosity weight (which may easily differ among different works); although luminosity-weighted parameters are also estimated. In fact, a young population can dominate the luminosity of a galaxy, and consequently its luminosity weighted age, even when its contribution in mass is very low (Trager et al. 2000; Conroy 2013; Vazdekis et al. 2016).

Table 1 illustrates part of the stellar-population parameters and uncertainties derived by MUFFIT using BC03 for our sample of quiescent galaxies (see Sect. 3 below) used throughout this research.

3. Definition of the quiescent sample

The definition of a reliable sample of quiescent galaxies with low levels of contamination may be a sensitive and tricky process, because both dusty star-forming galaxies and cool stars in ground-based surveys present colours similar to those of the quiescent galaxy population. The contamination of these sources can represented a substantial part of the sample at certain redshift and mass ranges and their effects should be removed or minimised at least (see Sects. 3.1–3.4). Even though multi-filter photometric surveys, which are not biased by selection effects other than the photometric depth, the definition of a complete sample in stellar mass (Sect. 3.5) with accurate enough photo- z predictions (Sect. 3.6) is key to reliably drive this study, be-

⁴ <http://www.caha.es/CAHA/Instruments/020000>

⁵ <http://www.caha.es>

⁶ <http://cosmo.iaa.es/content/alhambra-gold-catalog>

⁷ MULTI-FILTER FITting for stellar population diagnostics

Table 1. Stellar-population parameters of the sample of quiescent galaxies using BC03 SSP models. From left to right: ALHAMBRA source ID, right ascension, declination, magnitude in the detection band, photometric redshift, stellar mass, extinction, mass weighted age and metallicity, $m_{F365} - m_{F551}$ and $m_{F551} - J$ rest-frame colours (labeled as $U - V$ and $V - J$ respectively) and their values after dust correction (intrinsic colours), and average signal-to-noise ratio. The parameter uncertainties are attached below each quantity.

SourceID 814–	RA [deg]	DEC [deg]	m_{F814W} [AB]	z	$\log_{10} M_{\star}$ [M_{\odot}]	A_V [AB]	Age _M [Gyr]	[M/H] _M [dex]	$U - V$ [AB]	$V - J$ [AB]	$(U - V)_{\text{int}}$ [AB]	$(V - J)_{\text{int}}$ [AB]	$< S/N >$
62402442	214.4301	52.3397	16.71 ±0.02	0.119 ±0.003	10.66 ±0.05	0.27 ±0.07	4.5 ±1.3	−0.24 ±0.15	1.88 ±0.04	1.24 ±0.02	1.73 ±0.04	1.09 ±0.05	40.64
62300829	213.5037	52.3945	16.53 ±0.02	0.100 < 0.001	10.64 ±0.08	0.08 ±0.08	6.0 ±2.4	−0.05 ±0.17	1.91 ±0.02	1.20 ±0.02	1.87 ±0.05	1.16 ±0.05	39.73
74405663	243.0770	54.1213	17.10 ±0.02	0.119 ±0.003	10.55 ±0.04	0.15 ±0.16	4.1 ±0.5	−0.20 ±0.10	1.78 ±0.04	1.19 ±0.02	1.68 ±0.20	1.10 ±0.09	39.52
22202797	36.8434	1.1945	17.31 ±0.02	0.104 ±0.007	10.33 ±0.10	0.10 ±0.08	5.2 ±1.9	−0.15 ±0.20	1.86 ±0.06	1.14 ±0.03	1.80 ±0.06	1.09 ±0.05	38.77
74103404	243.0550	54.6608	17.14 ±0.02	0.230 < 0.001	11.31 ±0.04	0.02 ±0.05	5.4 ±0.9	0.12 ±0.16	1.89 ±0.02	1.24 ±0.02	1.87 ±0.04	1.22 ±0.03	38.69
21205253	37.0285	1.1497	17.37 ±0.02	0.136 ±0.005	10.66 ±0.08	0.07 ±0.09	7.8 ±2.0	−0.05 ±0.16	1.96 ±0.04	1.18 ±0.03	1.93 ±0.05	1.14 ±0.06	38.66
74401062	243.1835	54.2408	18.02 ±0.02	0.140 ±0.001	10.33 ±0.06	0.13 ±0.09	4.8 ±1.5	−0.12 ±0.13	1.86 ±0.02	1.12 ±0.02	1.79 ±0.05	1.05 ±0.06	38.64
74405753	243.1381	54.1192	17.97 ±0.02	0.151 ±0.004	10.47 ±0.06	0.11 ±0.10	5.0 ±1.6	0.03 ±0.13	1.94 ±0.03	1.23 ±0.02	1.88 ±0.06	1.17 ±0.06	38.61
74406006	243.2873	54.1121	17.14 ±0.02	0.144 ±0.006	10.80 ±0.10	0.13 ±0.11	7.1 ±2.2	0.02 ±0.15	1.99 ±0.05	1.23 ±0.03	1.92 ±0.07	1.16 ±0.07	38.59
51406997	189.5499	61.7978	16.77 ±0.02	0.108 ±0.007	10.59 ±0.09	0.15 ±0.10	6.7 ±2.4	−0.04 ±0.14	1.97 ±0.06	1.20 ±0.03	1.88 ±0.07	1.11 ±0.07	38.57
74101458	243.4018	54.7131	17.64 ±0.02	0.140 < 0.001	10.58 ±0.03	0.02 ±0.04	5.3 ±0.8	−0.22 ±0.14	1.74 ±0.02	1.18 ±0.02	1.73 ±0.02	1.17 ±0.03	38.41
51210550	188.7010	62.2081	17.53 ±0.02	0.110 ±0.002	10.26 ±0.05	0.02 ±0.04	5.3 ±1.1	−0.19 ±0.23	1.79 ±0.04	1.14 ±0.02	1.78 ±0.04	1.13 ±0.03	38.31
74104138	243.0991	54.6405	17.40 ±0.02	0.206 ±0.006	11.16 ±0.07	0.11 ±0.11	7.2 ±2.2	0.07 ±0.10	2.04 ±0.05	1.21 ±0.03	1.98 ±0.07	1.15 ±0.06	38.30
41401013	150.4250	2.0662	15.98 ±0.02	0.133 ±0.006	11.02 ±0.11	0.17 ±0.07	4.1 ±2.4	0.13 ±0.19	1.88 ±0.04	1.26 ±0.02	1.79 ±0.05	1.16 ±0.05	38.26
74406197	243.3334	54.1071	17.96 ±0.02	0.156 ±0.005	10.48 ±0.07	0.06 ±0.08	4.6 ±1.1	0.10 ±0.16	1.88 ±0.05	1.19 ±0.03	1.85 ±0.04	1.16 ±0.05	38.25
73400609	243.4698	54.2539	17.54 ±0.02	0.142 ±0.005	10.64 ±0.06	0.04 ±0.07	7.0 ±1.8	−0.11 ±0.12	1.92 ±0.05	1.18 ±0.04	1.91 ±0.04	1.16 ±0.04	38.12
74408909	243.4100	54.0274	16.64 ±0.02	0.145 ±0.006	11.03 ±0.07	0.06 ±0.09	7.6 ±1.9	−0.18 ±0.13	1.92 ±0.06	1.17 ±0.04	1.88 ±0.06	1.14 ±0.07	38.06
74104674	243.3939	54.6296	18.24 ±0.02	0.220 ±0.001	10.73 ±0.10	0.05 ±0.08	5.1 ±2.0	0.08 ±0.12	1.93 ±0.02	1.12 ±0.02	1.90 ±0.06	1.10 ±0.05	38.04
22102185	37.3262	1.2085	18.41 ±0.02	0.250 ±0.004	10.74 ±0.08	0.12 ±0.10	4.0 ±1.5	0.16 ±0.13	1.96 ±0.04	1.22 ±0.03	1.89 ±0.06	1.15 ±0.06	38.00
74108616	243.0808	54.5163	18.12 ±0.02	0.120 ±0.001	10.23 ±0.03	0.02 ±0.04	6.1 ±0.8	−0.43 ±0.11	1.71 ±0.02	1.12 ±0.02	1.70 ±0.03	1.10 ±0.04	37.98

Notes. Additional columns and galaxies will be available at http://archive.cefca.es/alhambra/quiescent_galaxies_query.html . Only a portion of the table is shown in the printed version for illustrating purposes.

cause the stellar mass is tightly related to the star formation history of each galaxy (e. g. Cowie et al. 1996; Trager et al. 2000; Tremonti et al. 2004; Gallazzi et al. 2005, 2006; Jimenez et al. 2007; Panter et al. 2008; González Delgado et al. 2014).

3.1. The dust corrected UVJ -diagram

There are many similar relations that define a sample of quiescent galaxies based on colour-magnitude diagrams (CMD, Bell et al. 2004; Baldry et al. 2004; Brown et al. 2007), in SFR-mass relations (Moustakas et al. 2013), in colour-mass relations (Peng et al. 2010), or in colour-colour diagrams (Daddi et al. 2004; Williams et al. 2009; Arnouts et al. 2013) usually defined at rest-frame. During the last years, the UVJ colour-colour diagram (e. g. Williams et al. 2009) has become one of the most extended methods for separating the quiescent galaxy population from the galaxies that lie on the blue cloud or star forming population. However, UVJ diagrams present a non-negligible level of contamination in the selection of quiescent galaxies that depends on redshift and stellar mass (Williams et al. 2009; Moresco et al. 2013).

For the aims of this work, it is therefore crucial to diminish the contamination of dust-reddened star-forming galaxies in our sample. Otherwise, the sample would contain a subset of younger and obscured galaxies, that differs from the largely evolved quiescent galaxies. To make a more reliable sample selection, we took advantage of the stellar population results provided by MUFFIT. We used the k -corrections along with the extinction values to build a new and improved version of the UVJ -diagram free of dust colour effects, which allows us to clean the quiescent sample of obscured star-forming galaxies. In brief, MUFFIT retrieves a set of SSP mixtures with different weights and parameters after fitting the SED of each galaxy from the ALHAMBRA dataset, in which the extinction is included. From these mixtures, it is straightforward to rebuild the same combination of models (in a general case age, metallicity, IMF, overabundances, stellar mass, and the weight of each SSP component in the mixture), at rest-frame and null extinction ($A_V = 0.0$).

Instead of using the rest-frame $U - V$ and $V - J$ colours in order to build the UVJ -diagram, we took the bands $F365W$, $F551W$, and J from ALHAMBRA to compute the rest-frame colours $m_{F365} - m_{F551}$ and $m_{F551} - J$, which are the most similar bands to the U , V , and J effective wavelengths. As expected, see Fig. 1, the empirical bimodality is also present using these bands. In Fig. 1, we present the UVJ -diagram made with the ALHAMBRA bands mentioned previously for all the galaxies at $0.1 \leq z \leq 1.1$ in the ALHAMBRA Gold catalogue (complete down to $m_{F814W} = 23$) and corrected of reddening. By looking at the distribution of the rest-frame intrinsic colour $(m_{F365} - m_{F551})_{\text{int}}$ (see top inner panels in Fig. 1), we can easily set the limit for quiescent galaxies as $(m_{F365} - m_{F551})_{\text{int}} \geq 1.5$, that is roughly constant with redshift, at least up to $z \sim 1.1$. Although this colour limit is not strictly located in the minimum between the red and blue peaks (corresponding to the quiescent and star-forming population respectively), its value was defined to agree with the limit established in Moresco et al. (2013, see Eq. 1 below) and to be slightly larger as to avoid the (now) poorly populated green valley, whose limits are difficult to define due to the low number of sources. In fact, after the definition of a quiescent sample complete in stellar mass (Sect. 3.5 below), the sample remains almost unaltered. For comparison reasons, we present the UVJ -diagram without the extinction correction in the bottom panels of Fig. 1. The range of colours in the UVJ -diagram to select the quiescent sample defined by Moresco et al. (2013) is

also plotted, which is less contaminated of obscured star-forming galaxies than the proposed by Williams et al. (2009). Formally,

$$\begin{cases} (m_{F365} - m_{F551}) > 0.88 \times (m_{F551} - J) + 0.69, & \text{for } z \leq 0.5 \\ (m_{F365} - m_{F551}) > 0.88 \times (m_{F551} - J) + 0.66, & \text{for } z > 0.5 \end{cases} \quad (1)$$

where $m_{F365} - m_{F551} > 1.6$ ($m_{F365} - m_{F551} > 1.5$) at $z \leq 0.5$ ($z > 0.5$) and $m_{F551} - J < 1.6$, all quantities at rest-frame and in AB-magnitudes.

Independently of the SSP model set used, BC03 and EMILES, the simple extinction correction applied on the UVJ colours yields striking results:

- As expected, removing dust effects makes clearer the colour bimodality of galaxies in the UVJ -diagram (see Fig. 1). This is because a very considerable part of the galaxies that reside in the green valley (the bridge between red and blue galaxies) are obscured star-forming galaxies ($\sim 65\%$). Their intrinsic colour $(m_{F365} - m_{F551})_{\text{int}}$ (see insets in Fig. 1) unveils that these galaxies really lie on the star-forming population, although they also present a large dust content that reddens their observed colours (Brammer et al. 2009; Whitaker et al. 2010, obtained a similar result for $U - V$). Thereby, the green valley is largely depopulated after accounting for extinction (inner panels in Fig. 1; see also Bell et al. 2005; Cowie & Barger 2008; Brammer et al. 2009; Cardamone et al. 2010).
- At least for a sample complete down to $m_{F814W} = 23$, the histogram of the $(m_{F365} - m_{F551})_{\text{int}}$ colour exhibits a local minimum at ~ 1.45 that can be imposed as the bluest colour limit to fairly select the quiescent sample in ALHAMBRA. This limit to separate quiescent from star-forming galaxies also remains roughly constant since $z \leq 1.1$, and it does not present any remarkable evolution. In spite of the presence of a bridge between the bulk of intrinsic red and blue galaxies at $(m_{F365} - m_{F551})_{\text{int}} \sim 1.45$, this colour range is not largely populated by many galaxy and it looks to be restricted for a few ones only.
- Additionally, we can see that the galaxies labelled as quiescent by Eq. 1 and that belong to the star-forming sample after the dust correction (intrinsic $m_{F365} - m_{F551} < 1.5$, black dots in Fig. 1) are typically concentrated close to the edges of Eq. 1, supporting the reliability of the extinction values provided by MUFFIT. Otherwise, the distribution of dust-reddened galaxies would uniformly populate the red part of the UVJ diagram as a consequence of degeneracies, where the effects of age, metallicity and extinction on the stellar continuum were not properly differentiated.
- Dusty star forming galaxies comprise the $\sim 20\%$ of the quiescent sample defined through Eq. 1. Our results clearly established that more massive quiescent galaxies are less biased by dusty star forming galaxies than the less massive ones (see Fig. 2 as well). More precisely, the most massive part of the sample is weakly contaminated by dusty star-forming galaxies when they are defined by Eq. 1 ($\log_{10} M_{\star} \geq 11$, 2–8 % from $z \sim 0.1$ to $z \sim 1.1$), while the low mass ones may be significantly biased by them (e. g. $\sim 40\%$ for $9.2 \leq \log_{10} M_{\star} \leq 9.6$ at $0.1 \leq z \leq 0.3$).

In addition to the colour cut $(m_{F365} - m_{F551})_{\text{int}} \geq 1.5$, we restrict this study to the redshift interval $0.1 \leq z \leq 1.1$ because: i) the stellar mass completeness constraint largely reduces the number of quiescent galaxies further than $z > 1.1$; ii) at $z < 0.1$,

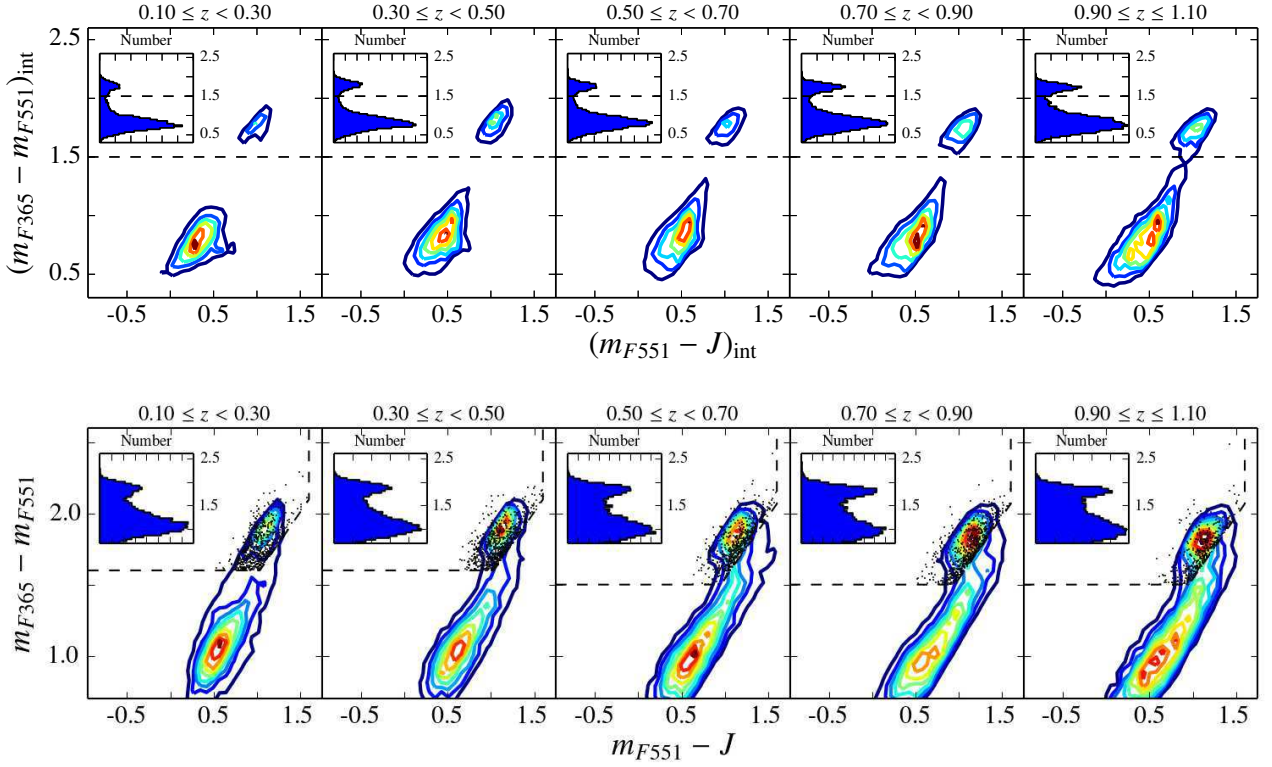


Fig. 1. *Top panels* illustrate the density surface of rest-frame intrinsic colours $(m_{F551} - J)_{\text{int}}$ (X-axis) and $(m_{F365} - m_{F551})_{\text{int}}$ (Y-axis) after correcting for extinction at different redshifts, whereas *bottom panels* are rest-frame colours without removing dust effects, both obtained by BC03 SSP models. Redder (bluer) density-curve colours are related to high (low) densities. *Inner panels*, histograms of the intrinsic (*top*) and observed (*bottom*) rest-frame colour $m_{F365} - m_{F551}$. Dashed lines in *top panels* illustrate our limiting value $(m_{F365} - m_{F551})_{\text{int}} = 1.5$ for quiescent galaxies, and in the *bottom panel* the quiescent *UVJ*-sample defined by Moresco et al. (2013, Eq. 1). Black dots are galaxies defined as quiescent with the *UVJ*-criteria of Moresco et al. (2013) that lie in the star-forming region after taking their extinctions into account.

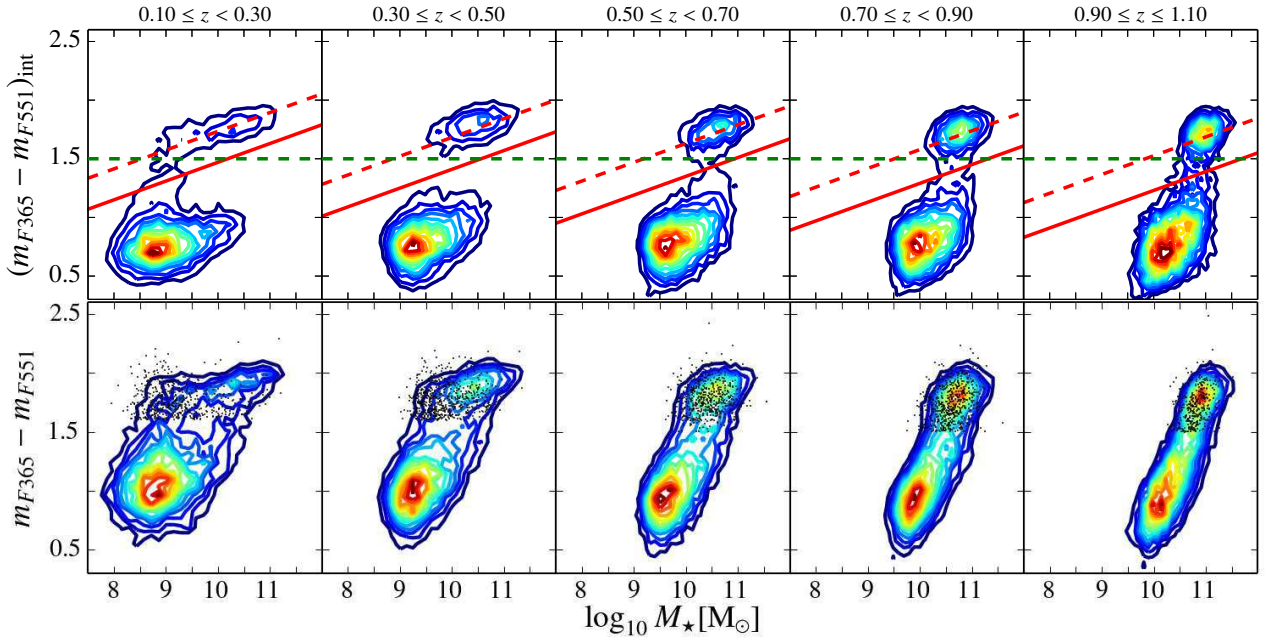


Fig. 2. *Top panels* illustrate the density surface of stellar mass (X-axis) and the rest-frame intrinsic colour $(m_{F365} - m_{F551})_{\text{int}}$ (Y-axis) after correcting for extinction at different redshifts, whereas *bottom panels* are rest-frame colours without removing dust effects, all obtained by BC03 SSP models. Redder (bluer) density-curve colours are related to high (low) densities. Dashed lines in *top panels* illustrate the limiting value $(m_{F365} - m_{F551})_{\text{int}} = 1.5$ used for selecting quiescent galaxies in Sect. 3.1. Black dots are galaxies defined as quiescent with the *UVJ*-criteria of Moresco et al. (2013) that lie in the star-forming region after taking their extinctions into account. Dashed and solid red lines show the fit to the quiescent sequence, $(m_{F365} - m_{F551})_{\text{int}}^{\text{Q}}$, and the limiting intrinsic colours, $(m_{F365} - m_{F551})_{\text{int}}^{\text{lim}}$, values of quiescent galaxies respectively (see details in Sect. 3.2).

the number of quiescent galaxies in ALHAMBRA is also very low, specially for the most massive ones, which are substantially less frequent. Taking as reference the predictions from BC03 SSP models (the retrieved A_V values can differ amongst SSP models), the total number of quiescent galaxies at this point is 14 944.

3.2. The stellar mass-colour diagram corrected for extinction

One of the main goals of UVJ -like diagrams was to reduce the number of dusty star-forming galaxies (hereafter DSF) in quiescent galaxy samples (see e. g. Moresco et al. 2013). Whilst these diagrams include a couple of colours that empirically split the loci of quiescent and star-forming galaxies, we do not exactly know whether UVJ diagrams are biasing in stellar mass the sample of quiescent galaxies or not. This is because these diagrams only include a couple of colours to select them, where physical parameters such as stellar mass are ignored and the overlap between both populations also complicates the sample selection. However, our analysis techniques also include the extinction as another stellar population parameter. This allows us to take advantage to build alternative diagrams for separating galaxies in quiescent and star-forming ones, as well as to confront UVJ diagrams with more sophisticated or physical methods.

In particular, we explore the rest-frame stellar mass-colour diagram corrected for extinction (MCDE). This "new" diagram is conceived to both unmask the dust-reddened star-forming galaxies and include the stellar mass of galaxies (physical parameter) avoiding any bias in the sample selection. The MCDE diagram is actually a step forward or improvement respect classical CMD diagrams (e. g. Bell et al. 2004; Baldry et al. 2004; Brown et al. 2007, where absolute magnitude is tightly linked to stellar mass) or the stellar mass-colour diagram (e. g. Peng et al. 2010, see also bottom panels in Fig. 2), which are typically contaminated by DSF. As expected, the MCDE makes clearer the colour bimodality of galaxies, see Fig. 2, where the dust-corrected colour $(m_{F365} - m_{F551})_{\text{int}}$ is key to disentangle red sources that are actually dusty star forming galaxies (see black dots in Fig. 2). Otherwise, disentangling DSF via colour-colour diagrams or CMD is not completely reliable. Again, the presence of galaxies in the green valley is much rarer, pointing out the large presence of DSF in the green valley colour range (non dust corrected). Figure 2 shows that the colour cut $(m_{F365} - m_{F551})_{\text{int}} \geq 1.5$ defined in Sect. 3.1 properly select quiescent galaxies at first order up to $z \sim 1$ and $m_{F814} \leq 23$ for this work. Although we face this issue in more detail in Sect. 6.2 for a general case. To define the colour limit of the quiescent galaxy population, red solid line in Fig. 2, we follow a process of three steps:

- i) From the distribution of ALHAMBRA galaxies on the MCDE, we define a set of straight lines to separate both populations by eye. As in Sect. 3.1, we focus on the redshift range $0.1 \leq z \leq 1.1$, which is divided in bins of $\Delta z = 0.2$.
- ii) For each of the bins defined above, we performed a least square fitting with all the quiescent galaxies above the subsample defined by eye in the previous step, that is, the red galaxies in the MCDE. For the fit, we assume a linear dependence of the intrinsic colour $(m_{F365} - m_{F551})_{\text{int}}$ with the stellar mass. The results from the least square fits show that the slope of the quiescent sequence in this diagram is compatible with a constant value. However, the ordinate changes with redshift. This is not surprising, because it is well known that the colour of galaxies evolve with cosmic time. As intrinsic colours depends on the input set of SSP models, the

least square fitting is repeat for the three sets of SSP models. At the redshift range $0.1 \leq z \leq 1.1$ and assuming a constant slope, we find that the relation between the intrinsic colour $(m_{F365} - m_{F551})_{\text{int}}$ and the stellar mass of quiescent galaxies is well expressed for BC03 SSP models by:

$$(m_{F365} - m_{F551})_{\text{int}}^Q = 0.16 (\log_{10} M_{\star} - 10) - 0.26(z - 0.1) + 1.76, \quad (2)$$

where $(m_{F365} - m_{F551})_{\text{int}}^Q$ is the representative colour $(m_{F365} - m_{F551})_{\text{int}}$ of quiescent galaxies at stellar mass M_{\star} . Likewise we repeat the process for EMILES SSP models for both BaSTI and Padova00 isochrones, respectively obtaining that:

$$(m_{F365} - m_{F551})_{\text{int}}^Q = 0.15 (\log_{10} M_{\star} - 10) - 0.24(z - 0.1) + 1.73, \quad (3)$$

$$(m_{F365} - m_{F551})_{\text{int}}^Q = 0.15 (\log_{10} M_{\star} - 10) - 0.19(z - 0.1) + 1.75. \quad (4)$$

Equations 2-4 illustrate that there exist discrepancies between SSP models. Nevertheless, these discrepancies are more remarkable between BC03 and EMILES+Padova00 SSP model sets, whereas for BC03 and EMILES+BaSTI are almost negligible.

- iii) Finally, we define the colour limits that can exhibit quiescent galaxies as a function of their stellar masses. To define this limit, we assume that it is also of the form $(m_{F365} - m_{F551})_{\text{int}} \propto 0.15 - 0.16$, i. e. the same dependence with mass than Eqs. 2-4. Under this assumption, the MCDE can be easily rotated by Eqs. 2-4 as

$$(m_{F365} - m_{F551})_{\text{int}}^{\text{rot}} = (m_{F365} - m_{F551})_{\text{int}} - (m_{F365} - m_{F551})_{\text{int}}^Q. \quad (5)$$

The distributions $(m_{F365} - m_{F551})_{\text{int}}^{\text{rot}}$ can be properly fitted by a Log-normal distribution (see Appendix C for details), where typical uncertainties of colour $(m_{F365} - m_{F551})_{\text{int}}$ are ~ 0.07 . Motivated by removing the effects of uncertainties, which vary with redshift, in the $(m_{F365} - m_{F551})_{\text{int}}^{\text{rot}}$ distribution, we adopted the maximum likelihood method (MLE) developed by López-Sanjuan et al. (2014, further details in Appendix C). From the fits provided by the MLE method, we can set the range of $(m_{F365} - m_{F551})_{\text{int}}^{\text{rot}}$ values at redshifts $0.1 \leq z \leq 1.1$, to subsequently set limits in the $(m_{F365} - m_{F551})_{\text{int}}$ values for quiescent galaxies. We define the maximum $(m_{F365} - m_{F551})_{\text{int}}$ value of quiescent galaxies as the 3σ limit (redshift dependent a priori) of the Log-normal distribution derived from the MLE. This limit closely lie on the limits set by eye, but it is mathematically motivated now. For BC03 SSP models, the limiting intrinsic colour $(m_{F365} - m_{F551})_{\text{int}}$ of quiescent galaxies is expressed as follows:

$$(m_{F365} - m_{F551})_{\text{int}}^{\text{lim}} = 0.16 (\log_{10} M_{\star} - 10) - 0.30(z - 0.1) + 1.50, \quad (6)$$

whereas for EMILES+BaSTI and EMILES+Padova00 are respectively:

$$(m_{F365} - m_{F551})_{\text{int}}^{\text{lim}} = 0.15 (\log_{10} M_{\star} - 10) - 0.24(z - 0.1) + 1.46, \quad (7)$$

$$(m_{F365} - m_{F551})_{\text{int}}^{\text{lim}} = 0.15 (\log_{10} M_{\star} - 10) - 0.13(z - 0.1) + 1.47. \quad (8)$$

3.3. Visual inspection

To increase the purity of the sample, we also carried out an individual inspection of the $\sim 15\text{k}$ galaxies with intrinsic red colours retrieved above and in the interval $0.1 \leq z \leq 1.1$. We removed from the sample those galaxies for which their photometry presented significant irregularities or that were compromised by really nearby sources, imaged in bad CCD regions, or spurious detections. To develop this process, we simultaneously checked one-by-one all the galaxy stamps, the adequacy of the photometric aperture (mainly the efficiency on the detection-deblending of sources and surroundings), and that the photo-spectrum did not present strong irregularities as the presented by time-variable sources or sources close to stellar spikes, which cannot be reproduced by stellar population models. Finally, we removed from the quiescent sample $\sim 5\%$ of sources after the visual inspection, remaining 14 235 quiescent galaxies at this stage (BC03 SSP models as reference).

3.4. Faint star removal

The ALHAMBRA Gold catalogue provides a statistical star/galaxy classification for discerning if each source in the catalogue is either a galaxy or a star (*Stellar_flag*, more detailed in Molino et al. 2014). This parameter was originally used to define our sample of galaxies (see Sect. 2) and it accounts for the morphology, apparent magnitude, and two colours to provide a statistical approach to carry out the star/galaxy separation for each detection. Unfortunately, this parameter is less effective at decreasing signal-to-noise-ratio, and consequently, for sources fainter than $m_{F814W} = 22.5$ this classification is uncertain and a value *Stellar_flag* = 0.5 is assigned. Although we do not expect a large number of contamination from stars at $22.5 \leq m_{F814W} < 23$ for the full sample, the ALHAMBRA fields may contain stars from the Milky Way halo, which are mainly composed of cool red stars. Our quiescent sample, composed of red sources, may be therefore partly contaminated by stars that were analysed as galaxies.

This problem is faced through a new MUFFIT module devoted to analysing stars, which carries out a similar SED-fitting process to the galactic version but using the Coelho et al. (2005) star models instead. This methodology ends up reducing the contamination of faint stars in ALHAMBRA from 24 % to 4 % after comparing our faint star detection predictions with the star/galaxy classification provided by COSMOS (classified as point-like sources thanks for its tiny PSF; Leauthaud et al. 2007), in a shared subsample of sources at $22.5 \leq m_{F814W} < 23$. It is worth mentioning that owing to the spectral coverage of the Coelho et al. (2005) stellar models (300 nm – 1.8 μm), the K_s photometry of the ALHAMBRA band is not used for the stellar analysis. A more detailed explanation about the whole process is provided in Appendix A, as well as the comparison with COSMOS to check the reliability of the methodology.

After removing 439 star candidates from the sample in the range $22.5 \leq m_{F814W} < 23$, the number of quiescent galaxies is reduced to 13 796.

3.5. Stellar mass completeness

We model the stellar mass completeness, C , through a Fermi-Dirac distribution (see Appendix B) that is parametrised by two redshift-dependent parameters, M_F and Δ_F . We find out that this kind of distribution reproduces the decay on the less massive galaxies of our flux-limited sample ($m_{F814W} \leq 23$) at any redshift

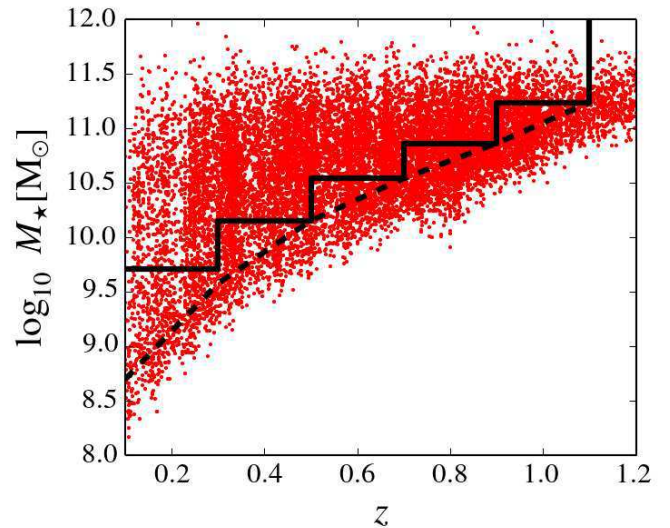


Fig. 3. Redshifts (X-axis) and stellar masses (Y-axis) of the sample of ALHAMBRA quiescent galaxies. The dashed line shows the 95 % stellar mass completeness level of quiescent galaxies from the ALHAMBRA Gold catalogue (complete down to $m_{F814W} = 23$). The solid line illustrates the limits assumed in this work to define our sample of galaxies complete in stellar mass at different redshift bins (see Sect.3).

properly (see Appendix B.1). Briefly, M_F is the stellar mass value in dex units for which the completeness reaches 50 % ($C = 0.5$), while Δ_F is related with the rate of decrease on the number of galaxies. The process for deriving these parameters takes advantage of stellar mass functions from deeper surveys (for further details, see Appendix B.2), in particular from the COSMOS survey, which specifically provides them for quiescent galaxies (Ilbert et al. 2010, computed using BC03 SSP models) and partly overlaps with ALHAMBRA. In this process, we assume that any discrepancy between the low-mass end of the ALHAMBRA stellar mass function and the COSMOS one is led by the mass incompleteness. These differences allow us to determine both M_F and Δ_F , that are directly related to the stellar mass limit, $\log_{10} M_C$, at certain redshift z and completeness level by

$$\log_{10} M_C(z) = \Delta_F(z) \ln [(1 - C) - 1] + M_F(z). \quad (9)$$

For this work, we require a conservative stellar mass completeness of at least $C = 0.95$ at any redshift slice (see Fig. 3 and values in Table 2). From Table 2, we derive that ALHAMBRA is complete down to $\log_{10} M_* \geq 9.4$ dex at $z = 0.3$. However, to develop this work, we rise the low-mass limit down to $\log_{10} M_* \geq 9.6$ dex, with the only aim of having a set of equal-size stellar mass bins of ~ 0.4 dex. In Appendix B, there is a more detailed and complete explanation of the full process to determine the ALHAMBRA completeness. When stellar masses are retrieved using MUFFIT and EMILES SSP models, their values differ with respect the one obtained using BC03 SSP models. EMILES stellar masses are systematically larger by about 0.15 and 0.11 dex for BaSTI and Padova00 isochrones, respectively. To determine the stellar mass completeness of EMILES predictions, we add 0.15 (EMILES+BaSTI) and 0.11 dex (EMILES+Padova00) to the M_F values provided in Table 2, whereas Δ_F remain unaltered. We check that this shift analytically reproduce the observed stellar masses properly.

Finally, the total balance of galaxies for this study, including the stellar mass completeness constraint, comprises a total of $\sim 8\,500$ quiescent galaxies for BC03 SSP models (all the galaxies

Table 2. The parameters M_F and Δ_F at different redshift, and the stellar mass limit at the completeness level $C = 0.7, 0.8, 0.9$, and 0.95 for the quiescent sample and BC03 SSP models (details in text).

Redshift	0.3	0.5	0.7	0.9	1.1
M_F	8.99	9.64	10.08	10.44	10.84
Δ_F	0.132	0.108	0.105	0.110	0.108
$\log_{10} M_{C=0.7}$	9.10	9.73	10.17	10.53	10.93
$\log_{10} M_{C=0.8}$	9.17	9.79	10.23	10.59	10.99
$\log_{10} M_{C=0.9}$	9.28	9.88	10.31	10.68	11.07
$\log_{10} M_{C=0.95}$	9.38	9.96	10.39	10.76	11.15

Notes. Parameters for EMILES SSP models are obtained adding 0.15 and 0.11 dex to M_F for BaSTI and Padova00 isochrones respectively. For EMILES, Δ_F is equal to the BC03 ones.

in our sample are enclosed by the black solid line in Fig. 3). The number of quiescent galaxies per stellar mass and redshift bin is detailed in Table 3. For EMILES SSP models, the final number of quiescent galaxies for this work is $\sim 8\,100$.

3.6. The photo- z accuracy of the quiescent sample

An accurate photo- z determination is essential to properly drive a stellar population study, otherwise any stellar-population prediction may be erroneous. As we mention above, we applied the accurate photo- z constraints provided in the ALHAMBRA Gold catalogue (computed using BPZ2.0, Benítez 2000; Molino et al. 2014), to subsequently run MUFFIT in the photo- z intervals provided in this catalogue, that is, treating the redshift as another free parameter to determine in our stellar population analysis. Despite MUFFIT is not a photo- z code, the combined use of both photo- z constraints from dedicated photo- z codes and MUFFIT has demonstrated to be a reliable method that improves the photo- z predictions $\sim 15\%$ (see Díaz-García et al. 2015), and it is necessary to check its reliability and accuracy.

The methodology to determine the level of accuracy for the photo- z predictions provided by MUFFIT (after using as priors the photo- z constraints from the Gold catalogue), is based on all the galaxies in our final sample with publicly available spectroscopic redshifts from surveys (zCOSMOS, Lilly et al. 2009; AEGIS, Davis et al. 2007; and GOODS-N, Cooper et al. 2011) that overlap with ALHAMBRA (from the catalogue of Molino et al. 2014). As there is no unique method to set numerical values of the photo- z accuracy, we turned to various statistics already used in the literature. One of the most extended is the normalised median absolute deviation (σ_{NMAD} , Brammer et al. 2008), since this is less affected of catastrophic errors or outliers. Formally,

$$\sigma_{\text{NMAD}} = 1.48 \times \text{median} \left(\frac{|\Delta z - \text{median}(\Delta z)|}{1 + z_{\text{spec}}} \right), \quad (10)$$

where $\Delta z = z_{\text{phot}} - z_{\text{spec}}$. Moreover, we complement our results proposing another photo- z accuracy estimator: the RMS of the Gaussian distribution built from the values $\Delta z/(1 + z_{\text{spec}})$, which in the following, we denote as $\sigma_{\text{photo-}z}$. The number of catastrophic outliers is also a noted factor to take into account, so we include two estimators for it

$$\eta_1 = \frac{|\Delta z|}{1 + z_{\text{spec}}} > 0.2, \text{ and} \quad (11)$$

$$\eta_2 = \frac{|\Delta z|}{1 + z_{\text{spec}}} > 5 \times \sigma_{\text{NMAD}}. \quad (12)$$

Amongst the 8 547 quiescent galaxies in our sample complete in luminosity ($m_{F814W} \leq 23$) and in stellar mass (see Sect. 3.5 above), there are 576 quiescent galaxies with spectroscopic redshift measurements. Figure 4 illustrates the one-to-one comparison (top panel) of the 576 quiescent galaxies, showing the excellent agreement between our photometric predictions and the spectroscopic ones. For this subsample of 576 galaxies and according to Eqs. 10–12, we obtained $\sigma_{\text{NMAD}} = 0.0064$, $\eta_1 = 0.5\%$, and $\eta_2 = 6.6\%$ respectively; whereas for the $\Delta z/(1 + z_{\text{spec}})$ distribution we carried out a good fit to a Gaussian function (red solid line in middle panel in Fig. 4) centred at 0.0006 (i. e. closely centred to zero and without a systematic shift) and with a RMS or $\sigma_{\text{photo-}z} = 0.0053$.

If we compare the photo- z values provided by BPZ in the ALHAMBRA Gold catalogue with the spectroscopic ones, we obtain an accuracy of $\sigma_{\text{NMAD}} = 0.0080$, $\sigma_{\text{photo-}z} = 0.0062$, $\eta_1 = 0.5\%$, and $\eta_2 = 7.1\%$. Thereby, treating the photo z as another free parameter for MUFFIT, in the ranges provided by BPZ, improves the photo- z accuracy $\sim 15 - 20\%$. As checked by Díaz-García et al. (2015), a photo- z uncertainty at this level, 0.6% , has a minimum impact on the stellar population parameters that are determined via SED-fitting in ALHAMBRA: age, metallicity, and extinction.

4. Star formation rates via SED-fitting

By means of combination of two SSPs, we cannot estimate the SFR of galaxies directly, unlike SED-fitting analyses based on τ -models or in more complex SFH (e. g. Cid Fernandes et al. 2005; Moustakas et al. 2013). In order to retrieve SFRs from the SED-fitting results provided by MUFFIT, it is necessary to use the definition of a tracer or parameter that allow us to estimate them (Sect. 4.1). Although the SFR of quiescent galaxies are typically low, they can also be used to complement and reinforce the reliability of the results obtained in Sects. 3.1 and 3.2, opening an alternative process or criterion in order to support that the dust-reddened star-forming galaxies that exhibit UVJ -colours of quiescent galaxies (see Eq. 1) also show other features proper of star-forming galaxies, and therefore, they were removed from the quiescent sample properly. Specifically, we focus on the SFRs of the DSF to check that they present SFR values in the range of star-forming galaxies.

On the one hand, we present the methodology for computing SFRs using the SED-fitting results provided by MUFFIT using the ALHAMBRA data (Sect. 4.1), taking the luminosity at $2\,800\text{ Å}$ as SFR tracer, to subsequently compare the SFR of DSF with the rest of the sample. On the other hand, we studied the dust emission at $24\text{ }\mu\text{m}$ of all the DSF removed from the quiescent sample, that is, a tracer computed from MUFFIT SED-fitting results, which is also independent of the ALHAMBRA data (Sect. 4.2).

4.1. Star formation rates in ALHAMBRA: dusty star-forming galaxies

By means of model predictions of stellar populations, the UV continuum in the range $\lambda\lambda\,1\,500\text{--}2\,800\text{ Å}$ is a good tracer of SFR in galaxies with on-going star formation, because this range is mainly dominated by the light emitted by late-O and early-B stars (see e. g. Madau et al. 1998). In particular, we chose the SFR tracers proposed by Madau et al. (1998), which are based on stellar population models with exponentially declining SFRs, or τ models, and Salpeter (1955) IMF. Even though the SFR de-

Table 3. Number of quiescent galaxies per stellar mass and redshift bin. Last column summarizes the total number of galaxies per stellar mass bin. Last row shows the total number of quiescent galaxies per redshift bin. All the cells include redshift and stellar mass bins complete at the level $C = 0.95$, otherwise appear dashed.

	$0.1 \leq z < 0.3$	$0.3 \leq z < 0.5$	$0.5 \leq z < 0.7$	$0.7 \leq z < 0.9$	$0.9 \leq z \leq 1.1$	Total
$9.6 \leq \log_{10} M_{\star} < 10.0$	289	–	–	–	–	289
$10.0 \leq \log_{10} M_{\star} < 10.4$	433	996	–	–	–	1429
$10.4 \leq \log_{10} M_{\star} < 10.8$	403	1035	1088	–	–	2526
$10.8 \leq \log_{10} M_{\star} < 11.2$	238	663	800	1480	–	3181
$\log_{10} M_{\star} \geq 11.2$	51	140	157	357	417	1122
Total	1414	2834	2045	1837	417	8547

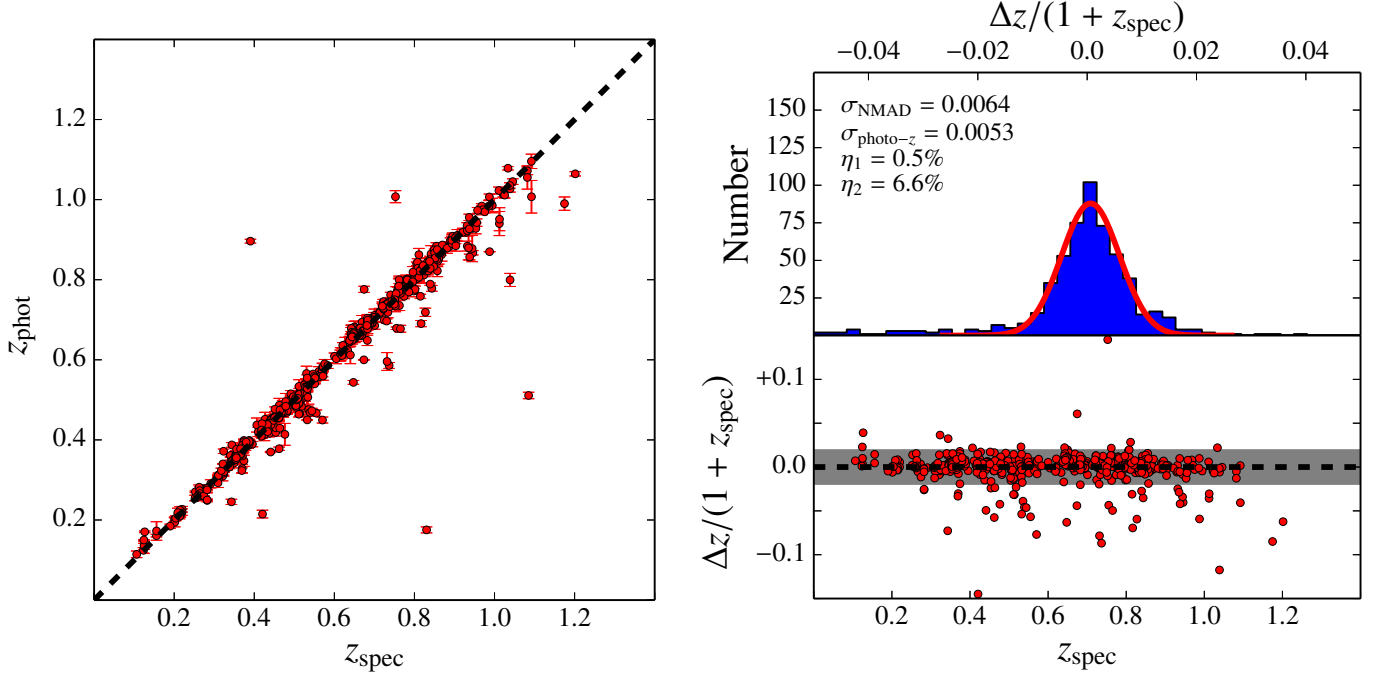


Fig. 4. Comparison of the photo- z provided by MUFFIT (z_{phot}) with their spectroscopic values (z_{spec}) for 576 quiescent galaxies in our sample. *Left panel*, comparison one-to-one of the redshifts, where the dashed black line is the one-to-one relation. *Top right panel* shows the histogram of values $\Delta z / (1 + z_{\text{spec}})$, along with the Gaussian that best fits this distribution (red solid line) and the photo- z accuracy estimators defined in the text (Eqs. 10–12). *Bottom right panel* exhibits the differences $\Delta z / (1 + z_{\text{spec}})$ as a function of the spectroscopic redshift (X -axis). Shaded region illustrates $3 \times \sigma_{\text{NMAD}}$ uncertainty.

rived from luminosities at 1500 \AA and τ -models is slightly less-dependent of the duration of the star-formation burst, the SFR derived along this section were computed from the rest-frame luminosity at 2800 \AA , $L_{2800\text{\AA}}^{z=0}$. Formally,

$$SFR_{2800\text{\AA}} = 1.27 \cdot 10^{-28} \times L_{2800\text{\AA}}^{z=0}, \quad (13)$$

where $L_{2800\text{\AA}}^{z=0}$ is in units of $\text{ergs s}^{-1} \text{ Hz}^{-1}$, and $SFR_{2800\text{\AA}}$ in $M_{\odot} \text{ yr}^{-1}$. Notice that Eq. 13 is not taking dust effects into account. The choice of the SFR tracer at 2800 \AA is motivated by the observational wavelength-frame of ALHAMBRA, because this starts at $\sim 3500 \text{ \AA}$ (band $F365$, $FWHM \sim 300 \text{ \AA}$ and effective wavelength $\lambda_{\text{eff}} = 3650 \text{ \AA}$). Therefore, the SFR tracer based on the luminosity at 2800 \AA is only matched at redshifts $z > 0.25$, whereas for 1500 \AA is at $z > 1.3$, which reduces our sample dramatically. Actually, for redshifts $z < 0.25$ we are able to obtain a prediction of the luminosity at 2800 \AA , but this prediction would be an extrapolation of the SED-fitting carried out by MUFFIT. For this section, we preferred a more conservative treatment in which the rest-frame flux at 2800 \AA must be included in the observational frame ($z \gtrsim 0.25$).

The rest-frame luminosity $L_{2800\text{\AA}}^{z=0}$, also free of dust attenuation, is calculated from the SED-fitting results provided by MUFFIT. Similarly to the process of removing the dust effects on colours (Sect. 3.1), we rebuilt the combination of best-fitting models retrieved during the Monte Carlo approach without extinction and for all the galaxies in ALHAMBRA. From these combination of models, we integrated the flux emitted in the rest-frame range $\lambda \lambda 2750\text{--}2850 \text{ \AA}$ in order to compute $L_{2800\text{\AA}}^{z=0}$ with its uncertainty and $SFR_{2800\text{\AA}}$ using Eq. 13.

In order to characterize the range of $SFR_{2800\text{\AA}}$ values of star-forming galaxies, as well as its dependence with redshift and stellar mass, we plotted the distribution $SFR_{2800\text{\AA}}$ versus stellar mass at different redshift bins. When viewed the full sample of ALHAMBRA galaxies in the SFR versus stellar mass plane, taking the stellar masses provided by MUFFIT, the already observed bimodality of star-forming and passive galaxies (e. g. Ilbert et al. 2010; Moustakas et al. 2013; Choi et al. 2014) appears, see Fig. 5. This figure also exhibits a tight correlation between the stellar mass and the SFR of the galaxy: the more massive, the larger the SFR of the galaxy independently of the spectral type (Daddi et al. 2007; Elbaz et al. 2007; Noeske et al.

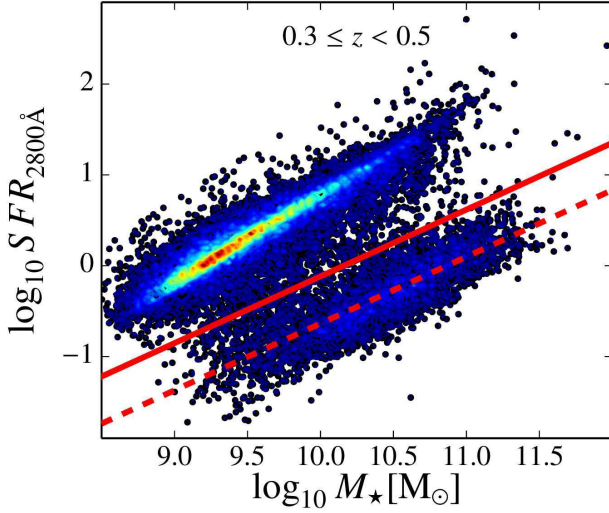


Fig. 5. Stellar mass (X-axis) versus star formation rate tracer $SFR_{2800\text{\AA}}$ (Y-axis) defined by Madau et al. (1998, see Eq. 13) of the ALHAMBRA galaxies at redshift $0.3 \leq z < 0.5$. Higher densities are presented by redder colours, whereas the lower ones by bluer colours. Dashed and solid red lines show the fit to the quiescent sequence and the limiting $SFR_{2800\text{\AA}}$ values for star-forming galaxies respectively.

2007; Moustakas et al. 2013). In order to separate both quiescent and star-forming populations, i. e. setting limiting $SFR_{2800\text{\AA}}$ values for quiescent and star-forming galaxies, we followed a similar process than the one detailed in Sect. 3.2:

- i) We took all the ALHAMBRA galaxies at the redshift range in which the rest-frame luminosity $L_{2800\text{\AA}}^{z=0}$ is in the observational wavelength-frame of ALHAMBRA, $0.3 \leq z \leq 1.1$. For each redshift bin, $\Delta z = 0.2$, the quiescent population is separated by a straight line that was established between both populations by eye.
- ii) From all the galaxies with $SFR_{2800\text{\AA}}$ below the limit established in the previous step for quiescent galaxies, we carried out an analytical fit of the population in each redshift bin assuming a linear dependence with stellar mass. Our results point out that the correlation between $\log_{10} SFR_{2800\text{\AA}}$ and stellar mass is compatible with no evolution in redshift. In the following, a relation of the form $\log_{10} SFR_{2800\text{\AA}} \propto 0.75 \log_{10} M_{\star}$ is assumed for any redshift providing that the $\log_{10} SFR_{2800\text{\AA}} - \log_{10} M_{\star}$ relation of quiescent galaxies in our sample (see also dashed line in Fig. 5) is well expressed by:

$$\log_{10} SFR_{2800\text{\AA}}^Q = 0.75 \log_{10} M_{\star} - 8.00. \quad (14)$$

- iii) We assumed that the border between quiescent and star-forming galaxies is also of the form $SFR_{2800\text{\AA}} \propto M_{\star}^{0.75}$. Under this assumption, the plane $\log_{10} SFR_{2800\text{\AA}}$ versus $\log_{10} M_{\star}$ can be rotated by Eq. 14 easily, as

$$\log_{10} SFR_{2800\text{\AA}}^{\text{rot}} = \log_{10} SFR_{2800\text{\AA}} - \log_{10} SFR_{2800\text{\AA}}^Q. \quad (15)$$

In this case, the distribution of $\log_{10} SFR_{2800\text{\AA}}^{\text{rot}}$ for the different redshift bins can be fitted by Gaussian functions (see Appendix C), where the typical uncertainties for $SFR_{2800\text{\AA}}$ are in average 0.16 dex for the most local bin and $\sim 50\%$ larger (~ 0.23 dex) at $0.9 \leq z \leq 1.1$. Again, we take advantage of the MLE methodology presented in Appendix C

for both removing the uncertainty effects on the distributions of $\log_{10} SFR_{2800\text{\AA}}^{\text{rot}}$ and retrieving the redshift dependence of the distribution shape. We established the maximum value of quiescent galaxies (defined by $SFR_{2800\text{\AA}}$) as the upper 3σ limit of the distribution of values derived from the MLE. By Eq. 15 and the 3σ limits of the distributions derived by the MLE, the limiting value between populations (solid line in Fig. 5) is expressed as follows:

$$\log_{10} SFR_{2800\text{\AA}}^{\text{lim}} = 0.75(\log_{10} M_{\star} - 10) - 0.18(z - 0.1) + 0.11. \quad (16)$$

There are 828 DSF galaxies (number defined from the results retrieved using BC03 SSP models) that were removed from the quiescent sample (complete in stellar mass and defined by the dust corrected UVJ -diagram in Sect. 5) between redshifts $0.3 \leq z \leq 1.1$. Their $SFR_{2800\text{\AA}}$ measurements were confronted with Eq. 16 for determining whether they present proper values of star-forming galaxies or not. Around $\sim 90\%$ of the 828 DSF galaxies have $SFR_{2800\text{\AA}}$ above Eq. 16, and consequently, their SFR values are in the range of star-forming galaxies. Indeed, when we take the SFR uncertainties into account, the fraction increases up to $\sim 97\%$, that is, almost the totality of DSF galaxies, with intrinsic blue colours that were removed from the sample of this work, exhibit SFRs in the range of values of star-forming galaxies for a 1σ uncertainty level. Moreover, we found out that $\sim 98.2\%$ of quiescent galaxies (defined by colours in Sect. 5) have SFR below Eq. 16, which increases up to $\sim 99.8\%$ at 1σ uncertainty level. The same conclusions are obtained when EMILES SSP models are used.

These results additionally supports the MUFFIT predictions about DSF and the necessity of removing these galaxies, which comprise $\sim 10\%$ of the sample, when a UVJ -selection is performed without removing the dust effects on colours. Notice that $SFR_{2800\text{\AA}}$ are also based on SED-fitting predictions carried out by MUFFIT because it is necessary to estimate the luminosity at $\sim 2800\text{\AA}$ removing their dust effects, but it differs respect the selection process developed in Sect. 5 which is based on a colour criterion and not on a luminosity-based SFR tracer.

4.2. Star formation rates and dust emission at $24\mu\text{m}$

The dust emission at $24\mu\text{m}$ is an additional tracer to confirm the predictions of MUFFIT and the above Sect. 4.1. Furthermore, the SFRs predicted from $24\mu\text{m}$ are fully separated from the SED-fitting results provided by MUFFIT and ALHAMBRA data.

The ALHAMBRA field number four, ALHAMBRA-4 in the following, is specially adequate for the purpose of this section. The main feature of ALHAMBRA-4 is that partly overlaps with the COSMOS field, and consequently with S-COSMOS (Sanders et al. 2007). As part of the *Spitzer* Legacy Program, S-COSMOS is a deep infrared survey imaged with the *Spitzer* Space Telescope that covers the entire COSMOS field (2 deg^2) with the IRAC and MIPS cameras. As starting infrared catalogue, we chose the S-COSMOS MIPS $24\mu\text{m}$ Photometry Catalogue October 2008⁸, $\sim 90\%$ ($\sim 75\%$) complete above a $24\mu\text{m}$ flux of $S_{24\mu\text{m}} \sim 80\mu\text{Jy}$ ($S_{24\mu\text{m}} \sim 60\mu\text{Jy}$) where the FWHM of the MIPS $24\mu\text{m}$ PSF is $\sim 6''$ (Le Floc'h et al. 2009). After cross-correlating the $24\mu\text{m}$ MIPS catalogue with all the galaxies in ALHAMBRA-4, we found a total of 1261 common galaxies at $0.2 \leq z \leq 1.2$, both quiescent and star-forming.

⁸ <http://irsa.ipac.caltech.edu/data/COSMOS/>

In brief (for further details, see López-Comazzi 2015), the model of Dale & Helou (2002) is performed in order to obtain the k corrected fluxes $S_{24\mu\text{m}}^{z=0}$ and rest-frame luminosities $L_{24\mu\text{m}}^{z=0}$ making use of the photo- z constraints provided by MUFFIT for these galaxies. In Dale & Helou (2002), the model SED for the ISM is built from combinations of different dust masses heated by a radiation field, with a contribution α for each component. For obtaining $L_{24\mu\text{m}}^{z=0}$, we assumed the α range $1.0 \leq \alpha \leq 2.5$ ($\alpha = 1.0$ is the typical value for active galaxies, whereas for the passive ones is $\alpha = 2.5$). Finally, to convert rest-frame luminosities $L_{24\mu\text{m}}^{z=0}$ into SFRs, we used the relation provided by Calzetti et al. (2007) and expressed as:

$$SFR_{24\mu\text{m}} = 1.31 \cdot 10^{-38} \times L_{24\mu\text{m}}^{z=0}{}^{0.885}. \quad (17)$$

Amongst the 1261 galaxies with MIPS measurements at $24 \mu\text{m}$, there are 58 DSF. Using Eq. 16, we are able to determine whether these 58 galaxies also present SFRs in the order of star-forming galaxies or not. We found out that 51 of 58 galaxies (i. e. the $88 \pm 12 \%$) present SFR values using Eq. 17 larger than the lower limit established by Eq. 16. Consequently, the SFR of these galaxies is more representative of star-forming galaxies than quiescent, which strongly favours that MUFFIT is pointing out that these galaxies are actually reddened by dust.

5. Stellar populations of quiescent galaxies within stellar mass- and UVJ colour-colour diagrams

The empirical bimodality of galaxies in the stellar mass- and colour-colour diagrams is directly related to their stellar population properties (e. g. Bower et al. 1992; Gallazzi et al. 2006; Whitaker et al. 2010). This can be interpreted as a hint to explore whether within the quiescent sequence similar stellar population properties are constrained to lie on certain colour ranges. Indeed, colour predictions from models predict this fact, although there are also degeneracies and some stellar population properties are not observed in real galaxies. In this work, we are in a privileged position because we are able to estimate the extinction, and thus, to discern the main stellar-population parameters that lead to the distribution of colours.

In Sect. 5.1, we explore the distribution of the stellar population parameters of quiescent galaxies within the UVJ diagrams (both corrected and non-corrected for extinction). On the other hand, Sect. 5.2 presents the distribution of the same parameters (age, metallicity, extinction, and sSFR) but in the stellar mass-colour diagram. In both cases, instead of plotting the individual measurements, which include uncertainties, we carried out a bidimensional and locally weighted regression method (LOESS, Cleveland 1988; Cleveland & Devlin 1979). The LOESS method allows us to model the trends of our quiescent sample and minimize the uncertainty effects on the diagram planes through a regression method. Specifically, we used the LOESS implementation for Python language⁹ (Cappellari et al. 2013), where the regularization factor is set to $f = 0.6$ and a local linear approximation is assumed (this method gave satisfactory results in previous work, such as Cappellari et al. 2013; McDermid et al. 2015). The uncertainties in stellar mass, extinction, age, metallicity, and sSFR of individual galaxies were also taken into account during the regression process.

5.1. Stellar population analysis within the intrinsic UVJ diagram

In Figs. 6 and 7, we present the distribution of stellar population parameters for quiescent galaxies on the rest-frame UVJ -diagram (non dust-corrected and intrinsic colours respectively) for BC03 SSP models. To guide the eye, we also plot the typical selection of quiescent galaxies (dotted black line in Fig. 7, see Eq. 1 in this work and Moresco et al. 2013). Interestingly, the only selection criterion $(m_{F365} - m_{F551})_{\text{int}} \geq 1.5$ (dashed black line in Fig. 6) provides a quiescent sample whose observed colour ranges are well delimited by Eq. 1 (see Fig. 7). In our sample of quiescent galaxies, we only find a 1 % of galaxies with $m_{F365} - m_{F551}$ and $m_{F551} - J$ colours out of the box delimited by Eq. 1.

Below, we dissect the UVJ -distribution of stellar population parameters, which constitutes the main result of this section:

- From the first rows of Figs. 6 and 7, fewer massive quiescent galaxies tend to populate the bluest parts of the UVJ -diagram, whereas at increasing red colours $(m_{F365} - m_{F551})_{\text{int}}$ and $(m_{F551} - J)_{\text{int}}$ quiescent galaxies continuously present larger stellar masses. The most massive galaxies are also the reddest ones and they are concentrated in the upper part of the UVJ -diagram at decreasing redshift ($(m_{F365} - m_{F551})_{\text{int}} \sim 2.0$). Nevertheless, most massive galaxies are scattered in a larger $(m_{F365} - m_{F551})_{\text{int}}$ range when we explore the highest redshift panels ($1.5 \leq (m_{F365} - m_{F551})_{\text{int}} \leq 2.0$), which has been extensively observed in the last years (e. g. Bower et al. 1992; Kauffmann et al. 2003; Gallazzi et al. 2005; Baldry et al. 2006; Peng et al. 2010). Notice that each panel comprises different stellar mass ranges, as indicated in the upper labels and according to Fig. 3, hence the less massive galaxies are only present in the local redshift bins.
- The whole sample shows an expected low dust content (96 % of galaxies present $A_V \leq 0.6$), where the more obscured quiescent galaxies lie on the bluer $(m_{F365} - m_{F551})_{\text{int}}$ and $(m_{F551} - J)_{\text{int}}$ intrinsic colour regions of the diagram (see Fig. 6). On the other hand, if dust effects on the colours are not corrected (observational rest-frame colours, Fig. 7), dusty galaxies populate the red parts of the diagram. As a sanity check, the colour changes owing to a dust reddening case with $A_V = 0.5$ and $R_V = 3.1$ and the extinction law of Fitzpatrick (1999) are $\Delta(m_{F365} - m_{F551}) \sim 0.28$ and $\Delta(m_{F551} - J) \sim 0.29$ (illustrated in Figs. 6 and 7), showing the good agreement between the colour changes predicted by an extinction law and the direction of the distribution of increasing extinction values retrieved at any redshift. This also remarks that the extinction values provided by MUFFIT are properly decoupled and not significantly affected by degeneracies with the rest of stellar-population parameters: age and metallicity. Otherwise, the extinction distribution in the UVJ -diagram would be randomly distributed or it would show another colour dependencies.
- Regarding ages (third row in Figs. 6 and 7), older quiescent galaxies in the sample are concentrated in the upper part of the UVJ -diagram, and they therefore tend to populate the intrinsic redder colours $(m_{F365} - m_{F551})_{\text{int}}$. Likewise young quiescent galaxies lie on the bluest colours in concordance with the less massive systems in the sample. From Fig. 6, we find evidences that the variety of ages presented by quiescent galaxies is linked with the scatter of $(m_{F365} - m_{F551})_{\text{int}}$ partly, but not fully linked to this colour. In the rest-frame UVJ -diagram, we also find a non-negligible dependence of the age with $(m_{F551} - J)_{\text{int}}$, although milder

⁹ <http://www-astro.physics.ox.ac.uk/~mxc/software/>

than the other intrinsic colour. Consequently, our results match with previous findings (e. g. Whitaker et al. 2010) in which the $(m_{F365} - m_{F551})_{\text{int}}$ colour is scattered by the ages in the quiescent population. This is not surprising because the $(m_{F365} - m_{F551})_{\text{int}}$ colour ranges the 4 000 Å-break that is sensitive to age (e. g. Bruzual A. 1983; Balogh et al. 1999), even though this is also degenerated with the metallicity (Worthey et al. 1994; Peletier 2013). On the contrary, the observed UVJ -diagram (instead of using the dust-free colours, see Fig. 7) shows that the observed colour $m_{F365} - m_{F551}$ is not driven by the age. In fact, in some panels of Fig. 7, the trends of age with $m_{F365} - m_{F551}$ are not so clear as in the intrinsic ones, or they look inverted. Thereby, extinction is also playing an important role in this aspect masking and blurring the relation between $(m_{F365} - m_{F551})_{\text{int}}$ and age.

- Exploring the metallicity distribution in the UVJ -diagram, see fourth row in Fig. 6, we find out that there is a tight correlation between metallicity and the intrinsic $(m_{F551} - J)_{\text{int}}$ colour. There is a clear trend in which larger metallicity contents ($[M/H]_{\text{M}} > 0.1$ dex) present redder $(m_{F551} - J)_{\text{int}} > 1.1$ colours. Hence the most metal rich quiescent galaxies lie on the right-hand side of the UVJ -diagram and this trend remains at least up to redshift $z \sim 1$. For a fixed $(m_{F551} - J)_{\text{int}}$ colour, the influence of the metal content on the $(m_{F365} - m_{F551})_{\text{int}}$ is almost negligible in a wide range of the colour $(m_{F551} - J)_{\text{int}}$, but it is not null. Whilst the age distribution is distorted by extinction, the metallicity trend with the colour $m_{F551} - J$ is still prominent (last row in Fig. 7). The main extinction effect over metallicity distribution is that at the high redshift panels (or the most massive galaxies, $\log_{10} M_{\star} > 10.8$ dex), the metallicity exhibits a more remarkable dependence with the $m_{F365} - m_{F551}$ colour respect to its intrinsic counterpart (see Fig. 6) and it is substantially less affected than the age.
- As the rest of stellar population properties explored in this work, lower and higher sSFR of quiescent galaxies populate different colour ranges in dust-corrected UVJ diagrams (see last row in Fig. 6). Our results point out that the lowest sSFR lie on the upper parts of this diagram, independently of the stellar mass and redshift. This is not surprising because at increasing stellar mass, quiescent galaxies exhibit lower sSFR and they are also redder. In fact, the correlation between sSFR and the intrinsic colour $(m_{F365} - m_{F551})_{\text{int}}$ is remarkable. Furthermore, there is also a correlation with $(m_{F551} - J)_{\text{int}}$, although milder. Notice that sSFR were retrieved from the luminosity at 2 800 Å (Eq. 13), but we find evidences to propose the intrinsic color $(m_{F365} - m_{F551})_{\text{int}}$ as an alternative sSFR tracer, at least for quiescent galaxies. Nevertheless, this tracer should be treated carefully. When there is not any star formation, Eq. 13 provides non-null SFR, because there is a non null continuum at 2 800 Å. Although these values can be treated as upper sSFR limits. In Fig. 7, we find out that the correlation between $(m_{F365} - m_{F551})_{\text{int}}$ and sSFR is not so clear than with its intrinsic colour. However, certain range colours present predominantly lower sSFR. The lowest sSFR values lie on the upper parts of classic UVJ diagrams (non-dust corrected), whereas the highest ones present bluer colours. This fact matches with the distribution of stellar mass in these diagrams (see first row in Fig. 7), which is not surprising. As above, extinctions displace galaxies within these diagrams, which allows that dust-obscured quiescent galaxies with higher sSFR also lie on the upper parts of UVJ diagrams.

Although it is well known that the use of different stellar population models yields different quantitative results, we find that a great qualitative agreement between all the predictions retrieved using BC03 and EMILES SSP models. Thereby, the same conclusions in this section can be extrapolated when EMILES SSP models (both BaSTI and Padova00 isochrones) are used, see more details in Figs. D.3, D.4, D.10, and D.11 (Appendix D). As we mention above, this is a qualitative analysis since different column panels encompass different stellar mass ranges. A further analysis of the distribution of stellar population parameters in colour diagrams and the influence of the mass is presented in the section below.

5.2. Stellar populations in the dust corrected stellar mass-colour diagram

A straightforward analysis of the distribution of stellar population properties of quiescent galaxies in the stellar mass-colour diagram (both corrected and non-corrected for reddening) can also shed interesting results, as well as to complement and make easier the interpretation of the analysis faced in Sect. 5.1. We illustrate the stellar population parameters of the quiescent galaxies selected by $(m_{F365} - m_{F551})_{\text{int}} \geq 1.5$ in Figs. 8 and 9. We detail the main features of the distribution of stellar population parameters below, which were equally obtained for the three SSP model sets used in this work (BC03, EMILES+BaSTI, and EMILES+Padova00; see also Figs. D.5, D.6, D.12 and D.13 in Appendix D.):

- It is clear from Fig. 8 that the quiescent galaxies exhibiting the larger extinctions are those that also present the bluest intrinsic colours. It is interesting that there is a clear correlation of extinction with the intrinsic colour $(m_{F365} - m_{F551})_{\text{int}}$, but also with the stellar mass of the galaxy since $z \sim 1$. At fixed intrinsic colour $(m_{F365} - m_{F551})_{\text{int}}$, the more massive the quiescent galaxy, the larger the reddening by dust. Whilst there exists this correlation, discrepancies between extinction values are not very remarkable, as extinctions are typically low in the quiescent population. There are not strong evidences to confirm whether more massive galaxies are most dust-reddened or not. When we explore the same diagram but without correcting colours for extinction, Fig. 9, the reddest galaxies are those with the largest dust content (for $A_V \gtrsim 0.4$, $m_{F365} - m_{F551} \gtrsim 2$). In the same sense, there is a correlation of the extinction with both the stellar mass and the $m_{F365} - m_{F551}$ (non-dust corrected). Thus, at fixed colour $m_{F365} - m_{F551}$, more massive galaxies are less dust-reddened than the less massive ones. As in Sect. 5.1, this is in good agreement with the predictions from an extinction law (see black arrows in Fig. 9).
- In the second row of Fig. 8, we find the correlation between age and stellar mass. The most massive quiescent galaxies are also the oldest and the intrinsically reddest ones. This is in agreement with the "downsizing scenario" (Cowie et al. 1996), in which the more massive galaxies were formed in earlier epochs of the Universe respect their less massive counterparts. These very evolved galaxies also present very low extinctions. When studying the distribution of age in the stellar mass-colour diagram without correcting colours for dust, Fig. 9, the dependence between $m_{F365} - m_{F551}$ and age is softly blurred. Although the most massive and reddest ($m_{F365} - m_{F551} \geq 1.8$) are also the oldest ones.
- In Fig. 8, we observe that the stellar mass-metallicity relation is also present, reinforcing the reliability of the stel-

lar population properties retrieved by MUFFIT using ALHAMBRA photometry of galaxies. The more massive the galaxy, the more metal rich is. This correlation is usually referred as the stellar mass-metallicity relation (MZR), which has been studied previously (Trager et al. 2000; Tremonti et al. 2004; Gallazzi et al. 2005; Panter et al. 2008; González Delgado et al. 2014). When we focus in the plane without the dust correction, third row in Fig. 9, equal-metallicity values correlate with $m_{F365} - m_{F551}$, but also with stellar mass. Therefore, metallicity values populate well defined regions of stellar mass-colour diagrams.

- The sSFR values of quiescent galaxies also present well defined loci in the MCDE, see last row in Fig. 8. At increasing stellar mass, lower sSFR values are retrieved. It is interesting that the intrinsic colour $(m_{F365} - m_{F551})_{\text{int}}$ can be interpreted as an alternative sSFR tracer. However, to constrain the sSFR of quiescent galaxies using $m_{F365} - m_{F551}$, it is necessary to include the stellar mass (see Fig. 9). As in previous stellar population properties, the extinction is an important parameter that dilutes the correlations and trends unveiled in this work.

In this paper, we mainly focus on the distribution of stellar population parameters of quiescent galaxies in the stellar mass- and UVJ colour-colour diagrams. A detailed analysis of the stellar populations of quiescent galaxies and its dependence with stellar mass, it is beyond of the scope of this work.

6. Discussion

6.1. New insights into the green valley

Dust corrections play an important role in understanding how quiescent galaxies are distributed on the UVJ diagram as a function of their parameters: stellar mass, age, metallicity, and extinction. One of the most important results regarding the study of this diagram is that the green valley is largely populated by dusty star-forming galaxies ($\sim 65\%$), and that when the effects of reddening are corrected for in an intrinsic UVJ diagram, the population of galaxies in the "real" green valley is much lower than observed. This implies that the transition of galaxies from the blue cloud to the red sequence, and hence the related mechanisms for quenching, seems to be much more efficient and faster than previously considered.

Any successful mechanisms proposed for shutting down the star formation should account for a less populated green valley and a shorter transition timescale. For instance, the common presence of AGNs in galaxies with intermediate host-galaxy colours at $z \lesssim 1$ (Nandra et al. 2007; Bundy et al. 2008; Georgakakis et al. 2008; Silverman et al. 2008; Hickox et al. 2009; Schawinski et al. 2009) was interpreted as an evidence for AGNs heating up the gas in the host-galaxy (Silk & Rees 1998; Di Matteo et al. 2008) and shutting down the star formation rapidly (Bower et al. 2006; Croton et al. 2006; Faber et al. 2007; Schawinski et al. 2007). In the light of the results in this work, AGN feedback should be more efficient than previously expected as a quenching mechanism.

In fact, previous studies (Bell et al. 2005; Cowie & Barger 2008; Brammer et al. 2009; Cardamone et al. 2010) also supported that the population of galaxies in the green valley has bluer intrinsic colours and is largely dominated by dust-reddened galaxies. Based on the results by Cardamone et al. (2010), $\sim 75\%$ of galaxies in the green valley have intrinsic blue colours in good agreement with this work ($\sim 65\%$). In the same work,

after a dust correction of the $U - V$ colour, most of the galaxies hosting an AGN belong to the red sequence, $(U - V)_{\text{int}} \gtrsim 1.5$, or the blue cloud, $(U - V)_{\text{int}} \lesssim 0.8$, with a poor presence of AGNs at intermediate colours, favouring again the idea of either a faster or less frequent quenching mechanism due to AGNs.

6.2. The lower $U - V$ colour limit of UVJ -like diagrams

Even though the rest-frame UVJ diagram has been extensively used for the selection of quiescent galaxies, the lower limit in colour $U - V$ is still uncertain or fixed arbitrarily. In fact, some authors propose different definitions in the colour limits to minimize the impact of DSF (see e. g. Moresco et al. 2013). In addition, UVJ diagrams are only defined by a couple of colours, in which parameters such as stellar mass are not directly accounted for. The detailed analysis of the distribution of stellar population properties in colour-colour diagrams is key to unveil the likely bias that can introduce different colour selections.

Our results in Sect. 5 point out that low mass quiescent galaxies lie on the lower limits of the box classically defined for selecting the quiescent population. Therefore, this kind of colour-colour diagrams should be built accordingly with the specific features of each photometric survey. Taking advantage of the MCDE, see Fig. 10, we can state that the less massive quiescent galaxies can present $U - V$ colours as blue as the ones of massive star-forming galaxies (for EMILES, see Figs. D.7 and D.14 in Appendix D). In fact, this criteria change with redshift, as the intrinsic colours of galaxies also vary with cosmic time (see Eqs. 6–8). This fact is clearly illustrated in Fig. 10 at $0.1 \leq z < 0.3$, in where a bluer colour limit of $(m_{F365} - m_{F551})_{\text{int}} < 1.5$ is necessary to not bias the sample in the low mass regime. However, this limit must be set in accordance with the stellar mass to avoid the inclusion of massive star forming galaxies in the quiescent sample.

In this work, we obtain that the quiescent sample from ALHAMBRA (complete in magnitude down to $m_{F814} = 23$) defined via the dust-corrected UVJ colour-colour diagram and the MCDE is equivalent in the stellar mass range for which the quiescent sample is complete in stellar mass (see details in Fig. 10). For stellar masses below completeness, the only criteria $(m_{F365} - m_{F551})_{\text{int}} > 1.5$ is not enough to select quiescent galaxies. Although dust corrections exhibit a clear bimodality (see also Fig. 1), at $(m_{F365} - m_{F551})_{\text{int}} \sim 1.5$ there is not a well-defined border limiting both populations in UVJ diagrams. This is because these galaxies present similar colours, even after correcting colours for dust-reddening, and the key to split both populations is the inclusion of stellar mass. This would favour the use of the MCDE respect the dust corrected UVJ diagrams. Again, notice that is remarkable that in our case both methods are equivalent to built a quiescent sample complete in stellar mass and luminosity (down to $m_{F814} = 23$, see Fig. 10).

For deeper surveys, $I > 23$ mag, the selection bias can be even larger if these issues are not taken into account. Less massive quiescent galaxies will be detected, and therefore the $U - V$ lower colour limit should be bluer to not bias them. On the other hand, deeper surveys allow us to explore larger redshift ranges and the use of a unique definition like $(m_{F365} - m_{F551})_{\text{int}} > 1.5$ is not adequate strictly, as galaxy colours evolve with cosmic time. In a general case and taken the explored dust-corrected diagrams in this work into account, a pure non-biased selection of quiescent galaxies via colour diagrams should include dust corrections of the involved colours and galaxy stellar masses. Indeed, this discussion can be extended to the classical UVJ -diagrams, in which the colour correction for extinction is not included.

7. Summary and conclusions

Using the dataset provided by the ALHAMBRA multi-filter photometric survey and our optimised SED-fitting tool MUFFIT (extensively detailed in Díaz-García et al. 2015) with both BC03 and EMILES SSP models, we explore the stellar content of quiescent galaxies since $z = 1.1$, corresponding to the last 8 Gyr (60 % of the age of the Universe).

The selection of the quiescent sample is carefully carried out in order to minimize as much as possible the number of contaminants, mainly faint stars and dusty star-forming galaxies. In brief, we improve the colour-colour *UVJ* diagram taking the extinction estimations provided by MUFFIT into account for generating a dust-corrected *UVJ* diagram, which minimizes the contamination of dusty star-forming galaxies. We also explore the use of stellar mass-colour diagrams corrected for extinction (MCDE), an alternative diagram for the selection of quiescent galaxies and confronting results with the *UVJ*. Moreover, we carry out a one-by-one visual inspection to remove those sources whose photometry can be compromised (e. g. bad CCD regions or bad photometric apertures) and spurious detections. Using the stellar version of MUFFIT, we remove the faint stars of the ALHAMBRA catalogue with magnitudes ranging $22.5 \leq m_{F814W} \leq 23$. After comparing with the morphological classification of COSMOS for a common sample of sources, the contamination due to faint stars is reduced from 24 % to 4 %. Finally, we estimate the stellar mass completeness of our sample of quiescent galaxies in ALHAMBRA applying a novel method for defining an analytic function for the stellar mass completeness that yields a final sample of $\sim 8\,500$ galaxies at $0.1 \leq z \leq 1.1$ with a photo- z accuracy of $\sigma_{\text{NMAD}} = 0.006$.

We also develop a reliable methodology to take advantage of our SED-fitting results (based on a mixture of two SSPs) and make predictions of SFR and sSFR. The exploration of the distribution of SFR and sSFR values in the stellar mass plane reveals a bimodality, where the main sequence of galaxies (star-forming galaxies) populate the upper SFR and sSFR values. In addition, the more massive quiescent galaxies exhibit larger SFRs than their lower mass counterparts. However, the most efficient process of star formation in the quiescent population reside in the low mass systems, whereas the massive ones present the lowest sSFR of the quiescent population. We compare our SFR predictions based on the UV luminosity at around $2\,800\text{ Å}$ with an independent SFR tracer based on the $24\text{ }\mu\text{m}$ luminosity or dust emission, getting a satisfactory agreement that supports that the DSF of the sample were removed properly.

From the dust-corrected *UVJ*-diagram, we find out a number of striking results:

- A significant part of the galaxies that reside in the green valley are actually obscured star-forming galaxies ($\sim 65\%$). These reveal intrinsic colours $(m_{F365} - m_{F551})_{\text{int}}$ proper of the star-forming population, although their great dust content redden their colours. This also implies that the green valley is less populated than expected and the transition of galaxies from the blue cloud to the red sequence, and hence the related mechanisms for quenching, seems to be much more efficient and faster than previously considered.
- Down to $m_{F814W} = 23$, the histogram of the $(m_{F365} - m_{F551})_{\text{int}}$ colour exhibits a local minimum at ~ 1.45 that can be imposed as the bluest colour limit to fairly select the quiescent sample, which remains roughly constant since $z \leq 1.1$.
- Red galaxies that belong to the star-forming sample after the dust correction (intrinsic $m_{F365} - m_{F551} < 1.5$) are typically concentrated close to the edges of *UVJ* diagrams (e. g.

Williams et al. 2009; Moresco et al. 2013), supporting the reliability of the extinction values provided by MUFFIT.

- Quiescent galaxies selected through a classical *UVJ* diagram (not corrected from dust effects) are typically contaminated by a $\sim 20\%$ fraction of dusty star forming galaxies. Our results clearly establish that this contamination is less severe for massive galaxies ($\log_{10} M_{\star} \geq 11$, 2–8 % from $z \sim 0.1$ to $z \sim 1.1$) than for the least massive ones (40 %, for $9.2 \leq \log_{10} M_{\star} \leq 9.6$ at $0.1 \leq z \leq 0.3$).

The analysis of the distribution of stellar population parameters of quiescent galaxies on a dust-corrected *UVJ*-diagram and MCDE reveals that there exists a close correlation between the position of each galaxy in these diagrams and its age, metallicity, extinction, and stellar mass. We conclude that:

- The more massive quiescent galaxies lie on the redder parts of the *UVJ*-diagram at larger cosmic times. At higher redshifts, $z \sim 1$, massive quiescent galaxies present a larger spread of $(m_{F365} - m_{F551})_{\text{int}}$ colours ($1.5 \leq (m_{F365} - m_{F551})_{\text{int}} \leq 2.0$) than at $z \sim 0.2$, where they lie on the upper and redder parts of the *UVJ*-diagram $(m_{F365} - m_{F551})_{\text{int}} \sim 2.0$.
- The whole quiescent sample shows an expected low dust content (96 % of galaxies present $A_V \leq 0.6$), where quiescent galaxies with bluer intrinsic colours, $(m_{F365} - m_{F551})_{\text{int}} \lesssim 1.7$ and $(m_{F551} - J)_{\text{int}} \lesssim 1.2$, are also the galaxies with larger extinction values ($A_V \gtrsim 0.4$). There is no clear evidence suggesting a clear trend between stellar mass and dust extinction.
- We find out a correlation between the colour $(m_{F365} - m_{F551})_{\text{int}}$ and the age of quiescent galaxies. The older ages present the redder $(m_{F365} - m_{F551})_{\text{int}}$ colours, populating the upper parts of the *UVJ*-diagram $((m_{F365} - m_{F551})_{\text{int}} > 1.8)$. On the other hand, the younger quiescent galaxies present the bluer colour of the diagram. Although there is a correlation with the $(m_{F365} - m_{F551})_{\text{int}}$ colour, age is also dependent of the $(m_{F551} - J)_{\text{int}}$ colour. The older quiescent galaxies lie on the high-mass end of the MCDE and these ones are the reddest ones (both $(m_{F365} - m_{F551})_{\text{int}}$ and $m_{F365} - m_{F551}$). The less massive quiescent galaxies are younger and bluer in good agreement with the "downsizing" scenario.
- The metallicity distribution in the *UVJ*-diagram is tightly correlated with the colour $(m_{F551} - J)_{\text{int}}$ and weakly with $(m_{F365} - m_{F551})_{\text{int}}$. The most metal rich quiescent galaxies ($[M/H]_{\text{M}} > 0.1$ dex) also present the reddest colours $(m_{F551} - J)_{\text{int}} > 1.1$. The more massive, the more metal-rich the quiescent galaxy is (MZR) as revealed by the MCDE. Metallicity values lie on very well defined positions in both *UVJ* and MCDE diagrams.
- For quiescent galaxies, very low sSFR ($\log_{10} \text{sSFR}_{2800\text{Å}} \sim -11$) lie on the upper parts of rest-frame and dust corrected *UVJ*-diagrams $((m_{F365} - m_{F551})_{\text{int}} \gtrsim 1.8)$; while values of $\log_{10} \text{sSFR}_{2800\text{Å}} \sim -10.5$ are at $(m_{F365} - m_{F551})_{\text{int}} \lesssim 1.6$. A correlation between sSFR and the intrinsic colour $(m_{F365} - m_{F551})_{\text{int}}$ is found, which may be used as a sSFR tracer at least for quiescent galaxies. Actually, this tracer should be treated carefully, as the sSFR are computed via a SFR tracer which is linked to the $2\,800\text{ Å}$ luminosity, i. e. even when star formation processes are not present, the continuum yields a non-null sSFR value.

From both stellar mass- and *UVJ* colour-colour diagrams, we conclude that dust corrections play an important role in understanding how quiescent galaxies distribute inside these diagram as a function of their parameters: mass, age, metallicity,

extinction, and sSFR. Without dust corrections, quiescent galaxies with large dust contents are in the upper parts of the *UVJ*-diagram and CMD as predicted by extinction laws. The correlation between age and the colour ($m_{F365} - m_{F551}$) is weaker than with $(m_{F365} - m_{F551})_{\text{int}}$, whereas metallicity still correlates with $(m_{F551} - J)$ but also with $(m_{F365} - m_{F551})$.

After exploring the MCDE and the rest-frame *UVJ* colour-colour diagram, we note that to perform a pure non-biased selection of quiescent galaxies from these diagrams, we should include dust corrections of the involved colours and also the galaxy stellar mass.

Acknowledgements. L. A. D. G. acknowledges support from the “Caja Rural de Teruel” for partly developing this research. A. J. C. is a Ramón y Cajal Fellow of the Spanish Ministry of Science and Innovation. This work has been partly supported by the “Programa Nacional de Astronomía y Astrofísica” of the Spanish Ministry of Economy and Competitiveness (MINECO) under grant AYA2012-30789, as well as by FEDER funds and the Government of Aragón, through the Research Group E103. L. A. D. G. also thanks the support of I. F. for offering the opportunity to develop part of this research at the Mullard Space Science Laboratory (MSSL). We also acknowledge support from the Spanish Ministry for Economy and Competitiveness and FEDER funds through grants AYA2010-15081, AYA2010-15169, AYA2010-22111-C03-01, AYA2010-22111-C03-02, AYA2011-29517-C03-01, AYA2012-39620, AYA2013-40611-P, AYA2013-42227-P, AYA2013-43188-P, AYA2013-48623-C2-1, AYA2013-48623-C2-2, ESP2013-48274, AYA2014-58861-C3-1, Generalitat Valenciana projects Prometeo 2009/064 and PROMETEOII/2014/060, Junta de Andalucía grants TIC114, JA2828, P10-FQM-6444, and Generalitat de Catalunya project SGR-1398. Throughout this research, we made use of the Matplotlib package (Hunter 2007), a 2D graphics package used for Python which is designed for interactive scripting and quality image generation. This paper is dedicated to M. A. L. C., a light in the darkness supporting and encouraging me to continue until the end of my Ph. D. and this work.

References

- Aparicio Villegas, T., Alfaro, E. J., Cabrera-Caño, J., et al. 2010, *AJ*, 139, 1242
- Arnouts, S., Le Floch, E., Chevillard, J., et al. 2013, *A&A*, 558, A67
- Arzner, K., Güdel, M., Briggs, K., et al. 2007, *A&A*, 468, 501
- Baldry, I. K., Balogh, M. L., Bower, R. G., et al. 2006, *MNRAS*, 373, 469
- Baldry, I. K., Glazebrook, K., Brinkmann, J., et al. 2004, *ApJ*, 600, 681
- Balogh, M. L., Morris, S. L., Yee, H. K. C., Carlberg, R. G., & Ellingson, E. 1999, *ApJ*, 527, 54
- Bell, E. F., Papovich, C., Wolf, C., et al. 2005, *ApJ*, 625, 23
- Bell, E. F., Wolf, C., Meisenheimer, K., et al. 2004, *ApJ*, 608, 752
- Belli, S., Newman, A. B., & Ellis, R. S. 2015, *ApJ*, 799, 206
- Benítez, N. 2000, *ApJ*, 536, 571
- Bower, R. G., Benson, A. J., Malbon, R., et al. 2006, *MNRAS*, 370, 645
- Bower, R. G., Lucey, J. R., & Ellis, R. S. 1992, *MNRAS*, 254, 601
- Brammer, G. B., van Dokkum, P. G., & Coppi, P. 2008, *ApJ*, 686, 1503
- Brammer, G. B., Whitaker, K. E., van Dokkum, P. G., et al. 2009, *ApJ*, 706, L173
- Brown, M. J. I., Dey, A., Jannuzi, B. T., et al. 2007, *ApJ*, 654, 858
- Bruzual, G. & Charlot, S. 2003, *MNRAS*, 344, 1000
- Bruzual A., G. 1983, *ApJ*, 273, 105
- Bundy, K., Georgakakis, A., Nandra, K., et al. 2008, *ApJ*, 681, 931
- Calzetti, D., Kennicutt, R. C., Engelbracht, C. W., et al. 2007, *ApJ*, 666, 870
- Capak, P., Aussel, H., Ajiki, M., et al. 2007, *ApJS*, 172, 99
- Cappellari, M., McDermid, R. M., Alatalo, K., et al. 2013, *MNRAS*, 432, 1862
- Cardamone, C. N., Urry, C. M., Schawinski, K., et al. 2010, *ApJ*, 721, L38
- Chabrier, G. 2003, *PASP*, 115, 763
- Choi, J., Conroy, C., Moustakas, J., et al. 2014, *ApJ*, 792, 95
- Cid Fernandes, R., Mateus, A., Sodré, L., Stasińska, G., & Gomes, J. M. 2005, *MNRAS*, 358, 363
- Cleveland, W. & Devlin, S. 1979, *Journal of the American Statistical Association*, 83, 596
- Cleveland, W. S. 1988, *Journal of the American Statistical Association*, 74, 829
- Coe, D., Benítez, N., Sánchez, S. F., et al. 2006, *AJ*, 132, 926
- Coelho, P., Barbuy, B., Meléndez, J., Schiavon, R. P., & Castilho, B. V. 2005, *A&A*, 443, 735
- Conroy, C. 2013, *ARA&A*, 51, 393
- Cooper, M. C., Aird, J. A., Coil, A. L., et al. 2011, *ApJS*, 193, 14
- Cowie, L. L. & Barger, A. J. 2008, *ApJ*, 686, 72
- Cowie, L. L., Songaila, A., Hu, E. M., & Cohen, J. G. 1996, *AJ*, 112, 839
- Cristóbal-Hornillos, D., Aguerri, J. A. L., Moles, M., et al. 2009, *ApJ*, 696, 1554
- Croton, D. J., Springel, V., White, S. D. M., et al. 2006, *MNRAS*, 365, 11
- Daddi, E., Cimatti, A., Renzini, A., et al. 2004, *ApJ*, 617, 746
- Daddi, E., Dickinson, M., Morrison, G., et al. 2007, *ApJ*, 670, 156
- Dale, D. A. & Helou, G. 2002, *ApJ*, 576, 159
- Davis, M., Guhathakurta, P., Konidaris, N. P., et al. 2007, *ApJ*, 660, L1
- Di Matteo, T., Colberg, J., Springel, V., Hernquist, L., & Sijacki, D. 2008, *ApJ*, 676, 33
- Díaz-García, L. A., Cenarro, A. J., López-Sanjuan, C., et al. 2015, *A&A*, 582, A14
- Domínguez Sánchez, H., Pérez-González, P. G., Esquej, P., et al. 2016, *MNRAS*, 457, 3743
- Domínguez Sánchez, H., Pozzi, F., Gruppioni, C., et al. 2011, *MNRAS*, 417, 900
- Elbaz, D., Daddi, E., Le Borgne, D., et al. 2007, *A&A*, 468, 33
- Faber, S. M., Willmer, C. N. A., Wolf, C., et al. 2007, *ApJ*, 665, 265
- Fang, J. J., Faber, S. M., Koo, D. C., et al. 2017, *ArXiv e-prints* [arXiv:1710.05489]
- Fitzpatrick, E. L. 1999, *PASP*, 111, 63
- Fontana, A., Pozzetti, L., Donnarumma, I., et al. 2004, *A&A*, 424, 23
- Foreman-Mackey, D., Hogg, D. W., Lang, D., & Goodman, J. 2013, *PASP*, 125, 306
- Fritz, A., Scodreggio, M., Ilbert, O., et al. 2014, *A&A*, 563, A92
- Fumagalli, M., Labbé, I., Patel, S. G., et al. 2014, *ApJ*, 796, 35
- Gallazzi, A., Charlot, S., Brinchmann, J., & White, S. D. M. 2006, *MNRAS*, 370, 1106
- Gallazzi, A., Charlot, S., Brinchmann, J., White, S. D. M., & Tremonti, C. A. 2005, *MNRAS*, 362, 41
- Georgakakis, A., Nandra, K., Yan, R., et al. 2008, *MNRAS*, 385, 2049
- Girardi, L., Bressan, A., Bertelli, G., & Chiosi, C. 2000, *A&AS*, 141, 371
- González Delgado, R. M., Cid Fernandes, R., García-Benito, R., et al. 2014, *ApJ*, 791, L16
- Hickox, R. C., Jones, C., Forman, W. R., et al. 2009, *ApJ*, 696, 891
- Hunter, J. D. 2007, *Computing in Science & Engineering*, 9, 90
- Ilbert, O., McCracken, H. J., Le Fèvre, O., et al. 2013, *A&A*, 556, A55
- Ilbert, O., Salvato, M., Le Floch, E., et al. 2010, *ApJ*, 709, 644
- Jimenez, R., Bernardi, M., Haiman, Z., Panter, B., & Heavens, A. F. 2007, *ApJ*, 669, 947
- Kauffmann, G., Heckman, T. M., White, S. D. M., et al. 2003, *MNRAS*, 341, 54
- Koleva, M. & Vazdekis, A. 2012, *A&A*, 538, A143
- Le Floch, E., Aussel, H., Ilbert, O., et al. 2009, *ApJ*, 703, 222
- Leauthaud, A., Massey, R., Kneib, J.-P., et al. 2007, *ApJS*, 172, 219
- Lilly, S. J., Le Brun, V., Maier, C., et al. 2009, *ApJS*, 184, 218
- López-Comazzi, A. 2015, Master’s thesis
- López-Sanjuan, C., Cenarro, A. J., Hernández-Monteagudo, C., et al. 2015, *A&A*, 582, A16
- López-Sanjuan, C., Cenarro, A. J., Hernández-Monteagudo, C., et al. 2014, *A&A*, 564, A127
- López-Sanjuan, C., García-Dabó, C. E., & Balcells, M. 2008, *PASP*, 120, 571
- Madau, P., Pozzetti, L., & Dickinson, M. 1998, *ApJ*, 498, 106
- Makarov, D., Makarova, L., Rizzi, L., et al. 2006, *AJ*, 132, 2729
- Martín, N. S., Marchesini, D., Brammer, G. B., et al. 2016, *ApJ*, 827, L25
- McDermid, R. M., Alatalo, K., Blitz, L., et al. 2015, *MNRAS*, 448, 3484
- Moles, M., Benítez, N., Aguerri, J. A. L., et al. 2008, *AJ*, 136, 1325
- Molino, A., Benítez, N., Moles, M., et al. 2014, *MNRAS*, 441, 2891
- Moresco, M., Pozzetti, L., Cimatti, A., et al. 2013, *A&A*, 558, A61
- Moustakas, J., Coil, A. L., Aird, J., et al. 2013, *ApJ*, 767, 50
- Nandra, K., Georgakakis, A., Willmer, C. N. A., et al. 2007, *ApJ*, 660, L11
- Naylor, T. & Jeffries, R. D. 2006, *MNRAS*, 373, 1251
- Noeske, K. G., Weiner, B. J., Faber, S. M., et al. 2007, *ApJ*, 660, L43
- Oke, J. B. & Gunn, J. E. 1983, *ApJ*, 266, 713
- Pacifici, C., Kassin, S. A., Weiner, B. J., et al. 2016, *ApJ*, 832, 79
- Panther, B., Jimenez, R., Heavens, A. F., & Charlot, S. 2008, *MNRAS*, 391, 1117
- Peletier, R. F. 2013, XXIII Canary islands winter school of astrophysics. Stellar Populations, 353
- Peng, Y., Maiolino, R., & Cochrane, R. 2015, *Nature*, 521, 192
- Peng, Y.-j., Lilly, S. J., Kovač, K., et al. 2010, *ApJ*, 721, 193
- Pérez-González, P. G., Rieke, G. H., Villar, V., et al. 2008, *ApJ*, 675, 234
- Pietrinferni, A., Cassisi, S., Salaris, M., & Castelli, F. 2004, *ApJ*, 612, 168
- Pozzetti, L., Bolzonella, M., Zucca, E., et al. 2010, *A&A*, 523, A13
- Ricciardelli, E., Vazdekis, A., Cenarro, A. J., & Falcón-Barroso, J. 2012, *MNRAS*, 424, 172
- Röck, B., Vazdekis, A., Peletier, R. F., Knapen, J. H., & Falcón-Barroso, J. 2015, *MNRAS*, 449, 2853
- Salpeter, E. E. 1955, *ApJ*, 121, 161
- Sandage, A., Tammann, G. A., & Yahil, A. 1979, *ApJ*, 232, 352
- Sanders, D. B., Salvato, M., Aussel, H., et al. 2007, *ApJS*, 172, 86
- Schawinski, K., Thomas, D., Sarzi, M., et al. 2007, *MNRAS*, 382, 1415
- Schawinski, K., Virani, S., Simmons, B., et al. 2009, *ApJ*, 692, L19
- Schechter, P. 1976, *ApJ*, 203, 297
- Silk, J. & Rees, M. J. 1998, *A&A*, 331, L1
- Silverman, J. D., Mainieri, V., Lehmer, B. D., et al. 2008, *ApJ*, 675, 1025
- Trager, S. C., Faber, S. M., Worthey, G., & González, J. J. 2000, *AJ*, 120, 165

- Tremonti, C. A., Heckman, T. M., Kauffmann, G., et al. 2004, *ApJ*, 613, 898
 Vazdekis, A., Cenarro, A. J., Gorgas, J., Cardiel, N., & Peletier, R. F. 2003, *MNRAS*, 340, 1317
 Vazdekis, A., Koleva, M., Ricciardelli, E., Röck, B., & Falcón-Barroso, J. 2016, *MNRAS*, 463, 3409
 Vazdekis, A., Ricciardelli, E., Cenarro, A. J., et al. 2012, *MNRAS*, 424, 157
 Vazdekis, A., Sánchez-Blázquez, P., Falcón-Barroso, J., et al. 2010, *MNRAS*, 404, 1639
 Vergani, D., Scodeggio, M., Pozzetti, L., et al. 2008, *A&A*, 487, 89
 Whitaker, K. E., van Dokkum, P. G., Brammer, G., & Franx, M. 2012, *ApJ*, 754, L29
 Whitaker, K. E., van Dokkum, P. G., Brammer, G., et al. 2010, *ApJ*, 719, 1715
 Williams, R. J., Quadri, R. F., Franx, M., van Dokkum, P., & Labbé, I. 2009, *ApJ*, 691, 1879
 Worthey, G., Faber, S. M., Gonzalez, J. J., & Burstein, D. 1994, *ApJS*, 94, 687
 Wyder, T. K., Martin, D. C., Schiminovich, D., et al. 2007, *ApJS*, 173, 293
 Yano, M., Kriek, M., van der Wel, A., & Whitaker, K. E. 2016, *ApJ*, 817, L21

-
- ¹ Centro de Estudios de Física del Cosmos de Aragón (CEFCA), Plaza San Juan 1, Floor 2, E-44001 Teruel, Spain
 e-mail: diaz@cefca.es
² Mullard Space Science Laboratory, University College London, Holmbury St Mary, Dorking, Surrey RH5 6NT, United Kingdom
³ IAA-CSIC, Glorieta de la Astronomía s/n, 18008 Granada, Spain
⁴ Instituto de Astrofísica de Canarias, Vía Láctea s/n, 38200 La Laguna, Tenerife, Spain
⁵ Instituto de Física de Cantabria (CSIC-UC), E-39005 Santander, Spain
⁶ Unidad Asociada Observatorio Astronómico (IFCA-UV), E-46980, Paterna, Spain
⁷ Observatório Nacional-MCT, Rua José Cristino, 77. CEP 20921-400, Rio de Janeiro-RJ, Brazil
⁸ Department of Theoretical Physics, University of the Basque Country UPV/EHU, 48080 Bilbao, Spain
⁹ IKERBASQUE, Basque Foundation for Science, Bilbao, Spain
¹⁰ Departamento de Física Atómica, Molecular y Nuclear, Facultad de Física, Universidad de Sevilla, 41012 Sevilla, Spain
¹¹ Institut de Ciències de l'Espai (IEEC-CSIC), Facultat de Ciències, Campus UAB, 08193 Bellaterra, Spain
¹² Departamento de Astrofísica, Facultad de Física, Universidad de La Laguna, 38206 La Laguna, Spain
¹³ Instituto de Astrofísica, Universidad Católica de Chile, Av. Vicuña Mackenna 4860, 782-0436 Macul, Santiago, Chile
¹⁴ Centro de Astro-Ingeniería, Universidad Católica de Chile, Av. Vicuña Mackenna 4860, 782-0436 Macul, Santiago, Chile
¹⁵ Instituto de Astronomía, Geofísica e Ciências Atmosféricas, Universidade de São Paulo, São Paulo, Brazil
¹⁶ Observatori Astronòmic, Universitat de València, C/ Catedràtic José Beltrán 2, E-46980, Paterna, Spain
¹⁷ Departament d'Astronomia i Astrofísica, Universitat de València, E-46100, Burjassot, Spain

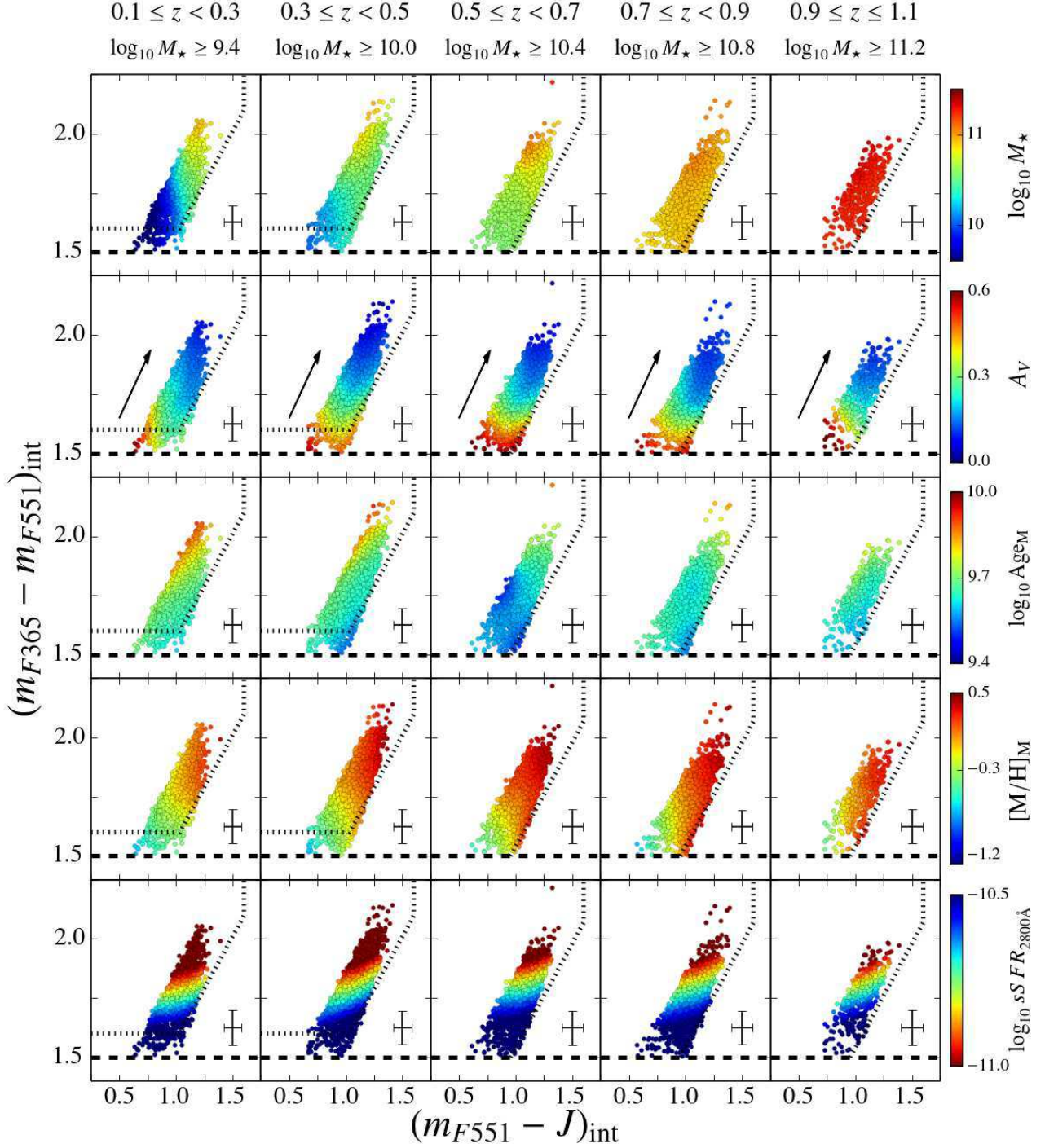


Fig. 6. The stellar-population parameters in the rest-frame UVJ -diagram. At different redshift bins, we present the intrinsic colours $(m_{F551} - J)_{\text{int}}$ (X-axis) and $(m_{F365} - m_{F551})_{\text{int}}$ (Y-axis) after correcting for extinction for the mass complete sample of quiescent galaxies (see stellar mass completeness on the top). The different stellar-population parameters are colour coded in function of their values and obtained using BC03 SSP models, see the inset colour bars in each panel. *From top to bottom*, stellar mass, extinction, both mass-weighted age and metallicity, and specific star formation rate. All the parameters were spatially averaged through a LOESS method. Black crosses illustrate the median uncertainties in both $(m_{F551} - J)_{\text{int}}$ and $(m_{F365} - m_{F551})_{\text{int}}$ intrinsic colours. Dashed black line encloses the rest-frame colour ranges assumed for selecting quiescent galaxies in Moresco et al. (2013, see Eq. 1), while dotted line illustrates our colour limit for selecting quiescent galaxies $(m_{F365} - m_{F551})_{\text{int}} > 1.5$. We illustrate the colour variations owing to a reddening of $A_V = 0.5$ (black arrow), assuming the extinction law of Fitzpatrick (1999).

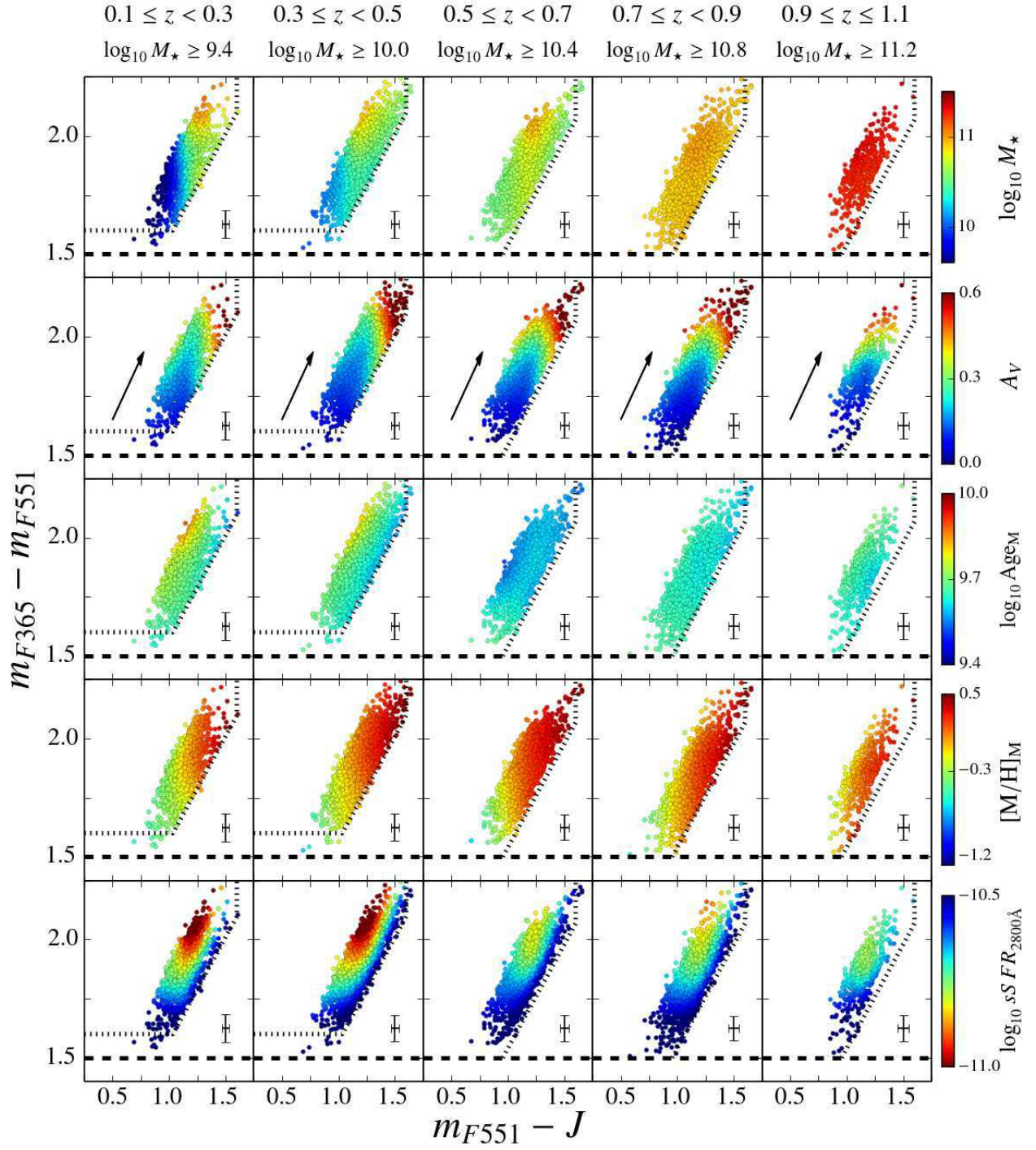


Fig. 7. As Fig. 6, but we plot the rest-frame colours $m_{F551} - J$ (X-axis) and $m_{F365} - m_{F551}$ (Y-axis) instead.

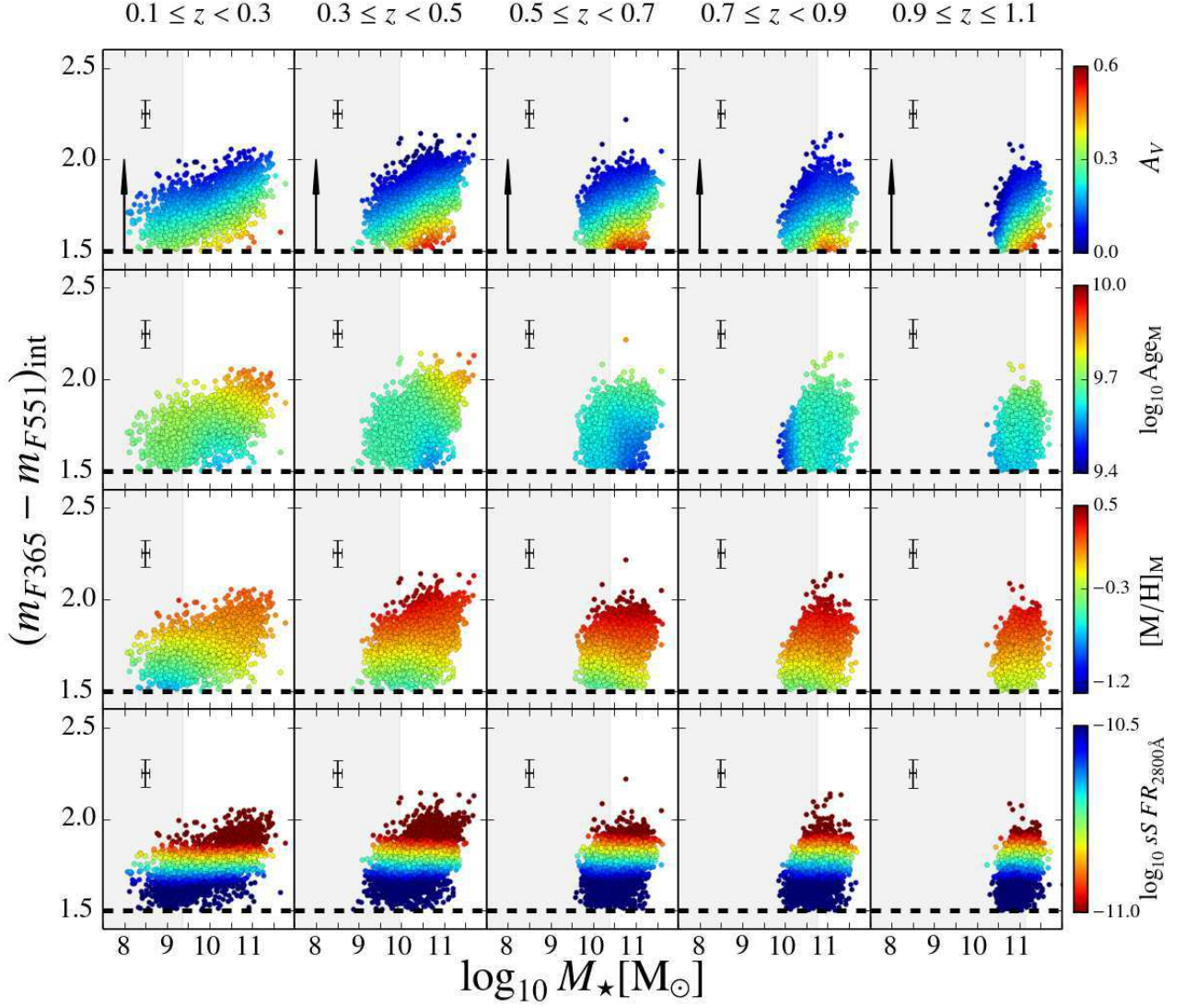


Fig. 8. The stellar-population parameters in the rest-frame stellar mass-colour diagram. At different redshift bins, we present the stellar mass (X-axis) and intrinsic colour $(m_{F365} - m_{F551})_{\text{int}}$ (Y-axis) after correcting for extinction. The different stellar-population parameters are colour coded in function of their values and obtained using BC03 SSP models, see the inset colour bars in each panel. *From top to bottom*, extinction, both mass-weighted age and metallicity, and specific star formation rate. All the parameters were spatially averaged through a LOESS method. Black crosses illustrate the median uncertainties in both stellar mass and $(m_{F365} - m_{F551})_{\text{int}}$ intrinsic colour. Dotted line illustrates the colour limit for selecting quiescent galaxies $(m_{F365} - m_{F551})_{\text{int}} > 1.5$ in the *UVJ* diagram for this work. Shaded regions show the stellar mass range in which our quiescent sample is not complete in stellar mass. We illustrate the colour variations owing to a reddening of $A_V = 0.5$ (black arrow), assuming the extinction law of Fitzpatrick (1999).

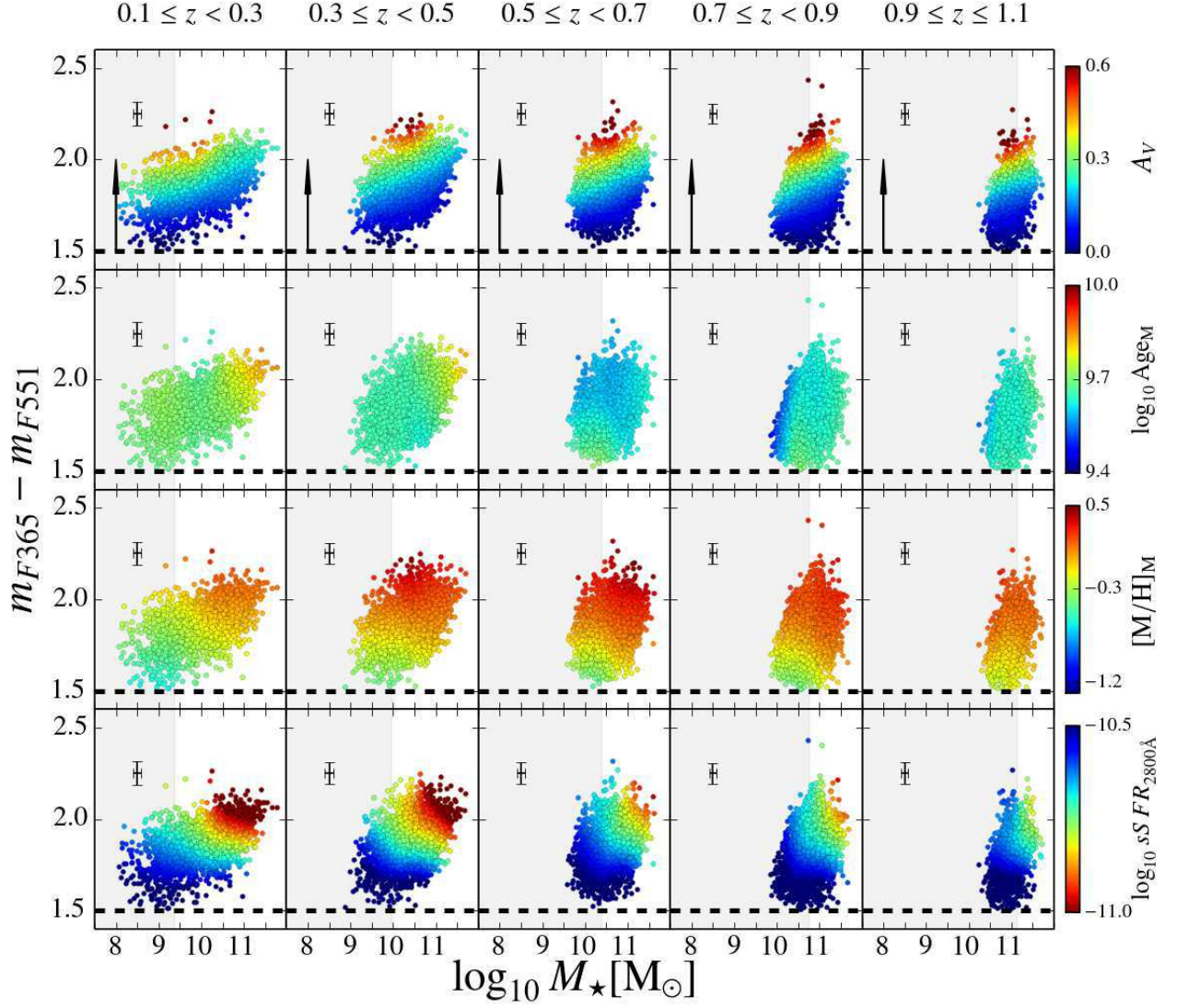


Fig. 9. As Fig. 2, but for the rest-frame colour $m_{F365} - m_{F551}$ (X-axis, non-dust corrected).

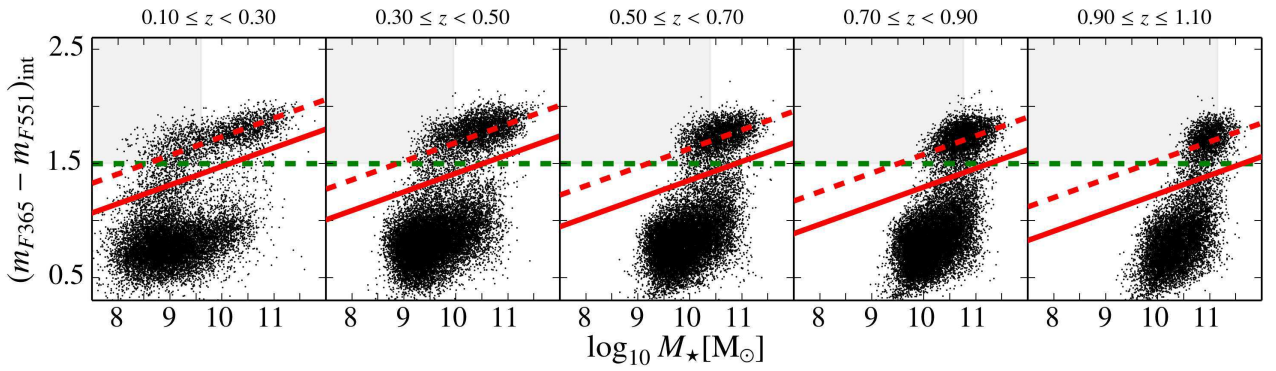


Fig. 10. All the ALHAMBRA galaxies (black dots) in the rest-frame stellar mass-colour diagram corrected for extinction (MCDE) at different redshift bins. Shaded region illustrates the stellar mass range in which our sample of quiescent galaxies is not complete in stellar mass (see Sect. 3.5) at each redshift bin. Dashed green lines show the limiting value $(m_{F365} - m_{F551})_{\text{int}} = 1.5$ used for selecting quiescent galaxies in Sect. 3.1. Dashed red line exhibits the main sequence of quiescent galaxies in the MCDE (see Eq. 2), whereas the solid one the limiting colour values for selecting quiescent galaxies in this diagram (see Eq. 6). The stellar population predictions were obtained through BC03 SSP models.

Appendix A: Detection and removal of faint stars in the quiescent sample

The performance of the MUFFIT module devoted to analysing stars is basically the same than for the galaxy version, excepting that instead of using mixture of SSP models it takes templates of stars to provide stellar parameters (effective temperature, metallicity, surface gravity, chemical composition, and extinction).

We ran the stellar version of MUFFIT with all the sources in the ALHAMBRA catalogue that present an apparent magnitude in the range $22.5 \leq m_{F814W} < 23$, using as input models the stellar library of Coelho et al. (2005) with the main grid of parameters: effective temperatures in steps of 250 K, $3500 \leq T_{\text{eff}} \leq 7000$ K; surfaces gravities with steps of 0.5, $0.0 \leq \log_{10} g \leq 5.0$; metallicities in the range $[\text{Fe}/\text{H}] = -2.5$ to $+0.5$; and chemical compositions $[\alpha/\text{Fe}] = 0.0$ and 0.4 . In addition, we added extinction values ranging $A_V = 0.0$ – 3.1 to the star models taking $R_V = 3.1$ and assuming a Fitzpatrick (1999) extinction law.

After the SED-fitting analysis and thanks to the Monte Carlo process performed by MUFFIT, we obtained two sets of χ^2 values for each source. One set from the SED-fitting treating the source as a galaxy and another one as a star. Therefore, the χ^2 distribution with the lower values (the most likely set of templates, galaxy or star) will discern whether the source is a galaxy or not. Although this method takes advantage of the photometry in all the bands, all the sources show apparent magnitudes in the range $22.5 \leq m_{F814W} < 23$, with a reasonable low signal-to-noise ratio that makes the distinction between distributions more difficult in several cases. To solve this drawback, we carried out a KS test, that allowed us to discern whether both χ^2 distributions are different or not and what is the probability. We assume that a source in the range $22.5 \leq m_{F814W} < 23$ is a star if satisfies that: the median of χ^2 values (from the χ^2 distribution) is lower using star templates than SSP templates, and that the KS-test additionally shows that both distributions of χ^2 values (star and galaxy) are not equivalent at a significance level of 1σ . Under these constraints, we got that in the redshift range $0.1 \leq z \leq 1.1$, there are 439 star candidates in the quiescent sample with $22.5 \leq m_{F814W} < 23$. Taking into account that there are 2284 quiescent galaxies in our sample at the same magnitude and redshift bin before the faint star/galaxy classification, we have removed the $\sim 19 \%$ of the sample at $22.5 \leq m_{F814W} < 23$. After removing all the faint star candidates in this magnitude range, our sample is composed of 13 796 quiescent galaxies.

To check whether the method developed for ALHAMBRA for removing stars in the range $22.5 \leq m_{F814W} < 23$ is reliable or not, we cross matched the ALHAMBRA and COSMOS photometric catalogues (Capak et al. 2007) to built a subset of shared sources in both surveys. Making the most of the ACS camera in COSMOS, we compared the stars or point sources detected in COSMOS and the ones by our method to estimate the degree of accuracy. There are 230 sources in common with our sample of quiescent candidates with apparent magnitudes $22.5 \leq m_{F814W} < 23$, in which we found out 50 star candidates with apparent magnitudes $22.5 \leq m_{F814W} < 23$ using the ALHAMBRA photometry and MUFFIT. From the star/galaxy classification of COSMOS (Leauthaud et al. 2007) in this subsample of 230 sources, we checked that 47 (94 %) of them are classified as point sources in COSMOS. Nevertheless, there are 9 stars that were not detected in the common subset with $22.5 \leq m_{F814W} < 23$ following the COSMOS classification. This points out that there are about a 24 % of faint stars that should be removed. In the case in which we can extrapolate these percentages from the subsample in common with COSMOS to

our sample of quiescent galaxies in ALHAMBRA, we would remove 84 % of faint stars in ALHAMBRA. Furthermore, we would expect a contamination around 4 % of stars in our sample of quiescent galaxies at $22.5 \leq m_{F814W} < 23$; as long as the star/galaxy classification of COSMOS was assumed as the optimal star/galaxy classification.

Figures A.1 and A.2 illustrate two cases in the process of detection and removal of faint stars from the quiescent sample. In Fig. A.1, we exhibit an ALHAMBRA source at $m_{F814W} = 22.8$ that was classified as star with the methodology explained above and in agreement with the stellar classification of COSMOS. From its stamp in COSMOS (top left panel) is easy to see that this source is a point-like candidate, unfortunately in ALHAMBRA (top right), the size of the PSF masks this feature. The middle panel of Fig. A.1 presents a good perspective of the MUFFIT efficiency for removing red and faint stellar sources from the quiescent sample. The statistical support of the Monte Carlo approach, using the proper signal-to-noise ratio of each band, allows us to discern that this source is actually a star with a significance level of $\sim 2.5 \sigma$ (98 %). Regarding the best-fitting stellar model (bottom panel of Fig. A.1), we observe that the optical range is well fitted by both Coelho et al. (2005, red markers) and BC03 (blue markers), but at the bluer and redder parts of the SED (black markers) a stellar model slightly fits better than a mixture of two SSPs. Note that for this case, there are no measurements in the m_{F365W} , m_{F396W} , and H bands owing to they are under their limit magnitudes. In Fig. A.2, we illustrate a red galaxy with $m_{F814W} = 22.7$ that was confirmed as galaxy by MUFFIT. Whilst in the COSMOS stamp this galaxy shows a remarkable and larger projected size, the ALHAMBRA PSF blurs the sources enough as to present a similar projected sizes than the stellar case (see top right panels in Figs. A.1 and A.2). Middle panel in Fig. A.2 shows a dominant set of lower χ^2 values, or best-fitting, of the mixture of two BC03 SSPs respect the stellar ones, which is clearly stated after comparing the galaxy SED with both best-fitting model predictions (bottom panel). Notice that two BC03 SSP models better fit the whole spectral range of ALHAMBRA, fitting simultaneously UV, optical, and NIR; unlike Coelho et al. (2005) models.

The election of a 1σ significance level is a compromise between the percentage of stars that remain in the sample, or contaminants, and the galaxies that were removed mistakenly. Indeed, the significance level for the KS-test can be used as an estimator to remove stars from the sample. If we relaxed the significance level toward lower values, we would be able to detect more faint stars, but we also would remove more fake stars that really are galaxies. Even though this drawback, notice that our SED-fitting analysis at a 1σ significance level made a substantial improvement in the faint end of the quiescent sample, where the contamination of faint stars were initially 24 % and now this is reduced up to 4 %, for which we have removed less than 1 % of galaxies in $22.5 \leq m_{F814W} < 23$ and much less in the total sample.

Appendix B: Stellar mass completeness determination

Our aim is to develop a method for parametrizing the stellar mass completeness of the ALHAMBRA galaxies. This method must be both applicable to the sample of quiescent galaxies in this work and easily calculable for any completeness level, C . Firstly, we explore the possibility of using a Fermi-Dirac like distribution function in order to model the stellar mass completeness in Appendix B.1, as this analytical function was already taken

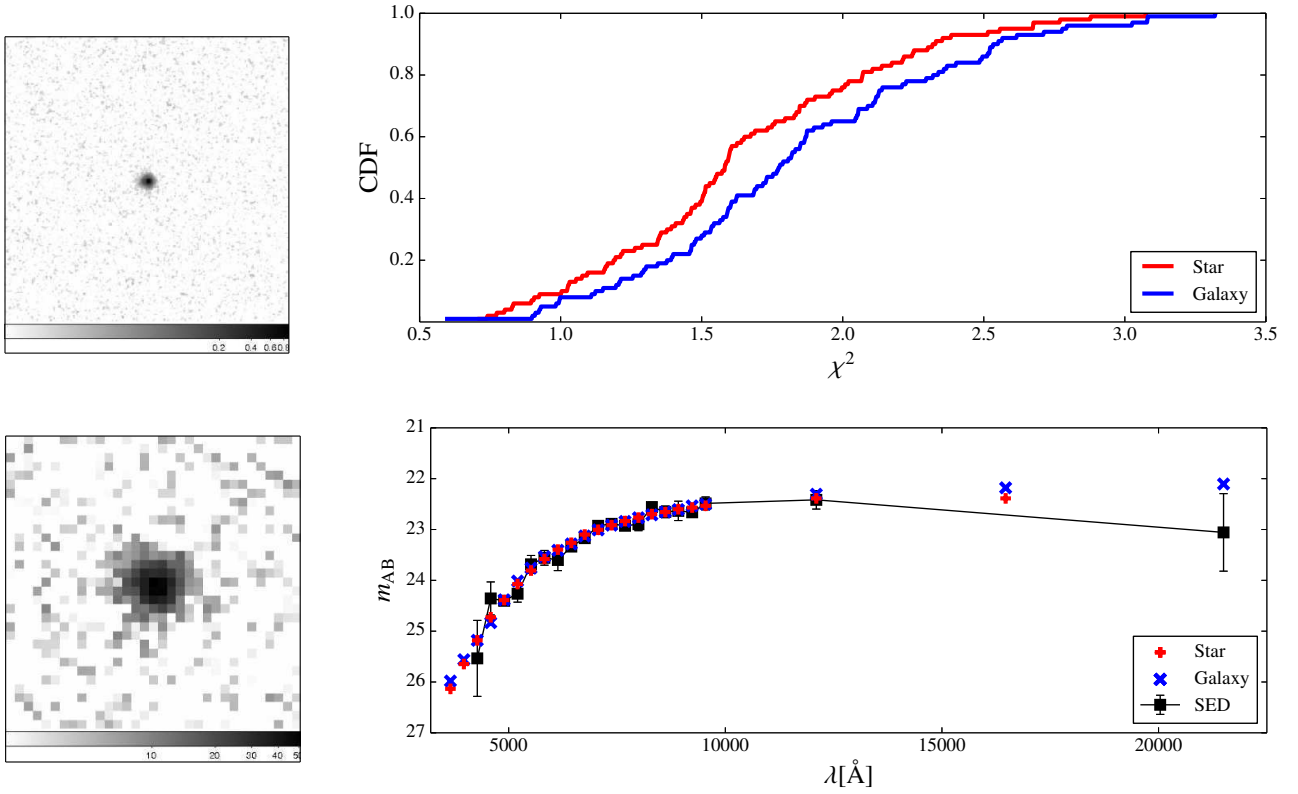


Fig. A.1. Red source identified as faint star and removed from the ALHAMBRA quiescent sample. *Top left and bottom left panels*, stamps of the faint star candidate in COSMOS (ACS camera, pixel scale $0.03''$ pixel $^{-1}$) and ALHAMBRA (LAICA camera, resolution $0.22''$ pixel $^{-1}$) respectively (aperture of $7'' \times 7''$ for both stamps). *Top right panel*, cumulative distribution function (CDF) of the χ^2 distributions obtained during the Monte Carlo process treating the source as an star (red) and as a galaxy (blue). *Bottom right panel*, best-fitting Coelho et al. (2005) model (red) and mixture of two BC03 SSPs (blue) to the photometry of the candidate (black).

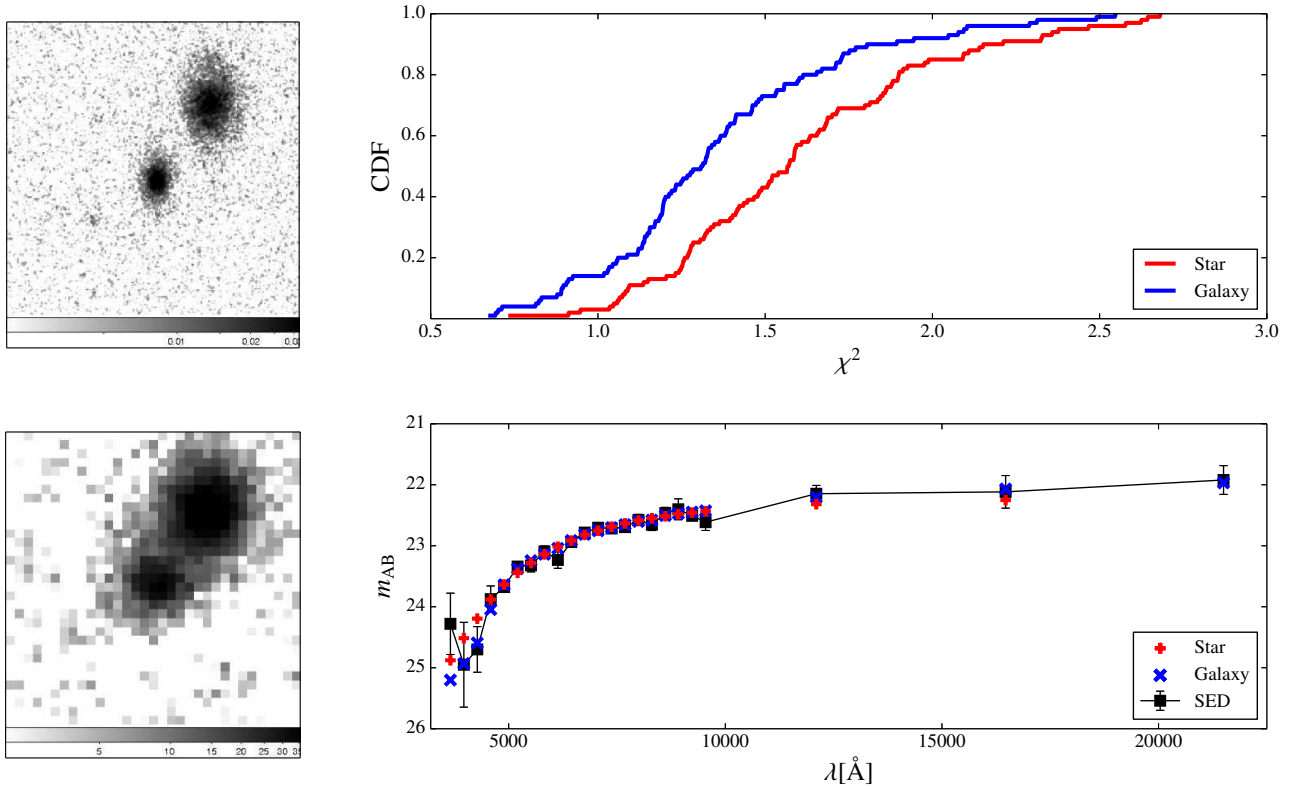


Fig. A.2. As Fig. A.1, but for a galaxy candidate case in the range $22.5 \leq m_{F814W} \leq 23.0$.

in previous works with satisfactory results (e. g. Sandage et al. 1979, although for magnitude completeness). Posteriorly in Appendix B.2, we detail the definitive method taken for this research to determine the stellar mass completeness of the quiescent sample.

Appendix B.1: Parametrization of the stellar mass completeness

The most natural way to estimate the stellar mass completeness of quiescent galaxies in this work (from the ALHAMBRA Gold catalogue) would be made the most of the full ALHAMBRA catalogue because of it is complete up to $m_{F814W} \sim 24.5$ (Molino et al. 2014), unlike the Gold catalogue that only comprises its bright part ($m_{F814W} \leq 23$). We also analysed all the galaxies in this deeper range with MUFFIT, seeking to estimate their stellar masses and rest-frame colours. The latter with the only purpose of extracting all the quiescent galaxies in the luminosity range $23 < m_{F814W} \leq 24$ (i. e. one magnitude deeper than our main sample for this research) following the selection criteria in Sect. 3. At this point, we likely estimated the percentage of galaxies we were missing after comparing the number of quiescent galaxies brighter than $m_{F814W} = 23$ with the total sample of quiescent galaxies down to $m_{F814W} = 24$ at different stellar mass and redshift bins. By this method, we estimated the bias introduced by the apparent magnitude selection ($m_{F814W} \leq 23$) over our quiescent galaxy sample.

Furthermore, our interest resides on parametrising the decay observed through any kind of function, and we tested a Fermi-Dirac distribution function for this aim. A Fermi-Dirac distribution function is formally expressed as

$$f_{FD}(z, M_\star) = \frac{1}{\exp[(M_F(z) - \log_{10} M_\star)/\Delta_F(z)] + 1}, \quad (B.1)$$

where $M_F(z)$ is the stellar mass value (in dex) for which the completeness reaches 50 % ($C = 0.5$) and $\Delta_F(z)$ is related with the decrease rate on the number of galaxies. Note that both $M_F(z)$ and $\Delta_F(z)$ are redshift dependent. To check that the stellar mass completeness introduced by the apparent magnitude selection ($m_{F814W} \leq 23$) can be reproduced by this analytical function, we fitted the bias introduced by the apparent magnitude selection through a χ^2 -test of Eq. B.1 and parameters $5 \leq M_F(z) \leq 14$ and $0.02 \leq \Delta_F(z) < 2$. In Fig. B.1 and for the redshift bin $0.4 \leq z < 0.5$, we show the stellar mass completeness ($m_{F814W} \leq 23$, solid blue line) and the Fermi-Dirac function that best fits it (dashed red line). We therefore confirm that this function fits properly the stellar mass completeness of our sample. The stellar mass value limit for a given completeness level and redshift, $M_C(z)$, can be easily derived from Eq. B.1 as

$$\log_{10} M_C(z) = \Delta_F(z) \ln[(1 - C) - 1] + M_F(z). \quad (B.2)$$

Indeed, these results are a good estimation of the stellar mass completeness itself. Although it also presents a disadvantage or uncertainty, we do not know how much complete in stellar mass is the sample of galaxies at $23 < m_{F814W} \leq 24$, since we can only confirm that it is complete in apparent magnitude but not in stellar mass. This method may be a good approach for magnitudes around $m_{F814W} \sim 23$ and for large stellar mass completeness ($C \gtrsim 0.7$). For magnitudes closer to $m_{F814W} = 24$, the ALHAMBRA sample may also be affected by incompleteness and the reliability of the predictions may be compromised. In Appendix B.2, we present an alternative and more general method, which is indeed the method used for this work.

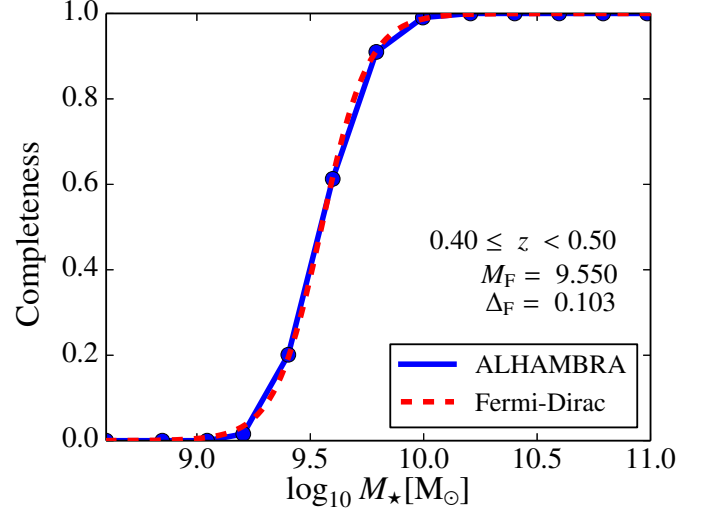


Fig. B.1. Stellar mass completeness of the ALHAMBRA sample of quiescent galaxies complete in flux down to $m_{F814W} \leq 23$. In blue, we illustrate the values recovered by the method explained in Appendix B.1 at the redshift bin $0.4 \leq z < 0.5$. The red dashed line illustrates the Fermi-Dirac like function that best fits our results at this redshift range, along with the parameters (M_F and Δ_F) of the function.

Appendix B.2: Likelihood-maximisation method

We perform a more generic method that suppress the disadvantages noted above taking advantage of stellar mass functions, $\Phi(M)$, from deeper surveys. In particular, we took the stellar mass functions from the COSMOS survey for quiescent galaxies (Ilbert et al. 2010). We aim measuring how the low-mass end of the ALHAMBRA sample differs from much deeper surveys, where these differences are led by the mass incompleteness. In this second method, we followed a process similar to the work of Sandage et al. (1979, STY), that lies in a likelihood maximisation in which we include the completeness term. This likelihood \mathcal{L} encompasses the probability of observing a galaxy accounting for both the selection and observational effects. Formally,

$$\ln \mathcal{L} = \sum_{i=1}^{N_g} \frac{\Phi(M_i) f(M_i)}{\int_{M_{i,\min}}^{M_{i,\max}} \Phi(M') f(M') dM'}, \quad (B.3)$$

where N_g is the number of galaxies in the sub-sample, $f(M_i)$ is the stellar mass completeness (Eq. B.1) for a galaxy with stellar mass M_i at certain redshift, $M_{i,\min}$ and $M_{i,\max}$ are respectively the minimum and maximum stellar mass at the redshift in which the galaxy i th resides, and $\Phi(M)$ is the stellar mass function characterised by the functional form of a Schechter-like function (Schechter 1976) through three parameters (α , M_* , and the normalisation Φ^* ; see Fontana et al. 2004; Pérez-González et al. 2008; Vergani et al. 2008; Ilbert et al. 2010, 2013) expressed as:

$$\Phi(M) dM = \Phi^* \left(\frac{M}{M_*} \right)^\alpha \exp\left(-\frac{M}{M_*}\right) d\left(\frac{M}{M_*}\right). \quad (B.4)$$

Notice that this likelihood must be re-maximised at each redshift bin of interest, but it is not necessary to define stellar mass bins. After fixing both α and M_* to the values obtained in Ilbert et al. (2010), the term Φ^* is not relevant because it is cancelled in Eq. B.3, the maximisation of Eq. B.3 provides us M_F and Δ_F .

Finally, we compare the values M_F and Δ_F obtained in Appendix B.1 with the values from the maximization of Eq. B.3 reaching a good agreement between both predictions. M_F and Δ_F present little discrepancies (< 0.1 dex and < 0.05 dex respectively) after comparing both techniques, where the reference values for the present work those obtained by the likelihood method. In Table 2, the values M_F and Δ_F are shown, as well as the stellar mass limits for different completeness levels for the quiescent galaxies in ALHAMBRA down to $m_{F814W} = 23$. This values were obtained for BC03 SSP models, that is, the same model set used by Ilbert et al. (2010) for the COSMOS survey. We check that the discrepancies between the stellar masses retrieved using EMILES are systematically more massive about 0.15 dex (0.11 dex) for BaSTI (Padova00) isochrones in comparison with those obtained using BC03 SSP models. For EMILES, the completeness is well reproduced when we add this systematic difference (0.15 and 0.11 dex) in M_F without altering Δ_F .

Appendix C: Removing uncertainty effects from distributions of stellar population properties

During the last decades, maximum likelihood estimators (MLE) have been used for varied aims in Astronomy (e. g. Naylor & Jeffries 2006; Makarov et al. 2006; Arzner et al. 2007; López-Sanjuan et al. 2008, 2015). For this work, we performed a MLE to remove uncertainties effects of individual galaxies from distributions of stellar populations properties, that is, a deconvolution to recover the intrinsic distributions of stellar population parameters. In Sects. 3.2 and 4, the distributions of $(m_{F365} - m_{F551})_{\text{int}}^{\text{rot}}$ and $\log_{10} SFR_{2800\text{\AA}}^{\text{rot}}$ values (respectively, Eqs. 5 and 15) supposed a challenge to determine the limiting values for quiescent galaxies, as these distributions are affected by the redshift-dependent uncertainties of individual galaxies.

Our starting point is the MLE method detailed by López-Sanjuan et al. (2014), which was initially developed to disentangle cosmic variance effects. In López-Sanjuan et al. (2014), authors assumed that intrinsic distributions are properly described by Gaussian-like probability distributions in the log-space, i. e. log-normal distributions in the real space. In addition, for uncertainties in the stellar population parameters of individual galaxies, a Gaussian distribution was also assumed. Therefore, uncertainty effects would increase distribution widths with a little impact on the distribution median. Under these assumptions, the likelihood to maximize (for details, see López-Sanjuan et al. 2014) is:

$$\mathcal{L} = -\frac{1}{2} \sum_j \left[\ln \left(p_{e,j}^2 + \sigma_p^{\text{int}2} \right) + \frac{(\mu_p - p_j)^2}{p_{e,j}^2 + \sigma_p^{\text{int}2}} \right], \quad (\text{C.1})$$

where p_j is the stellar population parameter (in this work $(m_{F365} - m_{F551})_{\text{int}}^{\text{rot}}$ or $\log_{10} SFR_{2800\text{\AA}}^{\text{rot}}$) of the j th galaxy in the distribution, $p_{e,j}$ is its 1σ error, μ_p the median of the real or intrinsic distribution (without uncertainty effects), and σ_p^{int} its width or intrinsic dispersion. For the maximization of Eq. C.1, we make the most of the *emcee*¹⁰ algorithm (Foreman-Mackey et al. 2013). This tool is an affine invariant sampling algorithm for a Markov chain Monte Carlo method (MCMC) that can be easily adapted to any function for maximization.

Figure C.1 shows the distribution of $(m_{F365} - m_{F551})_{\text{int}}^{\text{rot}}$ values of quiescent galaxies (for further details, see Sect. 3.2). Notice that Eq. C.1 is defined for Gaussian distributions, and

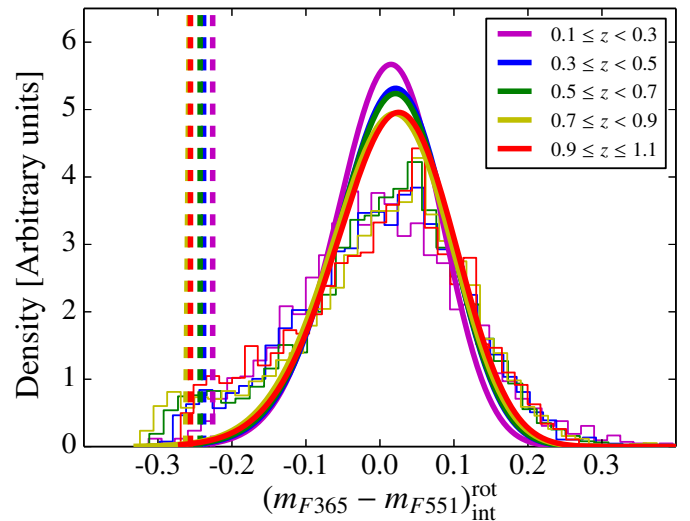


Fig. C.1. Histogram of the $(m_{F365} - m_{F551})_{\text{int}}^{\text{rot}}$ (see Eq. 5) values for the quiescent sample (intrinsic red galaxies) at different redshifts using BC03 SSP models. Solid lines illustrates the MLE best-fitting of the $(m_{F365} - m_{F551})_{\text{int}}^{\text{rot}}$ distributions at their average redshifts. Dashed coloured lines show the upper 3σ limit of the distributions provided by the MLE method.

$(m_{F365} - m_{F551})_{\text{int}}^{\text{rot}}$ is a lognormal-like distribution (see Fig. C.1). Therefore, we maximize Eq. C.1 for the distribution of values in the log-space, i. e. $\ln [1 - (m_{F365} - m_{F551})_{\text{int}}^{\text{rot}}]$ where a shift in the distribution is necessary to avoid negative values. As expected, medians almost remain unaltered after the MLE deconvolution, whereas the intrinsic distributions are narrower than the observed ones (see Fig. C.1). To illustrate, close to 3σ limit there is an overdensity in the number of galaxies, which may be partly interpreted as the transient population of galaxies from the blue cloud to the red sequence (green valley, see Fig. C.1), but also by uncertainties.

The intrinsic distribution of $\log_{10} SFR_{2800\text{\AA}}^{\text{rot}}$ can be fitted by Gaussian functions at any redshift bin properly (see Fig. C.2). Once again, the most remarkable impact of uncertainties is the widening of the distributions. After removing uncertainties and parametrized the distribution, it is straightforward to set the limiting sSFR values of quiescent galaxies. As mentioned above, we set this limit at a 3σ level (see dashed lines in Fig. C.2).

Appendix D: Distribution of stellar population parameters on the UVJ -diagram using EMILES SSP models

Throughout this work, to assess potential systematics from the use of a given population synthesis model, we use different sets of SSP models: BC03 and EMILES. The latter using both the isochrones of BaSTI and Padova00 (details in Sect. 2.1). Despite the little quantitative discrepancies amongst the outcomes obtained for the three sets of model predictions, there is a successful qualitative agreement in the results. Nevertheless, we complement this work including the predictions for EMILES SSP models.

In Figs. D.1–D.7, we illustrate the results for EMILES+BaSTI: the dust corrected UVJ -diagram (see details in Sect. 3.1), the MCDE (Sect. 3.2), the stellar-population parameters of quiescent galaxies in the dust- and non dust-corrected rest-frame UVJ -diagram (Sect. 5.1), the

¹⁰ <http://dan.iel.fm/emcee>

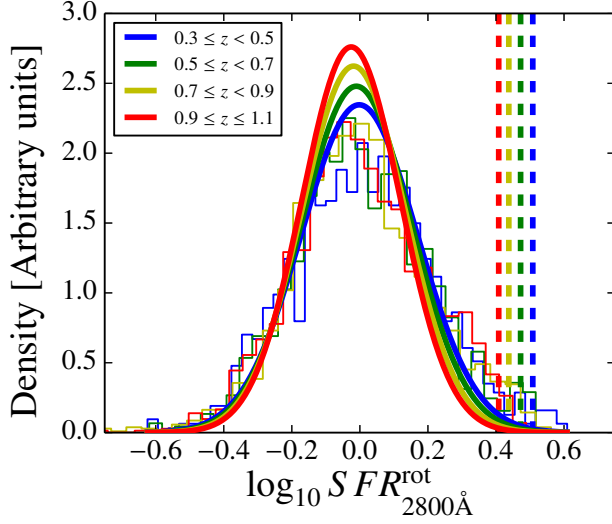


Fig. C.2. Histogram of the $\log_{10} SFR_{2800\text{\AA}}^{\text{rot}}$ (see Eq. 15) values for the quiescent sample defined by their star formation rates $SFR_{2800\text{\AA}}$ (see Eq. 13) at different redshifts using BC03 SSP models. Solid lines illustrates the MLE best-fitting of the $\log_{10} SFR_{2800\text{\AA}}^{\text{rot}}$ distributions at their average redshifts. Dashed coloured lines show the upper 3σ limit of the distributions provided by the MLE method.

stellar-population parameters of quiescent galaxies in the dust- and non dust-corrected stellar mass-colour diagram (Sect. 5.2), and the ALHAMBRA galaxies in the MCDE to set lower colour limits in UVJ -like diagrams (Sect. 6.2). The same plots (same order as above) are shown in Figs. D.8–D.14 for EMILES with Padova00 isochrones.

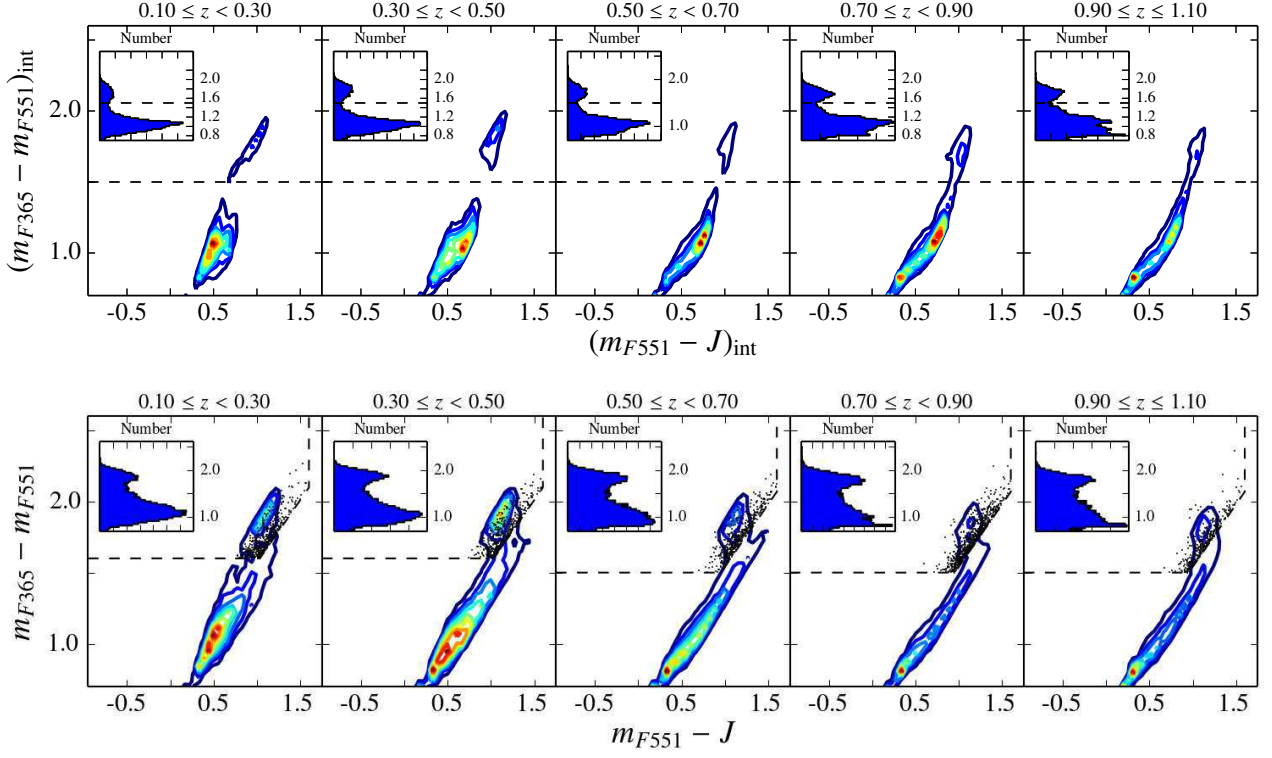


Fig. D.1. *Top panels* illustrate the density surface of rest-frame intrinsic colours $m_{F551} - J$ (X-axis) and $m_{F365} - m_{F551}$ (Y-axis) after correcting for extinction at different redshifts, whereas *bottom panels* are rest-frame colours without removing dust effects, both obtained by EMILES+BaSTI SSP models. Redder (bluer) density-curve colours are related to high (low) densities. *Inner panels*, histograms of the intrinsic (*top*) and observed (*bottom*) rest-frame colour $m_{F365} - m_{F551}$. Dashed lines in *top panels* illustrate our limiting value $(m_{F365} - m_{F551})_{\text{int}} = 1.5$ for quiescent galaxies, and in the *bottom panel* the quiescent UVJ -sample defined by Moresco et al. (2013, Eq. 1). Black dots are galaxies defined as quiescent with the UVJ -criteria of Moresco et al. (2013) that lie in the star-forming region after taking their extinctions into account.

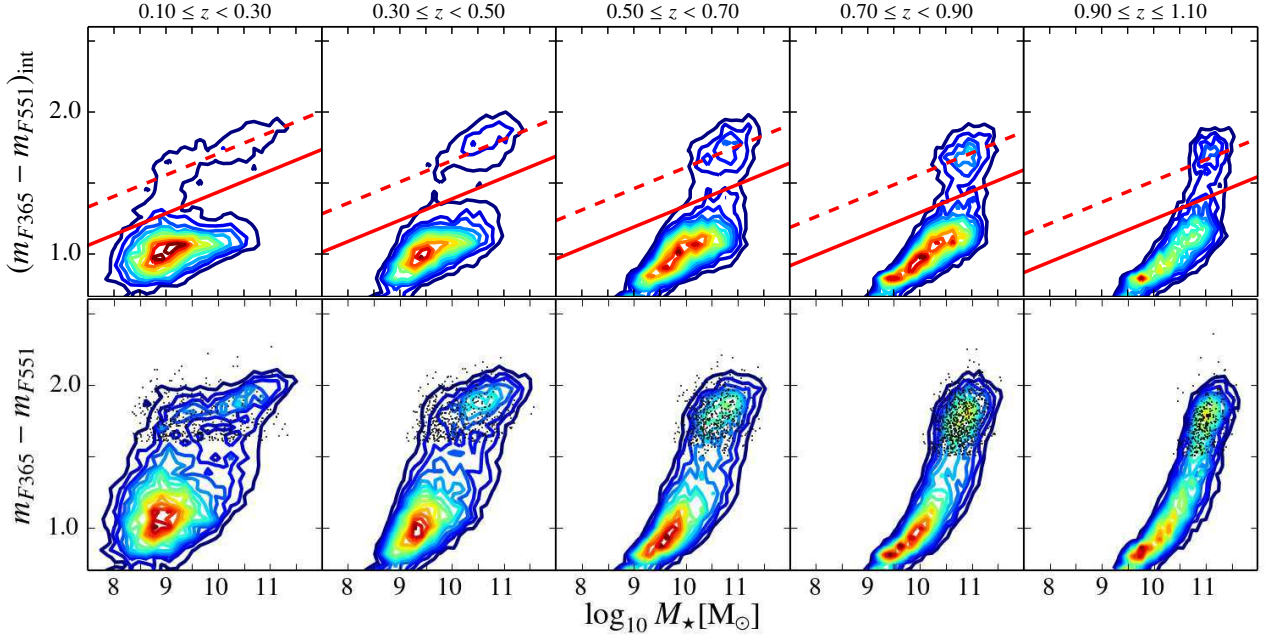


Fig. D.2. *Top panels* illustrate the density surface of stellar mass (X-axis) and the rest-frame intrinsic colour $m_{F365} - m_{F551}$ (Y-axis) after correcting for extinction at different redshifts, whereas *bottom panels* are rest-frame colours without removing dust effects, all obtained by EMILES+BaSTI SSP models. Redder (bluer) density-curve colours are related to high (low) densities. Dashed lines in *top panels* illustrate the limiting value $(m_{F365} - m_{F551})_{\text{int}} = 1.5$ used for selecting quiescent galaxies in Sect. 3.1. Black dots are galaxies defined as quiescent with the UVJ -criteria of Moresco et al. (2013) that lie in the star-forming region after taking their extinctions into account. Dashed and solid red lines show the fit to the quiescent sequence, $(m_{F365} - m_{F551})_{\text{int}}^{\text{Q}}$, and the limiting intrinsic colours, $(m_{F365} - m_{F551})_{\text{int}}^{\text{lim}}$, values of quiescent galaxies respectively (see details in Sect. 3.2).

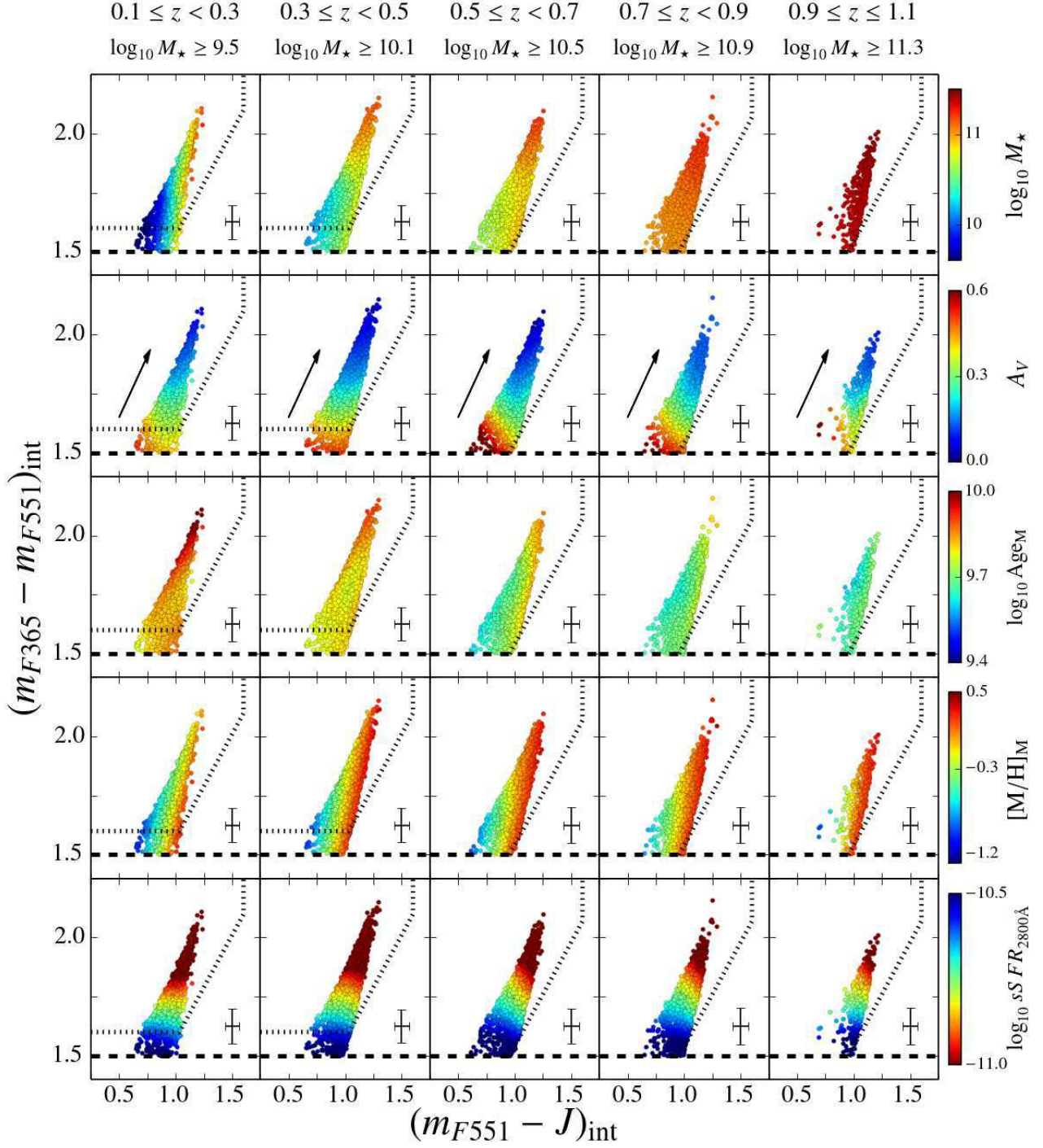


Fig. D.3. The stellar-population parameters in the rest-frame UVJ -diagram. At different redshift bins, we present the intrinsic colours $(m_{F551} - J)_{\text{int}}$ (X -axis) and $(m_{F365} - m_{F551})_{\text{int}}$ (Y -axis) after correcting for extinction for the mass complete sample of quiescent galaxies (see stellar mass completeness on the top). The different stellar-population parameters are colour coded in function of their values and were obtained using EMILES+BaSTI SSP models, see the inset colour bars in each panel. *From top to bottom*, stellar mass, extinction, both mass-weighted age and metallicity, and specific star formation rate. All the parameters were spatially averaged through a LOESS method. Black crosses illustrate the median uncertainties in both $(m_{F551} - J)_{\text{int}}$ and $(m_{F365} - m_{F551})_{\text{int}}$ intrinsic colours. Dashed black line encloses the rest-frame colour ranges assumed for selecting quiescent galaxies in Moresco et al. (2013, see Eq. 1), while dotted line illustrates our colour limit for selecting quiescent galaxies $(m_{F365} - m_{F551})_{\text{int}} > 1.5$. We illustrate the colour variations owing to a reddening of $A_V = 0.5$ (black arrow), assuming the extinction law of Fitzpatrick (1999).

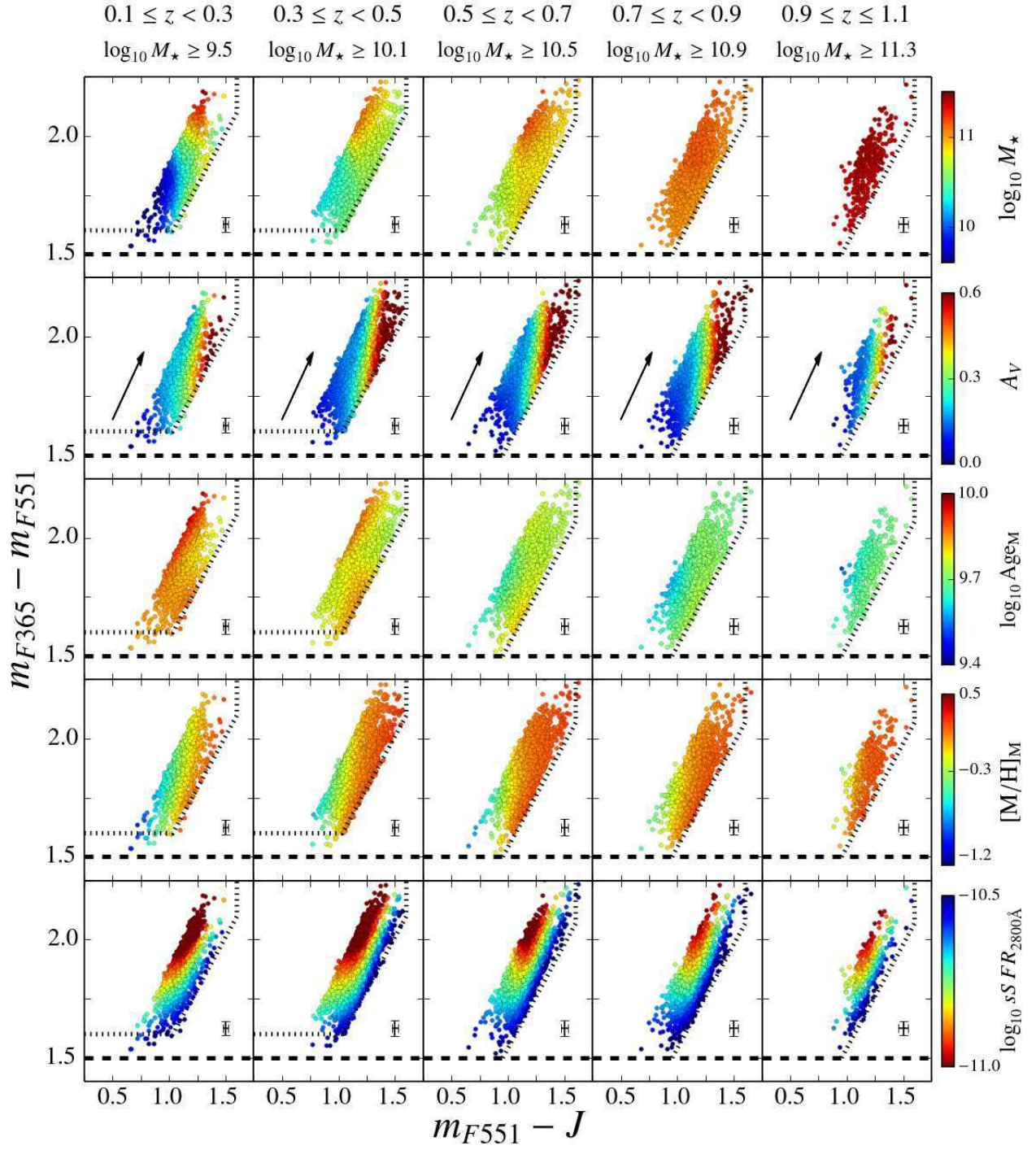


Fig. D.4. As Fig. D.3, but we plot the rest-frame colours $m_{F551} - J$ (X-axis) and $m_{F365} - m_{F551}$ (Y-axis) instead.

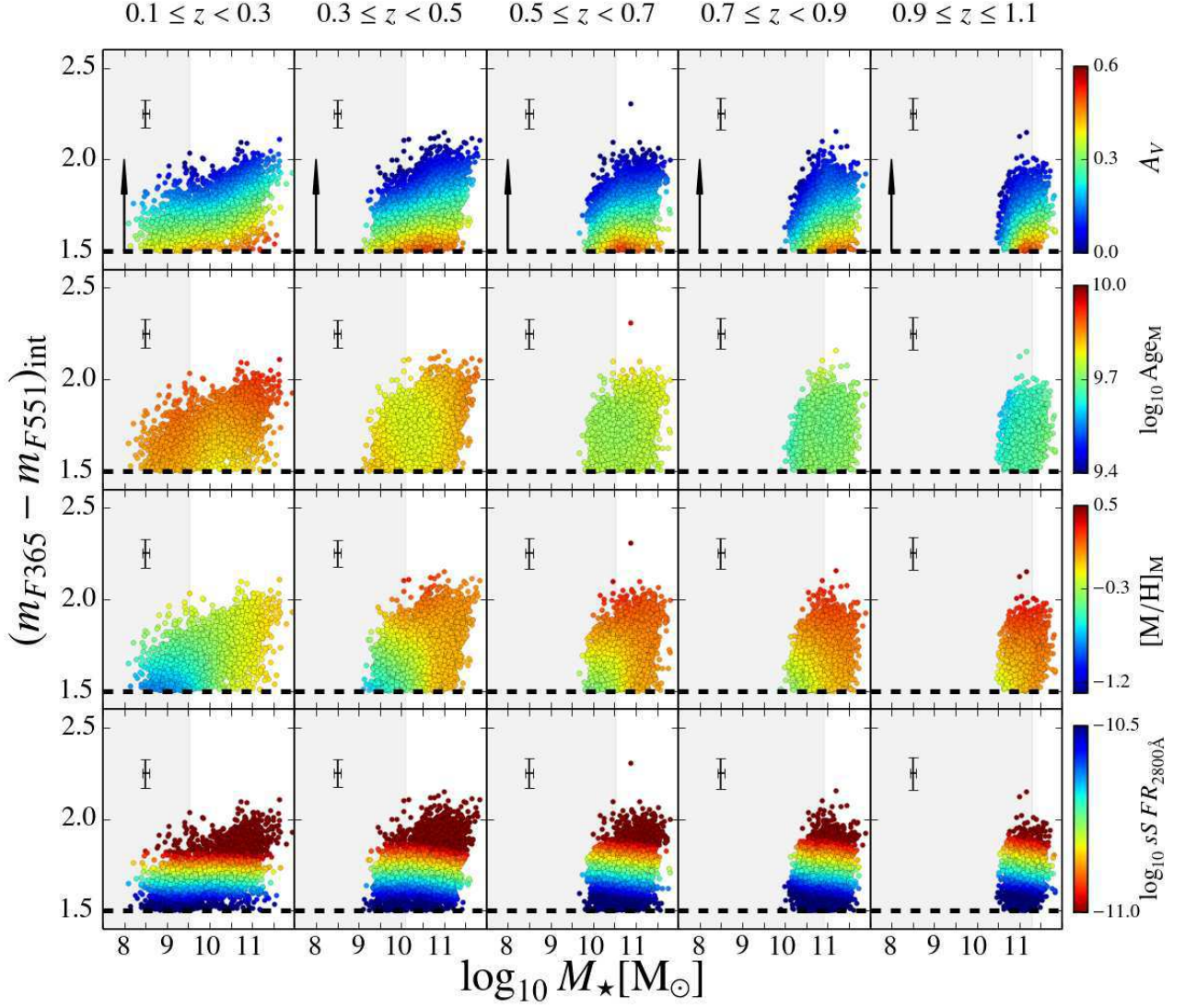


Fig. D.5. The stellar-population parameters in the rest-frame stellar mass-colour diagram. At different redshift bins, we present the stellar mass (X-axis) and intrinsic colour $(m_{F365} - m_{F551})_{\text{int}}$ (Y-axis) after correcting for extinction. The different stellar-population parameters are colour coded in function of their values and obtained using EMILES+BaSTI SSP models, see the inset colour bars in each panel. *From top to bottom*, extinction, both mass-weighted age and metallicity, and specific star formation rate. All the parameters were spatially averaged through a LOESS method. Black crosses illustrate the median uncertainties in both stellar mass and $(m_{F365} - m_{F551})_{\text{int}}$ intrinsic colour. Dotted line illustrates the colour limit for selecting quiescent galaxies $(m_{F365} - m_{F551})_{\text{int}} > 1.5$ in the *UVJ* diagram for this work. Shaded regions show the stellar mass range in which our quiescent sample is not complete in stellar mass. We illustrate the colour variations owing to a reddening of $A_V = 0.5$ (black arrow), assuming the extinction law of Fitzpatrick (1999).

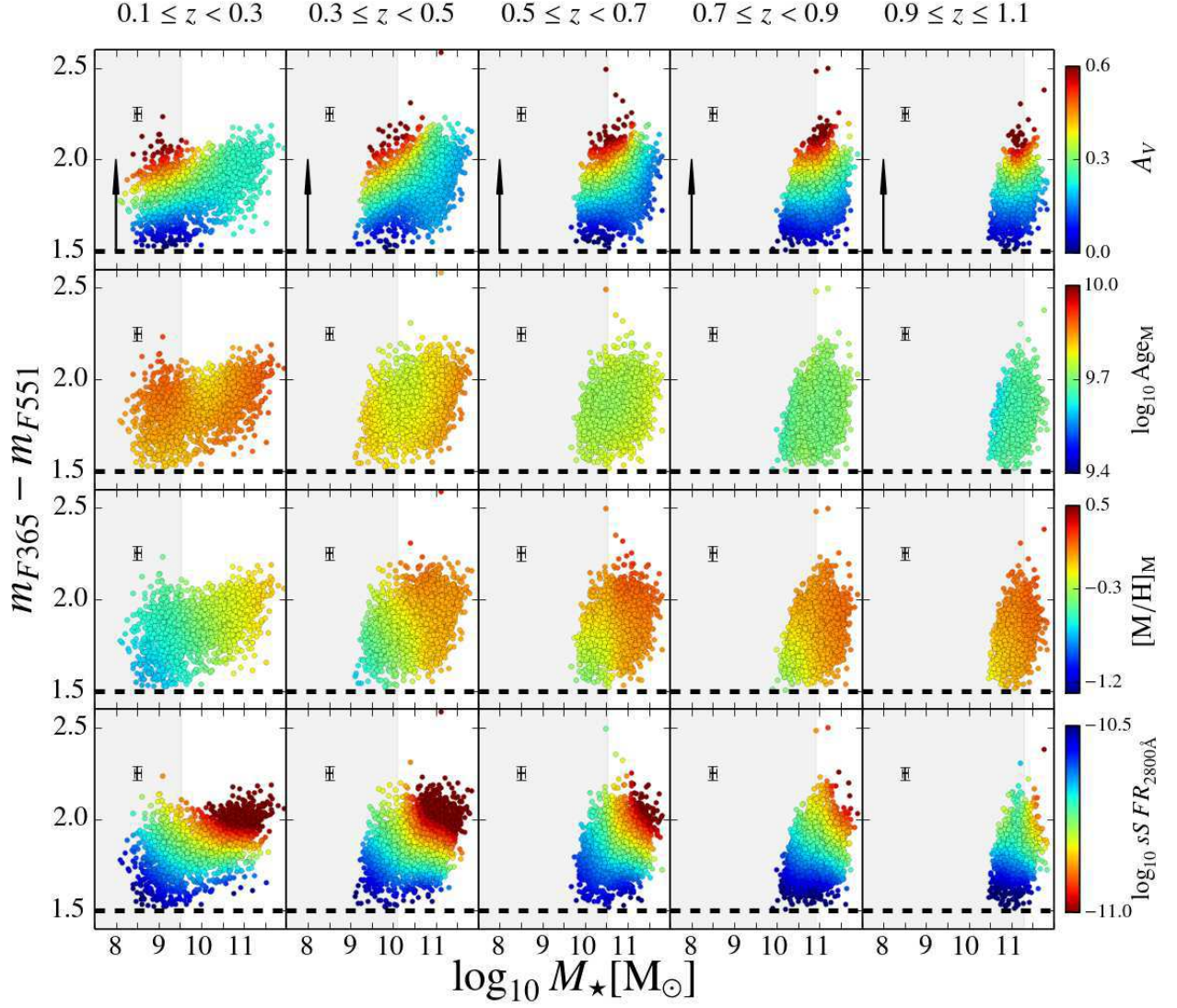


Fig. D.6. As Fig. D.5, but for the rest-frame colour $m_{F365} - m_{F551}$ (X-axis, non-dust corrected).

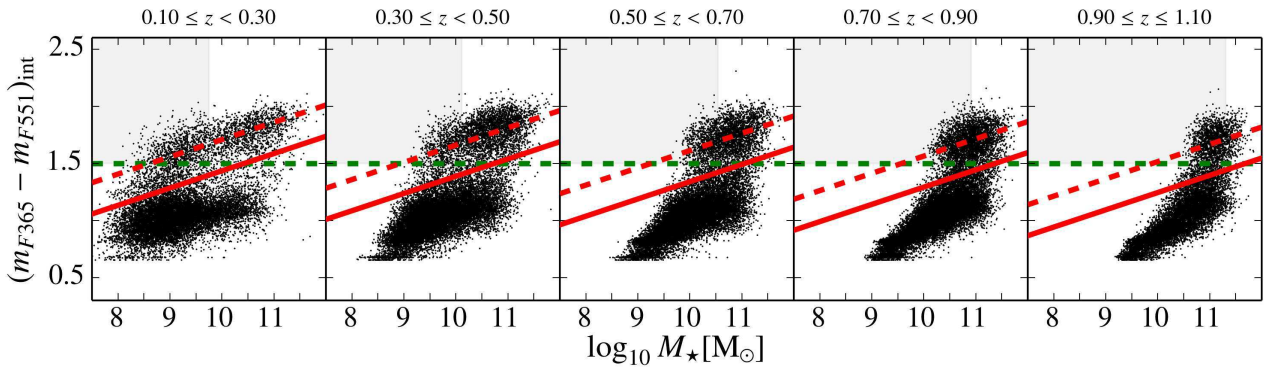


Fig. D.7. All the ALHAMBRA galaxies (black dots) in the rest-frame stellar mass-colour diagram corrected for extinction (MCDE) at different redshift bins. Shaded region illustrates the stellar mass range in which our sample of quiescent galaxies is not complete in stellar mass (see Sect. 3.5) at each redshift bin. Dashed green lines show the limiting value $(m_{F365} - m_{F551})_{\text{int}} = 1.5$ used for selecting quiescent galaxies in Sect. 3.1. Dashed red line exhibits the main sequence of quiescent galaxies in the MCDE (see Eq. 3), whereas the solid one the limiting colour values for selecting quiescent galaxies in this diagram (see Eq. 7). The stellar population predictions were obtained through EMILES+BaSTI SSP models.

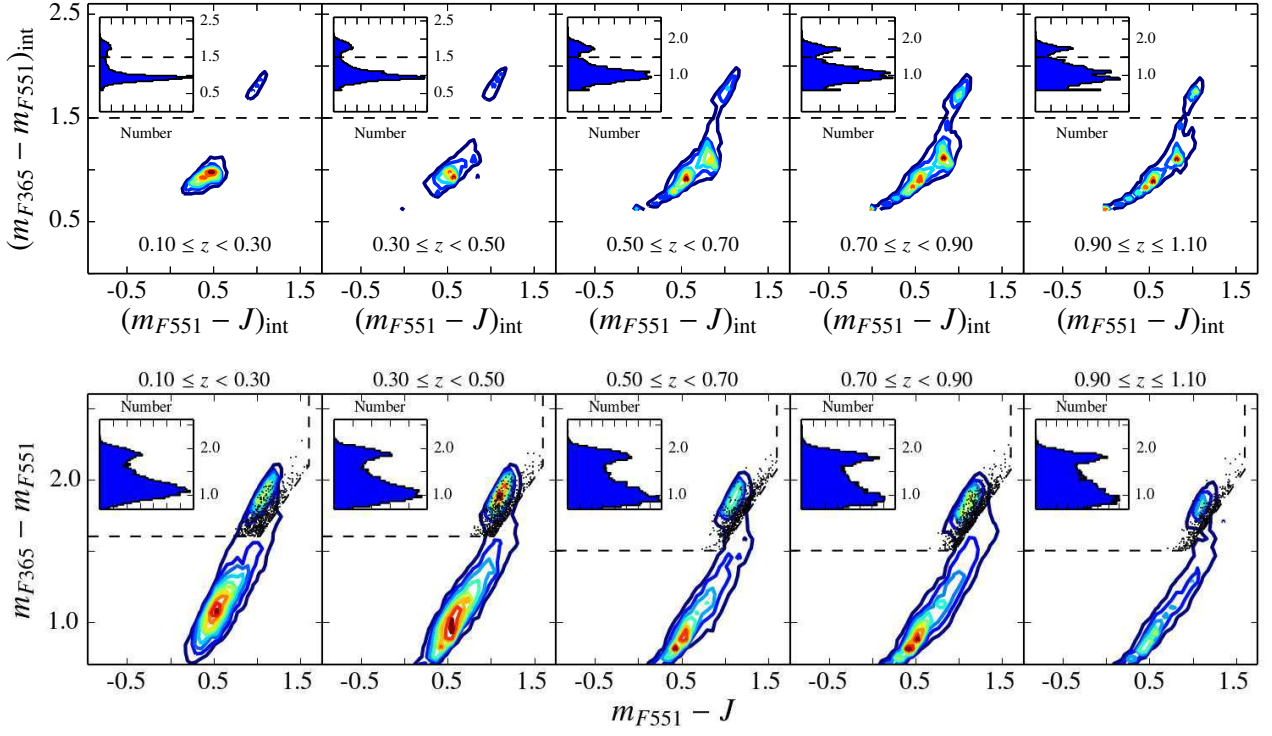


Fig. D.8. As Fig. D.1, but for Padova00 isochrones instead.

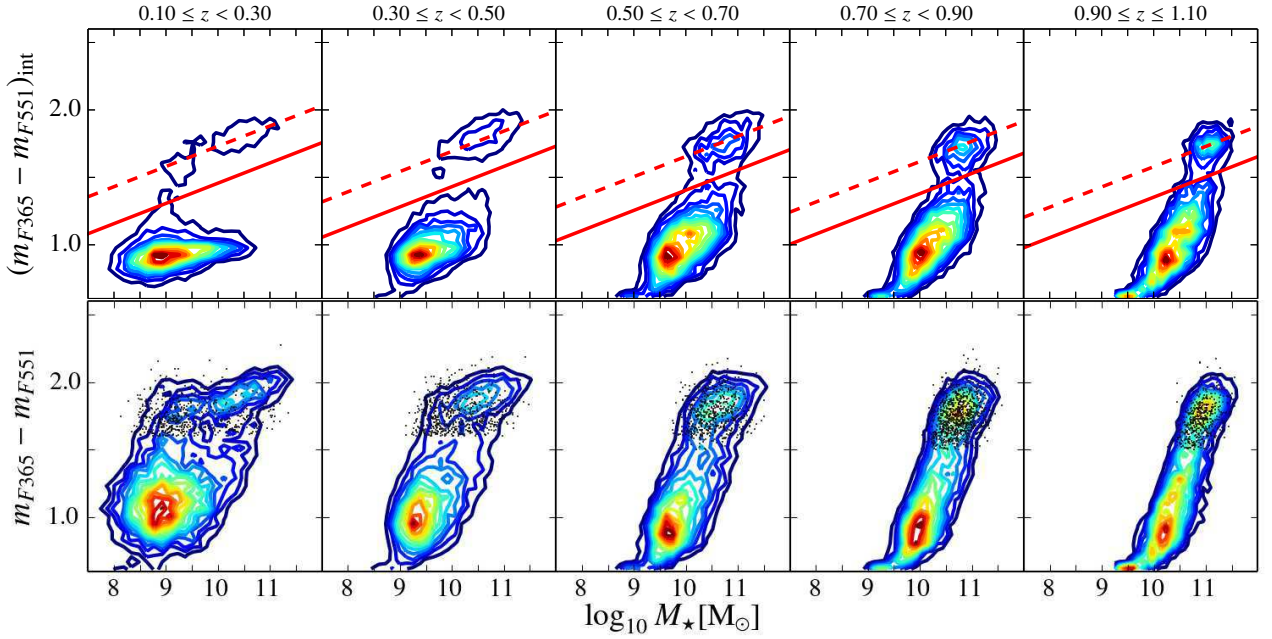


Fig. D.9. As Fig. D.2, but using Padova00 isochrones instead.

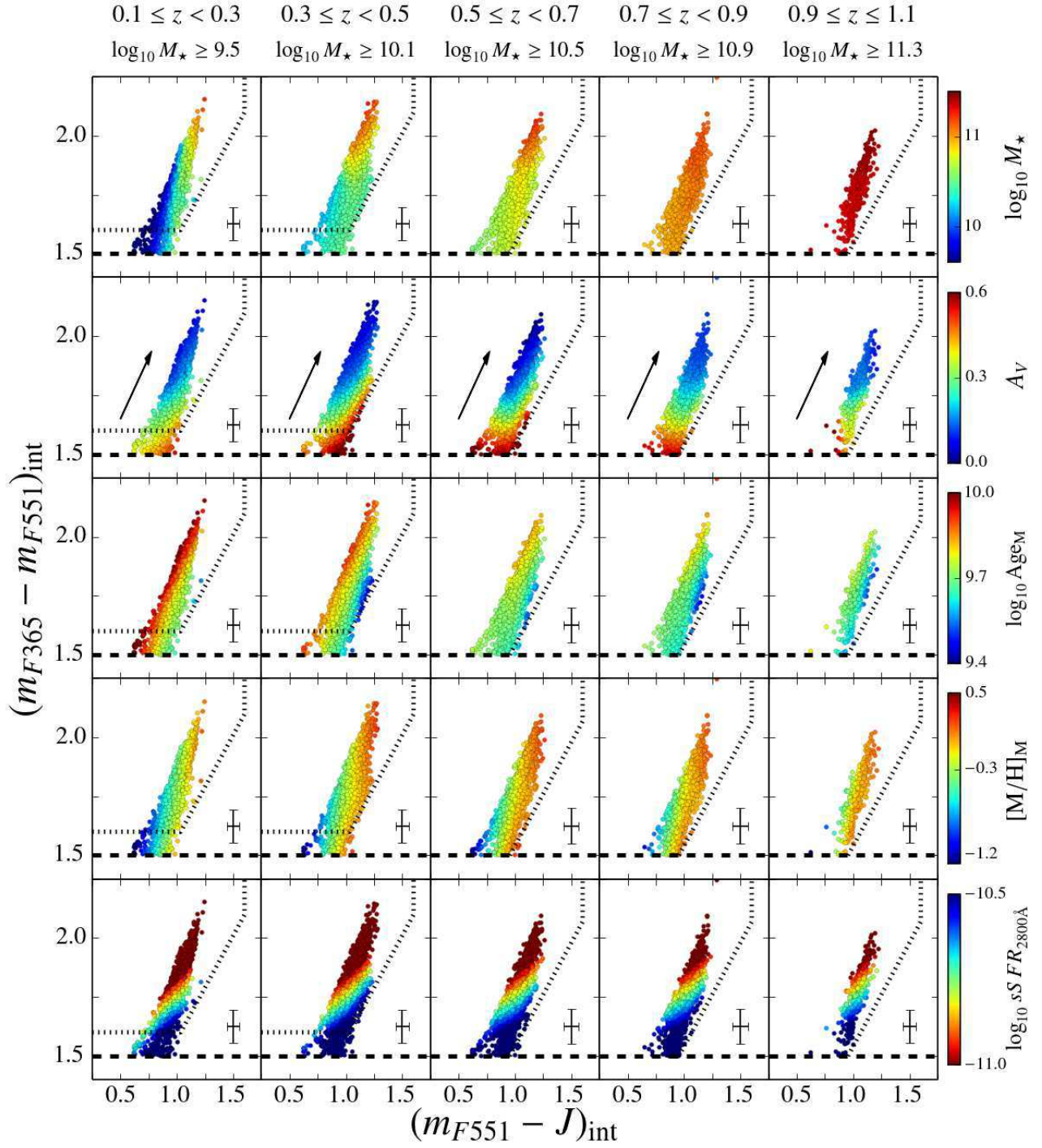


Fig. D.10. As Fig. D.3, but the stellar population predictions were obtained using EMILES+Padova00 SSP models instead.

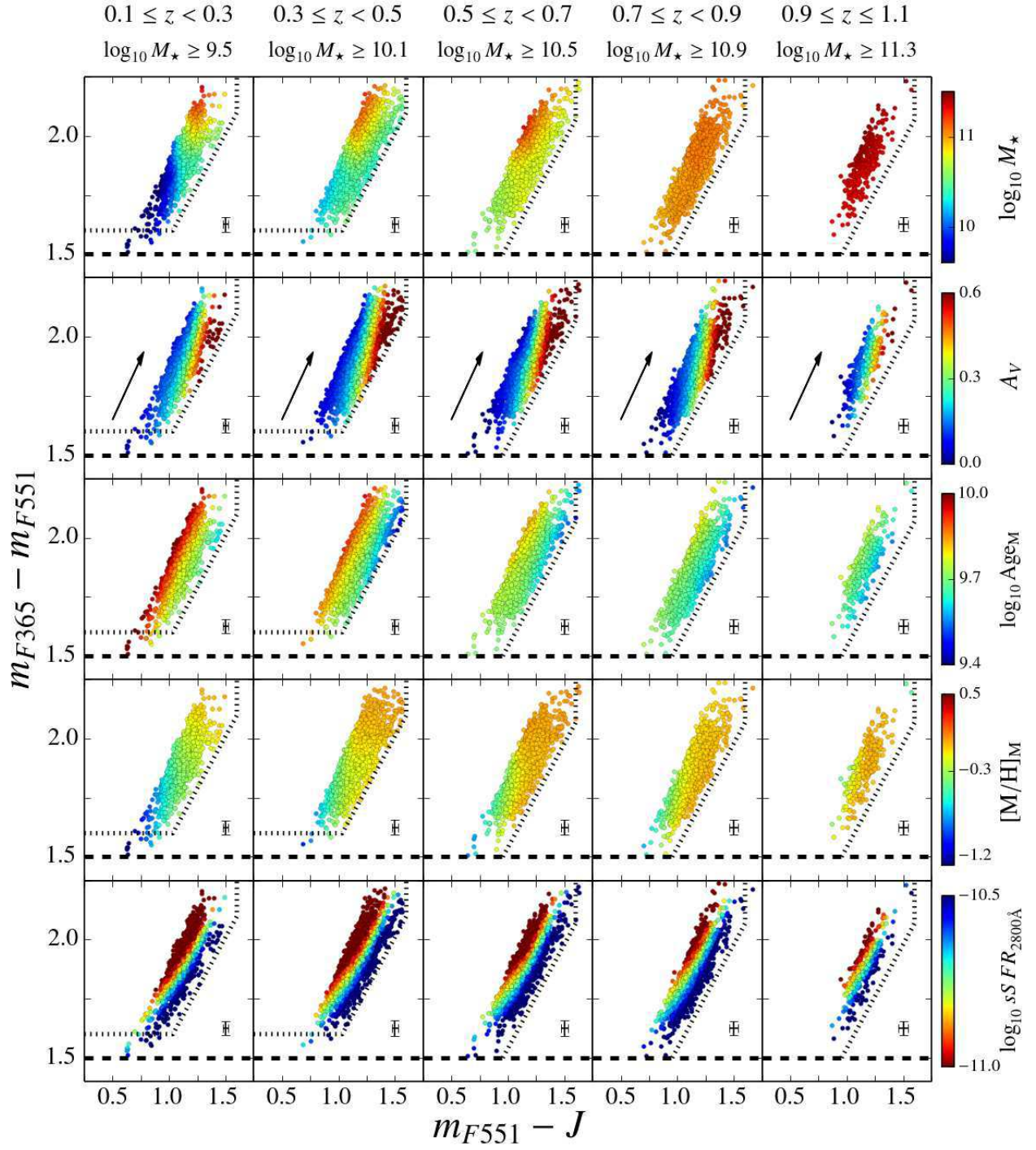


Fig. D.11. As Fig. D.4, but the stellar population predictions were obtained using EMILES+Padova00 SSP models instead.

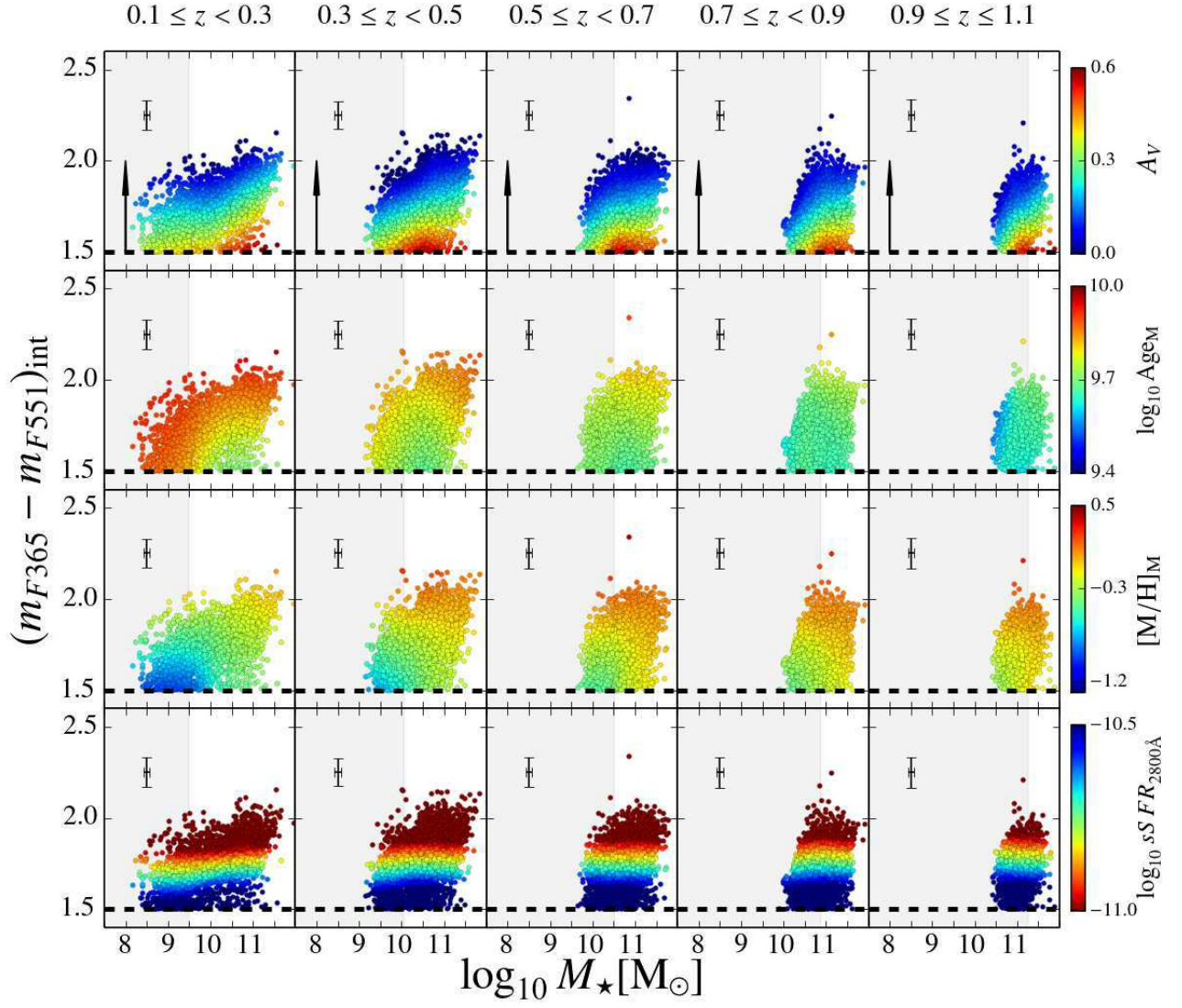


Fig. D.12. As Fig. D.5, but using EMILES+Padova00 SSP models.

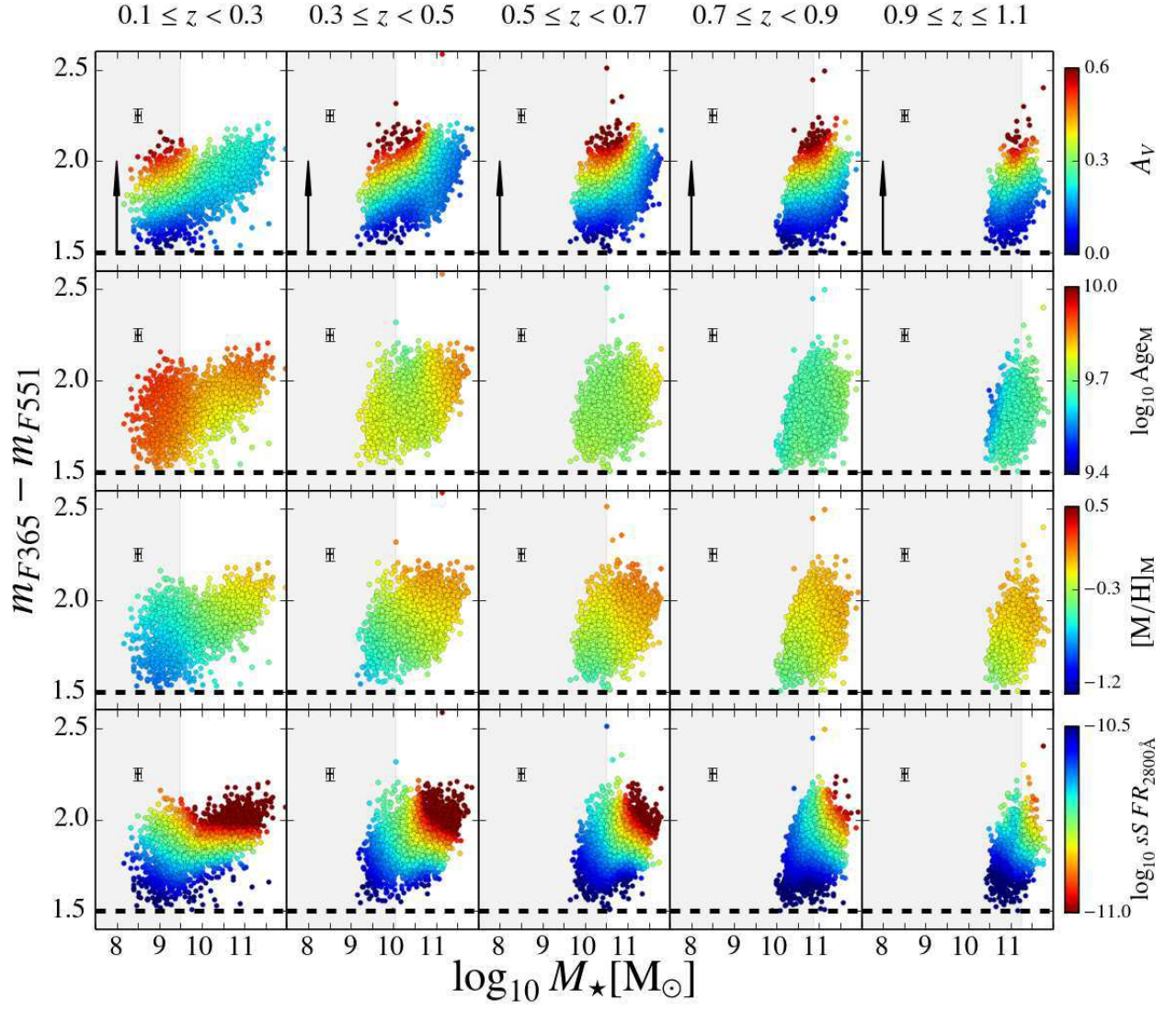


Fig. D.13. As Fig. D.6, but using EMILES+Padova00 SSP models.

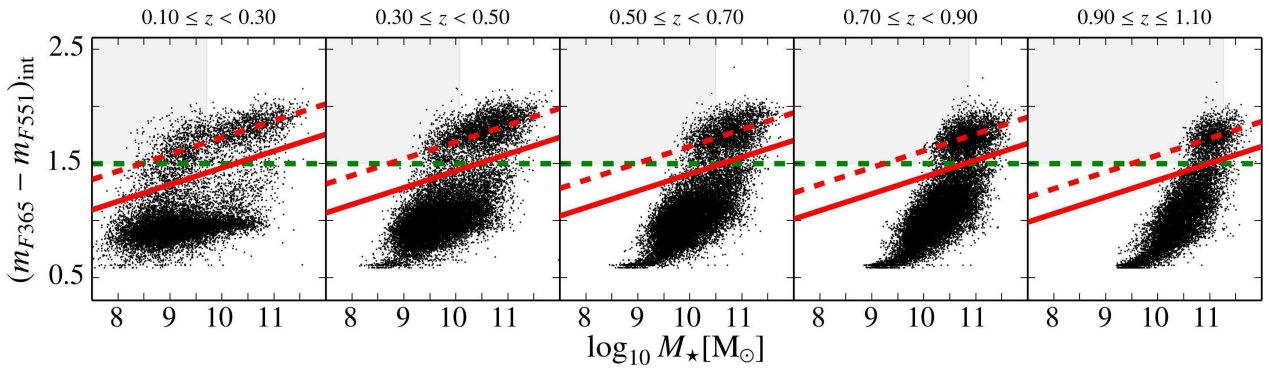


Fig. D.14. As Fig. D.7, but for the stellar population predictions obtained with EMILES+Padova00 SSP models.